2nd International Conference on

Sciences and Techniques for Renewable Energy and the Environment STR2E 2026

April 28-30, 2026

Faculty of Sciences and Techniques
Al Hoceima, Morocco

* *Special issue link : E3S Web of Conferences*

www.str2e.com

str2e.conference@gmail.com

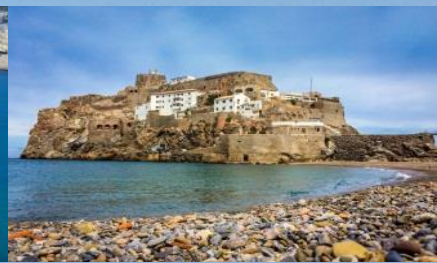

Preface

We are increasingly invited to preserve our planet by encouraging scientific innovations that make it possible to reduce polluting gas emissions through new, green energy resources.

STR2E 2026 is a very important event which aims to promote exchanges and cooperation between students, researchers, academics and industrialists from all over the world in all fields of sciences and techniques related to renewable energy and the environment. The specificity of this event is to welcome all fields of science and technology such as chemistry, physics, informatics, engineering…. which contribute to an integrative approach to renewable energies and the environment. By creating direct contact between international participants, the researchers will have the occasion to discuss the most recent innovations and possible matching cooperation and partnership through international programs, and to promote the exchange of PhD students, academics, and postdocs between the different partners.

STR2E 2026 is organized by the **Chemistry, Computer Science and Artificial Intelligence Research Team (ERCI2A), Faculty of Sciences and Techniques Al hoceima and Abdelmalek Essaadi University, Tetouan, Morocco.**

Renewable energies are an essential asset to protect our planet against brutal climate change largely caused by greenhouse gas emissions and pollution due to the use of fuels that release CO_2 and other gases. In essence, the widespread adoption of renewable energy is a fundamental step towards environmental sustainability, creating a healthier planet and a safer energy future for all.

This special issue brings together very interesting articles related to recent scientific and technological advances in the fields of renewable energy and environmental sustainability, offering a multidisciplinary platform for exchanging ideas, by highlighting cutting-edge research cuts, and fostering collaborations aimed at developing innovative and sustainable solutions to current urgent energy and environmental challenges.

The aim of this Special Issue is to promote and publish recent studies on renewable energy and environmental sustainability. The scope of this Special Issue includes (but is not limited to) the following topics:

* Solar Energy Engineering

* Smart Grid

* Photovoltaic and grid

* Hydrogen storage

* Enegy Conversion

* Electrode Materials for Energy, Environment and Electrochemical Sensors Applications

* Water Splitting, Electrolysis Efficiency and Fuel Cell

* Solar collector and exchangers

* Semiconductors and thin films for photovoltaic

* DFT for Semiconductor Energy Applications

* DFT for Photocatalysts, Catalysts, and optic

* Wind Energy Engineering

* Electric and Hybrid Vehicles

* Batteries

* Biomass Energy Engineering

Prof. Charaf Laghlimi On behalf of STR2E 2026

2nd International Conference on Sciences and Techniques for Renewable Energy and the Environment

April 28-30, 2026 / Al Hoceima, Morocco

www.str2e.com

str2e.conference@gmail.com

c.laghlimi@uae.ac.ma

2nd International Conference on

Sciences and Techniques for Renewable Energy and the Environment STR2E 2026

April 28-30, 2026

Faculty of Sciences and Techniques
Al Hoceima, Morocco

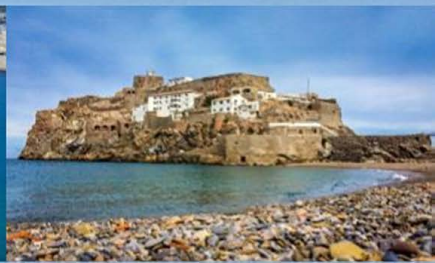

www.str2e.com

str2e.conference@gmail.com

Contents

Development of an ANN-Based Predictive Model for an Airfoil with a Trailing-Edge Flap

Naoual Afif [1,2], Yassine Lakhal [1,2], *Mohammed* Haiek [3], *Fatima Zahra* Baghli [1,2], *Soulaimane* Samagassi [4]

[1] Team of engineering and applied physics, Higher School of Technology of Beni Mellal, Morocco
[2] The Moroccan Association of Sciences and Techniques for Sustainable Development (MASTSD), Beni Mellal, Morocco
[3] Laboratory of Innovative Technologies, National School of Applied Sciences of Tangier. B.P. 1818, Tangier, Morocco.
[4] Training and Research Unit, Laboratory of Mechanics and Computer Science, Félix Houphouët-Boigny University, Abidjan, Ivory Coast.

Abstract. This work makes use of a data-driven approach to predict the aerodynamic performance of the wind turbine airfoil equipped with an active trailing-edge flap. The NACA 4412 airfoil is considered to investigate the effect of the trailing-edge flap angle on the efficiency, measured in terms of the lift-to-drag ratio (Cl/Cd). A vast set of aerodynamic data is generated to consider the angle of attack (α) from −20° to 20° and various flap angles (TE). Based on the generated database, an Artificial Neural Network (ANN) model is formulated to predict the value of Cl/Cd in terms of the angle of attack and the flap angle. The ANN model was trained using 81 iterations with 75% of the dataset used for training, 15% for validation, and 10% for testing. The predictions of the ANN model are then compared to the reference solutions from the Computational Fluid Dynamics (CFD) simulation in the form of systematic plots. The high level of agreement between the predictions of the two approaches emphasizes the validity and accuracy of the proposed data-driven ANN model. The model presented in this work provides an approach to efficiently and accurately overcome the repetitive simulation of aerodynamics and represents an attractive tool in the analysis of smart airfoils with active trailing-edge flaps. The ANN model provides an R^2 value of more than 0.9898 on the test data.

1. Introduction

The increasing need for energy and the need for reducing emissions of greenhouse gases has led to significant research in wind energy technology. The need for improved wind energy technology and overcoming challenges in wind speed fluctuations and turbulence has remained an area of concern in this sector for quite some time now. The conventional airfoil technology is only sufficient in certain areas and has numerous drawbacks in situations involving variations in airflows. The need for overcoming such drawbacks has led researchers to work on smart airfoils with actuators and sensors for managing airflows in real time, which is quite pertinent in the present situation [**1**].

Among the different techniques that have been employed for aerodynamic flow control, the use of trailing edge flaps has been found to be very effective. By providing the airfoil with autonomous control functions, the flap is able to react dynamically to the changing conditions of the wind in real time, which is very helpful for wind turbines [**2, 3**]. Various tests have shown that these flaps are able to affect the lift and drag forces and even delay flow separation [**4, 5**]. The influence of leading edge slats combined with slotted trailing edge flaps has also been studied [6].

However, more recent intelligent control methods have emerged with the aim of optimizing the real-time deflection of the trailing edge flap. For instance, the efficacy of a fuzzy logic control system on a trailing edge flap was demonstrated by Lakhal et al. [7] for improving the aerodynamic performance of wind turbine airfoils.

In order to help in understanding the phenomena, ultra-high resolution models are used to calculate airflow in various geometries. As much as these models are valuable in understanding the phenomena, their high cost and time complexity mean that they are not useful in control and optimization applications in a short time, such as in the optimization of wind turbine design. Simplified models that are less costly and faster are also being explored.

This paper discusses the continuous improvement of airfoil simulation efforts, coupled with parallel studies of applying machine learning methodologies for airflow simulation and understanding performance for various geometries. Artificial Neural Networks (ANNs) and other machine learning techniques have proved to be

remarkably successful over the past few years, especially regarding the complex interplay of airspeed, geometry, and forces of lift and drag [1]. In this context, Haiek et al. [8] presented a metamodeling method for simulating wind turbine airfoils using ANN, highlighting the ability of these models to effectively lower costs of simulation while maintaining their level of accuracy. More advanced techniques have been investigated for adaptive flow control and wing geometry optimization, exploiting the potential of high-performance computing for autonomous learning [2, 3].

Recent studies have also focused on integrating trailing-edge flap control with aerodynamic actuators to enhance energy extraction efficiency in turbines [9]. Moreover, the design of turbine blades increasingly considers structural optimization to reduce material usage while maintaining performance [10].

The purpose of this research is the development of an ANN model that has the capability of estimating the efficiency of a specific airfoil with a trailing flap using a large dataset of aerodynamic tests carried out on different models. With the use of the ANN model that can substitute the expensive CFD simulations, this research has the potential of being utilized in the wind turbine blades' optimization process[**7,** 8].

Unlike conventional ANN-based aerodynamic surrogate models that focus on fixed airfoil geometries, the present work incorporates the effect of active trailing-edge flap deflection, enabling the prediction of aerodynamic performance for morphing airfoils.

The rest of this paper will have the following structure. In Section 2, an overview of existing research on this subject will be given. The building of the aerodynamic database will then be explained in detail in Section 3. The structure of the artificial neural network used in this study will then be introduced in Section 4. The final results of this study will then be presented in Section 5.

2. Related Work

Active flow control technology on airfoils has made significant progress in the past two decades. The initial work on trailing-edge flaps in wind turbines primarily focused on aerodynamic performance evaluation by analytical modeling or algorithms. Later,Qian et al. [4] investigated deformable trailing-edge flaps in thick airfoils of a wind turbine by numerical simulations and observed a great improvement in aerodynamic performance and a decrease in loading.

The more recent studies have focused on various trailing edge modification techniques such as slots, serrations, and their combinations with high-lift devices. Tanürün et al. [5] studied the aerodynamic performance of NACA airfoil with a slotted trailing edge, while Arra et al. [6] studied the influence of slats on the NACA airfoils with slotted trailing edge flap.

Taken together, it is clear that trailing-edge flow control is an important area of research for airfoil design. The use of computational fluid dynamics (CFD) simulation results has gained importance in analyzing complicated flow control designs due to increasing computational power. Karthikeyan & Harish [1] used machine learning algorithms along with CFD simulation for analyzing hybrid flow control on NACA 4412 airfoil.

Recent trends have also combined reinforcement learning and deep learning techniques alongside classical supervised learning in adaptive and intelligent flow control. A deep supervision network combined with reinforcement learning for morphing trailing-edge wings was introduced by Dai et al. [2], while Portal-Porras et al. [3] directly used reinforcement learning for active flow control on airfoils. Although these methods offer potential for real-time decision-making tasks, they may involve significant data and computational costs during training.

In the context of wind turbine optimization, Wang et al. [**9**] and Han et al. [**10**] explored control strategies combining pitch and trailing-edge flap actuation in vertical axis wind turbines. Mansi & Aydin [**11**] studied the effect of trailing edge flaps on small-scale horizontal axis wind turbines. Li et al. [**12**] investigated nonlinear modeling and adaptive control of smart rotor wind turbines. Sanaye & Farvizi [**13**] developed an ANN-based approach with genetic algorithms for optimizing helical-blade vertical axis wind turbines.

Environmental impact assessments have become an important consideration for wind energy projects, as highlighted by Nazir et al. [**14**].

However, there still remains a requirement for effective and accurate aerodynamic models to successfully forecast values of Cl/Cd for airfoils with trailing-edge flaps. In fact, there is a lack of focus regarding surrogate models developed for flow data or for a control-oriented model. In point of fact, it should be noted that this paper will focus on addressing these concerns by creating and validating a model for a NACA 4412 airfoil with a trailing-edge flap via ANN.

3. Aerodynamic Database Generation

3.1 Airfoil and Trailing-Edge Flap Configuration

The aerodynamic study is done using NACA 4412 airfoil, which is commonly used in wind turbine blades because of its excellent lifting abilities at low to moderate Reynolds numbers. The NACA 4412 airfoil has maximum camber of 4% at 39.5% of chord length with relative thickness of 12%.

The trailing edge flap is an addition made to the basic airfoil to alter actively its aerodynamic characteristics. The geometry is described by a rigid hinged surface placed 80% on the chord and located 50% thick, covering 20% of the chord length. Flaps are tested by varying their angles of deflection (TE), varying the angles of attack (α) and maintaining a constant flap length (Fig. 1). Angles of deflection varying from -20° to 20° are tested, and their effect is observed on aerodynamic characteristics

Polar curves are created for angles of attack ranging from -20° to 20°. The ratio of lift to drag (Cl/Cd) is chosen as the criterion of excellence because this parameter directly indicates airfoil efficiency. In this way, it is possible to create an organized airfoil data base concerned with training and verifying the new proposed ANN prediction model.

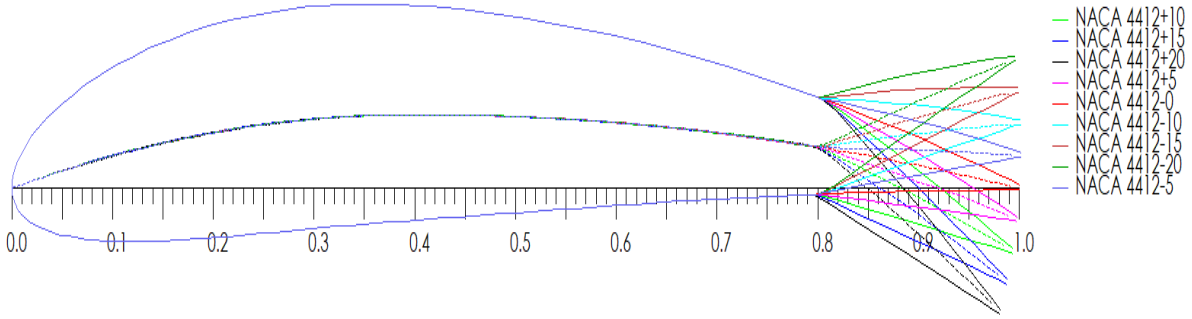

Fig. 1. Schematic of NACA 4412 with Variable Trailing-Edge Flap

3.2 Airfoil Simulation Methodology for ANN Training Data

The aerodynamic simulations were performed using QBlade, which relies on the XFOIL aerodynamic solver. The flow solution is obtained using a panel method coupled with a boundary-layer solver that accounts for viscous effects and boundary-layer development along the airfoil surface.

The computation of the aerodynamic database is done for every trailing-edge flap setting. The simulations are done with a Reynold number equal to 1000000 and within an angle of attack range of -20° through 20° and This allows a broad spectrum of aerodynamic conditions to be analyzed. This range includes pre-stall as well as post-stall conditions.

For each working condition, the values of the lift coefficient and the drag coefficient are calculated, and thereafter the resulting lift-to-drag ratios (Cl/Cd) are determined (Fig. 2). This approach results in a methodical generation of a dataset that interprets the nonlinear relationship between aero efficiency, angle of attack, and trailing flap deflection.

The obtained data is used as a basis for establishing a referential database used for testing and training the model of the artificial neural network for predictive evaluation purposes.

The generated aerodynamic coefficients for the NACA 4412 airfoil were validated against **well-established polars from the literature** at the same Reynolds number, showing good agreement and confirming the reliability of the QBlade/XFOIL simulations.

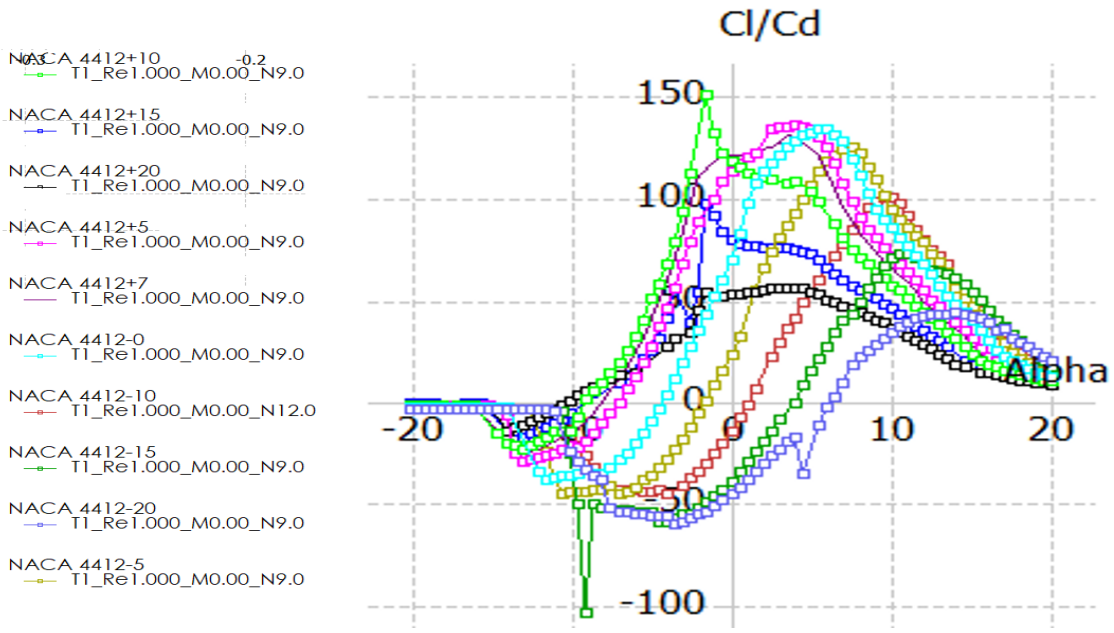

Fig. 2. Lift-to-Drag Ratio (Cl/Cd) vs. Angle of Attack for Various Flap Deflections

A mesh independence study was conducted to ensure that the numerical results were not affected by the grid resolution. Several meshes with increasing refinement levels were generated around the NACA 4412 airfoil, particularly near the airfoil surface and in the wake region. The aerodynamic coefficients (Cl and Cd) were monitored for each mesh configuration. The results showed that further mesh refinement produced negligible variations in the aerodynamic coefficients (less than 1%). Therefore, the selected mesh was considered sufficiently refined to ensure grid-independent results while maintaining a reasonable computational cost.

The aerodynamic database used for training the ANN model was generated using CFD simulations over a wide range of operating conditions. The angle of attack (α) was varied from −20° to 20° with a step size of 0.5°, while the trailing-edge flap deflection angle (TE) was varied from −20° to 20° with a step size of 5°.

This sampling strategy resulted in 81 values of angle of attack and 9 values of flap deflection, leading to a total of 729 CFD simulation cases, which were used to build the dataset for ANN training and validation.

The selected range of α ensures that the dataset includes aerodynamic conditions corresponding to pre-stall, near-stall, and post-stall regimes, which allows the ANN model to capture the nonlinear aerodynamic behavior of the airfoil over a wide range of operating conditions.

Therefore, the dataset provides a balanced representation of aerodynamic regimes, ensuring reliable training and generalization capability of the ANN model.

4 ANN-Based Predictive Model

In this paper, we have designed a supervised learning-based prediction model intended to forecast the aerodynamic characteristics of airfoils featuring a trailing edge flap. The prime goal of such a prediction model is to deliver a more efficient and useful alternative to traditional, time-consuming computational fluid dynamics calculations by directly estimating lift-to-drag ratios (Cl/Cd) based on airfoil geometric properties and trailing edge flap deflection angles.

The inputs of the ANN are two important geometric and aerodynamic characteristics of the wing:

- Angle of attack (α),
- Trailing-edge flap deflection parameter (TE).

These inputs are assembled into a vector $x \in \mathbb{R}^2$. The network is trained to predict the lift-to-drag ratio (Cl/Cd), with data created from numerical simulations of the airfoil at different flap deflections.

The proposed ANN model offers several advantages over traditional surrogate modeling techniques:

1. **Ability to capture strong nonlinearities:** Unlike classical response surface or spline interpolation methods, the ANN can accurately model the complex nonlinear relationship between lift-to-drag ratio (Cl/Cd), angle of attack, and trailing-edge flap deflection.
2. **Flexibility and adaptability:** The ANN structure can be easily retrained or extended for different airfoil geometries or operating ranges without redesigning the entire model.
3. **Computational efficiency:** Once trained, the ANN predicts Cl/Cd values almost instantly, avoiding the need for repeated CFD simulations or time-consuming interpolations.
4. **Robustness to large datasets:** The ANN can efficiently handle large CFD datasets, maintaining high predictive accuracy even across pre-stall and post-stall conditions.

Overall, these advantages make the ANN a powerful and practical tool for fast and accurate aerodynamic performance prediction, especially in the context of smart airfoils with active trailing-edge flaps.

4.1 Neural Network Architecture

A feedforward artificial neural network is employed within this study. The network consists of an input layer that is 2 neurons in number representing the angle of attac k(α) and the trailing edge flap deflection angle (TE), a hidden layer that is 10 neurons in number using a sigmoid activation function meant to handle nonlinearities, and an output layer that is a single neuron meant to predict the lift-to-drag ratio (Cl/Cd) (Fig. 3) .

This architecture is chosen in order to guarantee a proper level of learning, together with simplicity and numerical stability.

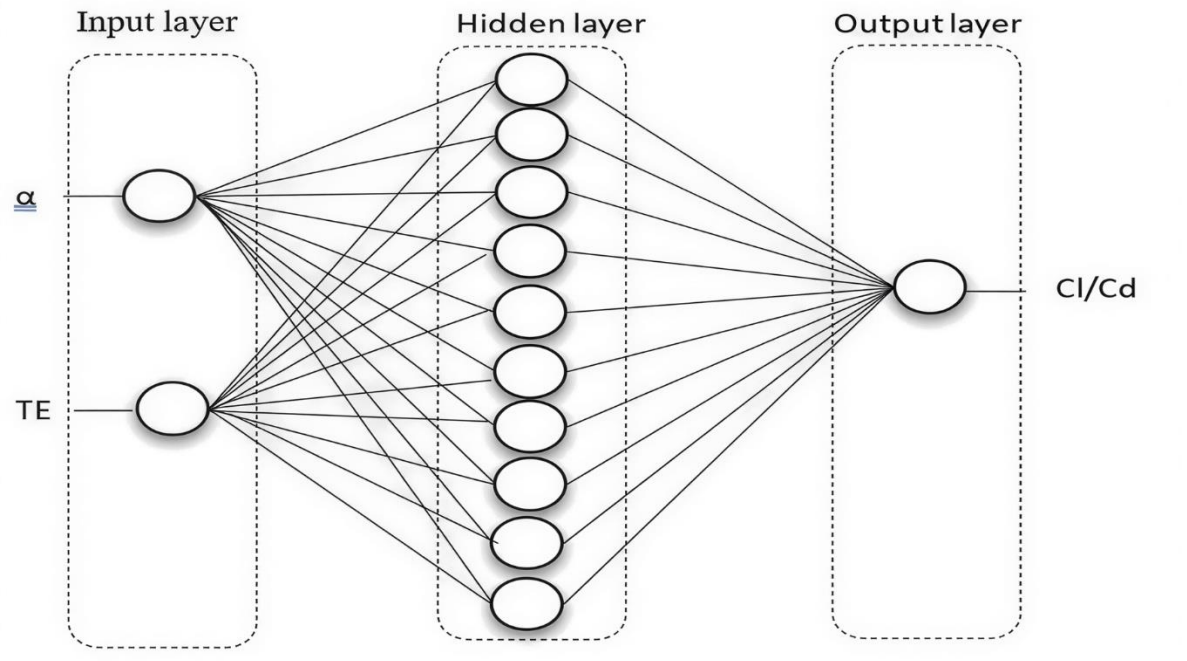

Fig. 3. Neural network architecture for ANN-Based Predictive Model

4.2 Training Methodology

The training process was carried out in three sequential phases:

1. **Training** using 75% of the data,
2. **Cross-validation** on 15% of the data,
3. **Testing** on the remaining 10%.

The ANN architecture used in this study consists of an input layer with two neurons corresponding to the angle of attack (α) and the trailing-edge flap deflection angle (TE), one hidden layer composed of 10 neurons, and an output layer with a single neuron predicting the lift-to-drag ratio (Cl/Cd). The sigmoid activation function was used in the hidden layer to capture nonlinear aerodynamic relationships, while a linear activation function was applied in the output layer.

The dataset was divided into three subsets for model development: 75% of the data were used for training, 15% for validation, and the remaining 10% for testing. This split strategy ensures that the model is trained efficiently while maintaining its ability to generalize to unseen data.

To reduce the risk of overfitting, a validation-based early stopping strategy was employed during the training process. The Levenberg–Marquardt optimization algorithm was used to minimize the mean squared error (MSE) between predicted and reference values. The network hyperparameters, including the number of hidden neurons and training iterations, were selected based on preliminary tests to achieve a good compromise between prediction accuracy and computational efficiency.

For the training of the Artificial Neural Network (ANN), a total number of 81 iterations were carried out. Unlike the random or stratified sampling approach followed in traditional methods, the training dataset was developed using a specific ordering of the NACA 4-digit airfoil 4412 according to the trailing edge flap deflection angles. The validation dataset was obtained through random sampling of the total dataset in order to test the ability of the ANN in generalizing airfoil geometries.

The training process used the Levenberg-Marquardt method, which is better suited for gradient descent algorithms and the Gauss-Newton method for quick convergence to a local minimum of the mean squared error (MSE).

The performance assessment of the proposed model was carried out by giving major emphasis to the value of the statistic of the coefficient of determination (R^2) as the primary assessment statistic, and Mean Squared Error (MSE) was considered as the secondary assessment statistic. These metrics were observed to monitor the learning process and ensure that there was no overfitting.

The quantitative performance of the ANN model during training, validation and testing phases is summarized in Table 1.

Table 1. Values of R and MSE during the construction of the metamodel

	Observations	MSE	R
Training	511	63.3588	0.9847
Validation	109	37.9958	0.9905
Test	109	50.8051	0.9898

4.3 Test and Validation

The validation step is the test of the ability of the predictive model based on ANN to correctly predict the value of the ratio of lift to drag (Cl/Cd) for trailing edge flap angles not presented during the training step.This is an important step to verify that the network is able to generalize and not simply memorize.

The model is guaranteed to be reliable if it meets the following criteria:

- High value of coefficient of determination ($R^2 \approx 1$) for both training and validation datasets;

- The convergence of mean squared error (MSE) to a stable point after a certain number of training epochs;

- Convergence and stabilization of the damping parameter μ in the Levenberg-Marquardt optimization algorithms.

Moreover, the tools for qualitative assessment such as the path followed by the MSE values during the epochs and the graphs showing the predictions against the actual values offer tangible proof about the ability of the model to approximate the reference behavior.

The convergence of the learning process can be analyzed through the evolution of the mean squared error shown in Fig. 4.

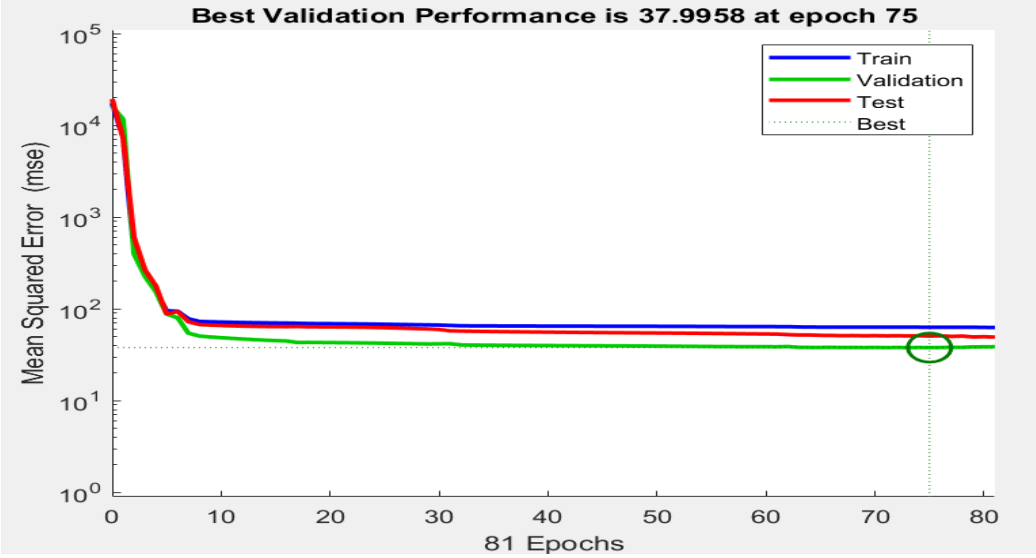

Fig. 4. Mean Squared Error (MSE)

A comparison of the error evolution in the different phases of model construction is presented in Fig. 5.

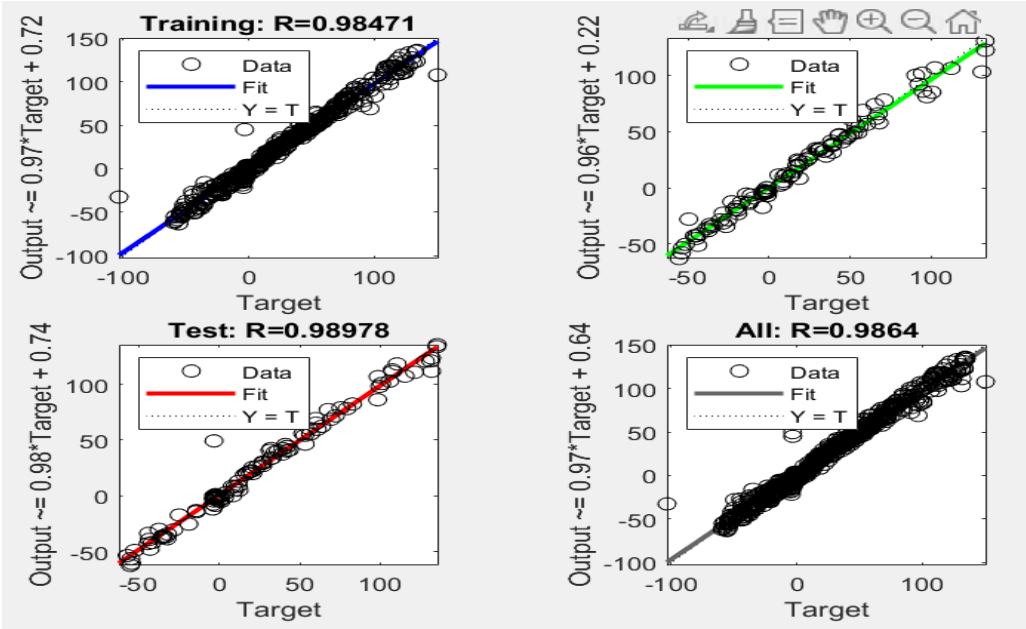

Fig. 5. MSE of different phase of ANN model building

4.4 Analysis on Unseen trailing-edge flap deflections

A set of trailing edge flap deflections, not practiced during the training procedures, is chosen to validate the prediction capability of the ANN model. For each flap deflection, the set of inputs provided to the model is the geometric variables set, the trailing edge flap deflection (TE), and the angle of attack parameter (α). The resulting output from the model is the lift-to-drag ratio (Cl/Cd), which is compared to the reference value obtained from the CFD databases.

As shown in Fig. 6. Cl/Cd ratio values generated by the ANN predictive model for a trailing-edge flap deflection equal to −17.5 demonstrate an almost perfect convergence across all angles of attack considered.

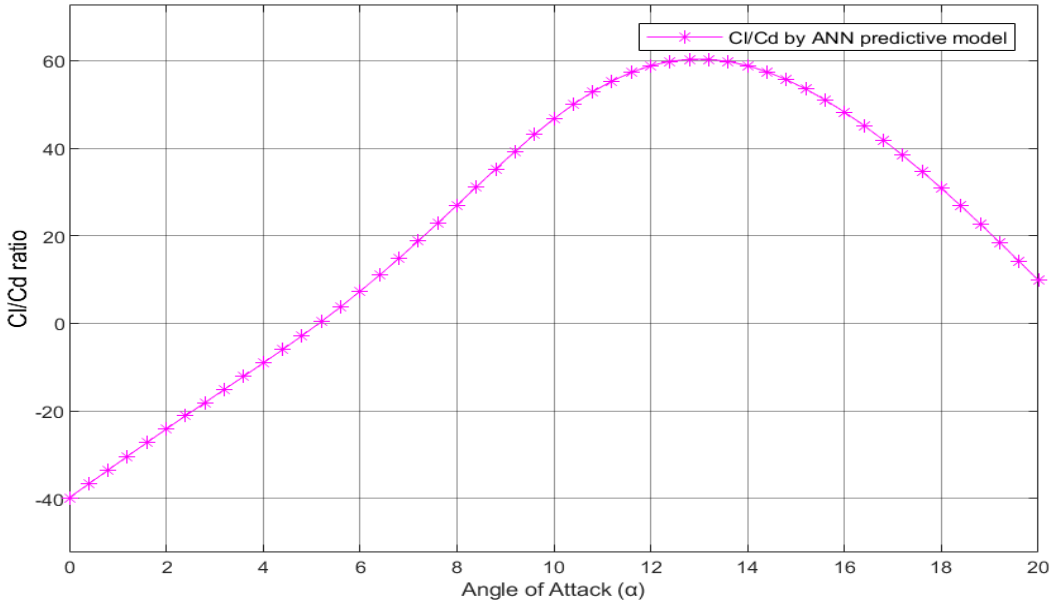

Fig. 6. Cl/Cd ratio values generated by the ANN predictive model for a trailing-edge flap deflection equal to -17.5

In Fig. 7. Cl/Cd ratio values obtained through CFD simulations for a trailing-edge flap deflection equal to −17.5 confirm this agreement, with only slight discrepancies at higher angles of attack, while maintaining the correct trend and accurately identifying the efficiency peaks.

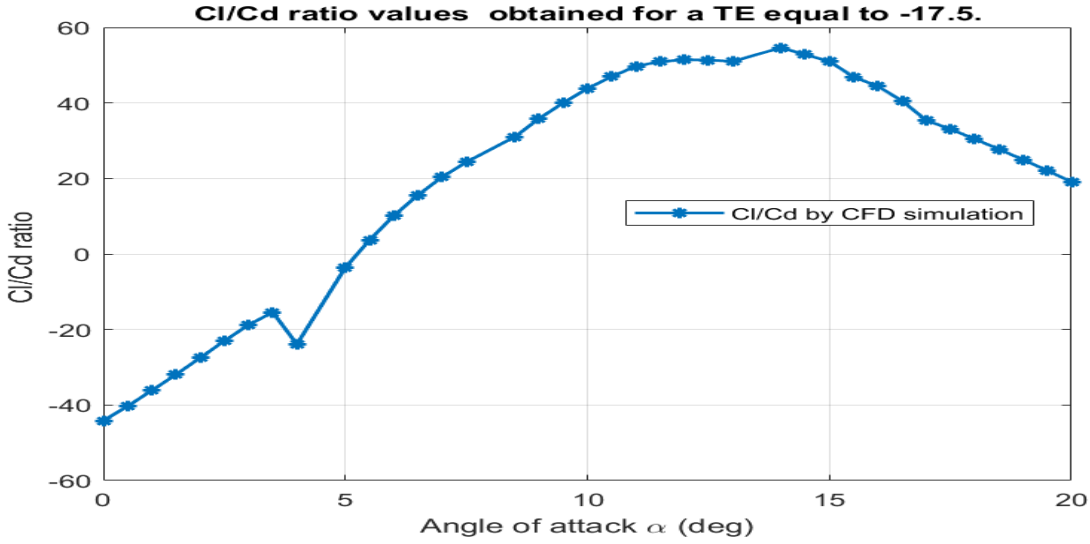

Fig. 7. Cl/Cd ratio values obtained through CFD simulations for a trailing-edge flap deflection equal to -17.5

In addition to the comparison with CFD simulations, the predictive capability of the proposed ANN model can be discussed with respect to previous research on data-driven aerodynamic modeling. Similar approaches using

artificial neural networks for airfoil performance prediction have been reported in the literature. For instance, Haiek et al. [8] demonstrated that ANN-based metamodels can effectively reproduce aerodynamic trends while significantly reducing computational cost. In the present study, the obtained coefficient of determination ($R^2 \approx 0.9898$) confirms that the proposed model achieves a comparable level of predictive accuracy.

Moreover, previous studies such as those of Sanaye and Farvizi [13] , as well as Li et al., have shown that intelligent modeling techniques can be successfully integrated into wind turbine optimization frameworks. The results obtained in this work are consistent with these findings, highlighting the ability of machine learning approaches to capture the nonlinear aerodynamic behavior of airfoils equipped with control devices such as trailing-edge flaps.

In addition to the quantitative agreement between the ANN predictions and the CFD results, the model is also able to reproduce the main aerodynamic trends typically observed for airfoils. In particular, for moderate angles of attack corresponding to the pre-stall region, the predicted aerodynamic performance follows a smooth and nearly linear evolution with increasing angle of attack. This behavior is consistent with the classical lift curve slope observed in airfoil aerodynamics. As the angle of attack approaches the stall region, the model captures the peak aerodynamic efficiency, followed by a gradual decrease at higher angles of attack corresponding to post-stall conditions. This confirms that the ANN model is capable of reproducing the nonlinear aerodynamic behavior associated with flow separation and stall phenomena.

A sensitivity analysis of the predicted aerodynamic performance was also conducted to examine the influence of the angle of attack (α) and the trailing-edge flap deflection angle (TE) on the lift-to-drag ratio (Cl/Cd). The results indicate that the angle of attack plays a dominant role in determining the aerodynamic efficiency of the airfoil, as it directly controls the flow behavior and lift generation. Variations in α lead to significant changes in the Cl/Cd ratio, particularly near the stall region.

On the other hand, the trailing-edge flap deflection modifies the aerodynamic performance by adjusting the effective camber of the airfoil. Although its influence is generally smaller than that of the angle of attack, the flap deflection allows fine control of the aerodynamic efficiency and can shift the optimal operating conditions. This demonstrates that the ANN model is able to capture the combined influence of both parameters on airfoil performance.

From a practical perspective, the results provide insight into the optimal range of trailing-edge flap deflections for wind turbine applications. The analysis shows that moderate positive flap deflections improve aerodynamic efficiency by increasing the effective camber of the airfoil. For example, for angles of attack between **4° and 10°**, the lift-to-drag ratio (Cl/Cd) increases from approximately **55–60 for TE = 0°** to about **60–65 for TE = 5°**.

However, larger flap deflections tend to increase drag and reduce aerodynamic efficiency. For instance, when the flap deflection reaches **15°**, the Cl/Cd ratio decreases to approximately **45–50** due to the significant drag penalty. Based on these observations, the optimal flap deflection range for maximizing aerodynamic efficiency is typically between **0° and 10°**, depending on the operating angle of attack.

These results suggest that moderate flap deflections can be beneficial for wind turbine blade performance, particularly for fine aerodynamic control under varying wind conditions.

5 Conclusion

In the present study, an artificial neural network (ANN)-based model has been proposed for predicting the aerodynamic efficiency, in terms of the Cl/Cd ratio, for a NACA 4412 airfoil section provided with a trailing-edge flap. A look-up table for aerodynamic performance has been created by carrying out computational fluid dynamics (CFD) calculations for a variety of angles of attack ranging between $-20°$ and $20°$, as well as for different flap deflection configurations. The proposed ANN model has been found to be very accurate in predicting the reference Cl/Cd ratios.

Furthermore, the aerodynamic database used for training the ANN model was generated from 729 CFD simulations corresponding to different combinations of angle of attack and trailing-edge flap deflection. A

typical CFD simulation required several minutes of computational time depending on the mesh resolution and solver convergence criteria.

In contrast, once the ANN model is trained, the prediction of the lift-to-drag ratio (Cl/Cd) for a new operating condition is obtained almost instantaneously, typically within a fraction of a second. This represents a significant reduction in computational cost compared to running a full CFD simulation for each configuration.

Although the training phase of the ANN requires the initial CFD dataset, it is performed only once. After training, the model can rapidly predict aerodynamic performance for a large number of operating conditions, which makes it particularly suitable for optimization studies and real-time aerodynamic control strategies.

Therefore, the proposed ANN model provides a promising framework for integration into real-time control systems for smart airfoils equipped with trailing-edge flaps, where rapid prediction of aerodynamic performance is required to adapt flap deflection to changing wind conditions.

However, the performance of the model is necessarily dependent on the quality and comprehensiveness of the training database. Expanding the training database to include Reynolds numbers and unsteady aerodynamics is expected to improve the generalization ability of the model. Thus, future studies will focus on improving the model to include unsteady flow conditions, as well as integrating the ANN model with control methods for trailing edge flaps.

Acknowledgements

The authors would like to thank the laboratories and institutions that supported this research work, particularly the Team of Engineering and Applied Physics at the Higher School of Technology of Beni Mellal.

Funding: The authors are warmly grateful to the support of “The Moroccan Association of Sciences and Techniques for Sustainable Development (MASTSD), Beni Mellal, Morocco”

References

[1] K. V. Karthikeyan, R. Harish, CFD-ML analysis of hybrid flow control on NACA4412 airfoil using triangular gurney flap and dual ns-DBD actuators, Aerosp. Sci. Technol. 169, 111404 (2026). https://doi.org/10.1016/j.ast.2025.111404

[2] J. Dai, P. Liu, C. Kong, L. Pan, J. Si, Adaptive control method for morphing trailing-edge wing based on deep supervision network and reinforcement learning, Aerosp. Sci. Technol. 153, 109424 (2024). https://doi.org/10.1016/j.ast.2024.109424

[3] K. Portal-Porras, U. Fernandez-Gamiz, E. Zulueta, R. Garcia-Fernandez, S. Etxebarria Berrizbeitia, Active flow control on airfoils by reinforcement learning, Ocean Eng. 287, 115775 (2023). https://doi.org/10.1016/j.oceaneng.2023.115775

[4] Y. Qian, Y. Zhang, Y. Sun, T. Wang, Numerical investigations of the flow control effect on a thick wind turbine airfoil using deformable trailing edge flaps, Energy 265, 126327 (2023). https://doi.org/10.1016/j.energy.2022.126327

[5] H. E. Tanürün, A. Yıldız, M. Seyhan, Aerodynamic performance analysis of a NACA 63(4)-421 airfoil equipped with a trailing edge slot, Exp. Therm. Fluid Sci. 171, 111604 (2026). https://doi.org/10.1016/j.expthermflusci.2025.111604

[6] A. Arra, N. Anekar, S. Nimbalkar, Aerodynamic effects of leading edge slats and slotted trailing edge flaps on NACA-2412 airfoil, Mater. Today Proc. 44, 587–595 (2021). https://doi.org/10.1016/j.matpr.2020.10.355

[7] Y. Lakhal, M. Haiek, F. Z. Baghli, Y. A. El Kadi, M. Benchagra, D. Sarsri, Smart flow control of an airfoil with trailing edge flap using a fuzzy logic strategy, Int. J. Energy Convers. 12, 5 (2024). https://doi.org/10.15866/irecon.v12i5.25100

[8] M. Haiek, Y. Lakhal, N. Ben Said Amrani, D. Sarsri, S. Samagassi, Metamodeling for predicting the behavior of airfoils of wind turbine blades: An integration of artificial neural networks, E3S Web Conf. 582, 03002 (2024). https://doi.org/10.1051/e3sconf/202458203002

[9] P. Wang, Q. Liu, C. Li, W. Miao, S. Luo, K. Sun, K. Niu, Effect of trailing edge dual synthesis jets actuator on aerodynamic characteristics of a straight-bladed vertical axis wind turbine, Energy 238, 121792 (2022). https://doi.org/10.1016/J.ENERGY.2021.121792

[10] Z. Han, H. Chen, Y. Chen, J. Su, D. Zhou, H. Zhu, T. Xia, J. Tu, Aerodynamic performance optimization of vertical axis wind turbine with straight blades based on synergic control of pitch and flap, Sustain. Energy Technol. Assess. 57, 103250 (2023). https://doi.org/10.1016/J.SETA.2023.103250

[11] A. Mansi, D. Aydin, The impact of trailing edge flap on the aerodynamic performance of small-scale horizontal axis wind turbine, Energy Convers. Manag. 256, 115396 (2022). https://doi.org/10.1016/j.enconman.2022.115396

[12] J. Li, Y. Wang, S. Lin, X. Zhao, Nonlinear modelling and adaptive control of smart rotor wind turbines, Renew. Energy 186, 677–690 (2022). https://doi.org/10.1016/j.renene.2022.01.020

[13] S. Sanaye, A. Farvizi, Artificial neural network and genetic algorithm for optimization of helical-blade vertical axis wind turbine, Clean. Eng. Technol. 29, 101088 (2025). https://doi.org/10.1016/j.clet.2025.101088

[14] M. Shahzad Nazir, N. Ali, M. Bilal, H. M. N. Iqbal, Potential environmental impacts of wind energy development: A global perspective, Curr. Opin. Environ. Sci. Health 13, 85–90 (2020). https://doi.org/10.1016/j.coesh.2020.01.002

First-Principles Investigation of Structural and Thermoelectric Properties of KXH_3 (X = Al, Mn, Ni) Perovskite Hydrides

Noureddine Elmeskini[1,2], *Ayoub* Koufi [1,2], *Younes* Ziat [1,2], *Hamza* Belkhanchi [1,2], *Ayoub* Fatihi [1,2], *Charaf* Laghlimi[3,2], *Noureddine* Lakouari [4]

[1]Engineering and Applied Physics Laboratory (EAPL), Superior School of Technology, Sultan Moulay Slimane University, Beni Mellal, Morocco
[2]The Moroccan Association of Sciences and Techniques for Sustainable Development, Beni Mellal, Morocco
[3]ERCI2A, FSTH, Abdelmalek Essaadi University, Tetouan, Morocco
[4]National Institute of Astrophysics, Optics and Electronics (INAOE), Puebla, Mexico. Secretariat of Science, Humanities, Technology and Innovation (Secihti), Mexico

Abstract. In this work, we present a comprehensive first-principles study of the structural, electronic, thermal, and thermoelectric properties of perovskite hydrides KXH_3 (X = Al, Mn, and Ni). Calculations were performed within the framework of density functional theory combined with semiclassical Boltzmann transport theory. Structural analysis confirms the stability of all compounds in the cubic perovskite phase. The electronic band structures and density of states reveal that all three compounds exhibit metallic behavior. In particular, $KAlH_3$ shows a pseudo-gap-like feature near the Fermi level with a low but finite density of states, indicating a weak metallic character, while $KMnH_3$ and $KNiH_3$ display pronounced metallic properties due to significant contributions of transition-metal d orbitals near the Fermi level. The electrical and thermal conductivities increase with temperature for all compounds, with $KAlH_3$ exhibits relatively high electrical conductivity despite its low density of states at the Fermi level. Thermoelectric performance analysis shows an enhancement of the power factor and figure of merit (ZT) at elevated temperatures, with $KMnH_3$ achieving the best performance due to a favorable balance between electrical conductivity, Seebeck coefficient, and thermal conductivity. These results highlight the crucial role of chemical substitution at the X-site in tuning the electronic and transport properties of KXH_3 hydrides, making them promising candidates for high-temperature thermoelectric applications.

1 Introduction

Several factors, including the sustained increase in global energy demand and concerns about greenhouse gas emissions [1], have prompted the search for innovative energy solutions that can provide a sustainable, clean, and more efficient source of energy [2]. Among the many energy alternatives, one area that promises numerous benefits for the development of a sustainable energy solution is hydrogen energy [3]. However, one of the major issues that must be resolved for widespread hydrogen technology application is the availability of a safe, efficient, and reversible hydrogen storage material [4]. Solid-state hydrogen storage systems have gained much attention as a feasible solution to the current storage techniques of high-pressure gas compression and cryogenic liquefaction [5]. Within the context of solid-state storage systems, hydrides and complex hydrides were found to be of great research interest for their high density of hydrogen and relative safety [6]. Of these materials, the perovskite hydrides were found to attract much attention in recent times owing to their stable crystal structure, flexibility in chemical composition, and variability in physical properties [7]. This is because the perovskite structure facilitates the substitution of ions on the cation sublattice, serving as an ideal solution for property modification [8]. In addition to applications for hydrogen storage, there is considerable potential for perovskite hydrides in the area of thermoelectric compounds, especially in high-temperature conditions [7]. The core strength of thermoelectric compounds is their ability to convert waste heat into electricity through a direct process, which is

regarded as an effective means of enhancing total energy efficiency. There is a complex trade-off between Seebeck coefficient, electrical conductivity, and thermal conductivity for thermoelectric compounds that can be effectively tuned via chemical or structural manipulations of their energy band levels. This indicates that compounds with balanced electronic transport properties and controllable thermal conductivities are very valuable.

Recent advances in computational materials science have significantly improved the predictive capabilities of first-principles methods. In particular, density functional theory (DFT), combined with semiclassical Boltzmann transport theory, has emerged as a powerful framework for investigating and optimizing the physical properties of novel materials, especially in the context of thermoelectric applications. These approaches enable a detailed understanding of the interplay between crystal structure, electronic structure, and transport phenomena. Within this framework, perovskite hydrides can be considered promising multifunctional materials, offering potential for both hydrogen storage and thermoelectric energy conversion. Accordingly, the present work aims to perform a comprehensive theoretical investigation of the structural, electronic, thermal, and thermoelectric properties of KXH_3 (X = Al, Mn, and Ni) perovskite hydrides using DFT-based calculations. Particular emphasis is placed on elucidating the effect of X-site substitution on the electronic structure, including band structure and density of states, as well as on the temperature-dependent transport properties. These analyses are essential for understanding structure–property relationships in perovskite materials and for guiding the design of materials with tailored functionalities.

2 Calculation Method

Some of the key ground-state parameters, such as the lattice parameter and its pressure derivative, are included in the present study. In this paper, theoretical calculations based on DFT are used to discuss the electrical conductivity, thermal conductivity, merit factor, and power factor of KXH_3 (X = Al, Mn, and Ni) in the temperature range of 300-900 K. Calculations are performed within the framework of the GGA. Optimization of the crystal lattice volume is a preliminary step before analyzing any electronic thermoelectric properties to ensure that the studied structure is in its minimum energy stable state; therefore, this optimization is performed using the Birch-Murnaghan equation of state, which is integrated into the Wien2k code [9]. To get accurate calculations of total energy and charge convergence along the self-consistent cycle (SCF), rigorous control on threshold values of 0.0001 Ry for total energy and 0.001(e) for charge is followed. Further, dense sampling of the Brillouin zone, along with octahedral integration, is used by means of a 1000 k-point mesh. Later, the thermoelectric properties are investigated using the BoltzTrap software package, which models electronic characteristics to provide a deeper understanding of the performance evaluation of compounds KXH_3 (X = Al, Mn, and Ni).

3 Results and discussion

3.1 Structural properties

Figure 1 depicts the crystal structure of KXH_3 compounds, where X successively represents Al, Mn, and Ni. This particular structure signifies potassium atoms, a substitution element of X, and hydrogen atoms in a perovskite structure. The colored spheres in this structure aptly represent the locations of different atoms, allowing their binding properties around the substitution element, positioned at the center of an octahedral structure, to be ascertained. with lattice parameters $a_0 = b_0 = c_0 = 3.938$ Å, 3.89 Å, and 3.62 Å, of $KAlH_3$, $KMnH_3$, and $KNiH_3$ respectively, with $\alpha = \beta = \gamma = 90°$, these values compare favorably with the Other work $a_0 = b_0 = c_0 = 3.938$ Å [10], 3.89 Å [11], and 3.62 Å [12], of $KAlH_3$ $KMnH_3$ and $KNiH_3$ respectively. This crystal structure aptly shows that compounds of KXH_3 maintain a structure similar to that of perovskite, in which X binds with three other atoms of hydrogen to form a substructure of XH_3, as this particular element resides in the center of an octahedron. The size of element X as a hindering factor, along with being an electron-rich component, maintains a distinctive impact on this structure. This structure also contains a potassium ion positioned in a cubic site, which acts as a donor ion that stabilizes the structure through ionic binding. In addition, the regular geometry of the lattice indicates good structural consistency, which is favorable for studies of electronic and vibrational transport. In this work, full structural optimization was performed, including relaxation of lattice parameters and internal atomic positions

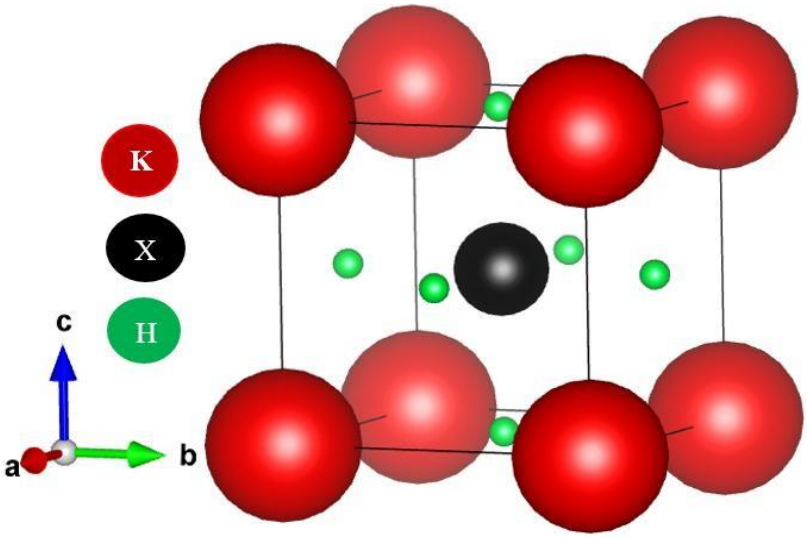

Figure 1. Structure of KXH_3 (X = Al, Mn, and Ni)

3.2 Electronic properties

Figure 2 illustrates the total (TDOS) and partial (PDOS) density of states for KXH_3 compounds for X = Al, Mn, and Ni, calculated around the Fermi level. Each sub-figure shows the electronic contributions of the orbitals of X (p for Al, d for Mn and Ni), K, and H. The PDOS diagrams, plotted in different colors, show the distribution of states in the valence and conduction bands. The TDOS curve at the bottom of each panel summarizes the total energy distribution of the system. The PDOS shows that, for $KAlH_3$, the valence band is mainly determined by Al-p H-s hybridization, indicating a more pronounced covalent character and a conductor tendency. In $KMnH_3$, a prominent presence of Mn-d states near the Fermi energy confers a metallic nature with a pronounced band of density of states around E_F. Moreover, in $KNiH_3$, a prominent contribution of Ni-d orbitals, which are relatively localized and intense, enhances the metallic character. The proximity of the Fermi energy around peaks of DOS in $KMnH_3$ and $KNiH_3$ suggests high electron mobility [13]. The hybridizations of X–H are element-dependent, with relatively weaker hybridizations in Mn, but in Ni, it is extremely dominant, which affects their electronic structure. Also, the lack of a total gap in Mn and Ni suggests better transport properties, unlike Al, which displays relatively insulating properties. The trend also indicates that the element X selects the nature of the chemical bond, bandwidth, as well as electron density. Therefore, flexibility in altering various electronic properties, from conductor grades like Al to relatively metallic in Ni, has been enabled by this substitution.

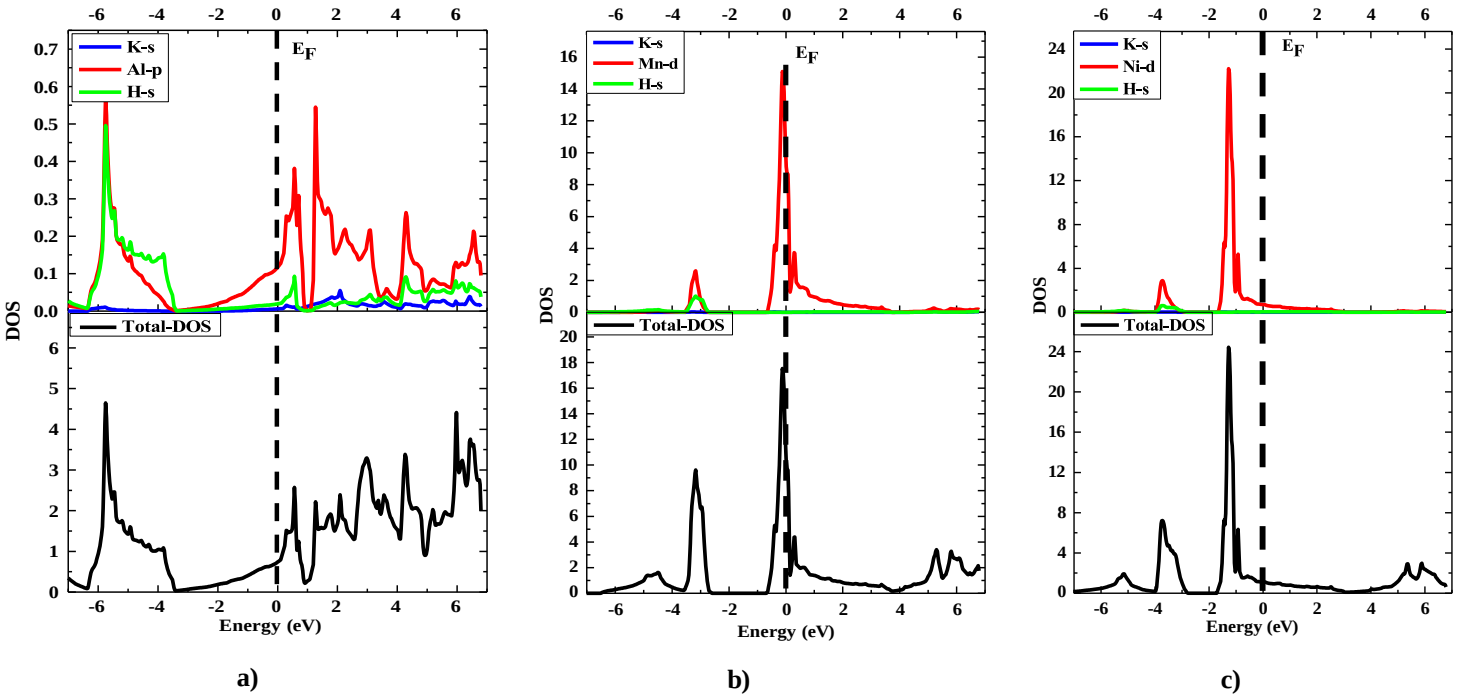

Figure 2. Density of states and partial density of states of a) $KAlH_3$; b) $KMnH_3$ and c) $KNiH_3$

Figure 3 shows the electronic band structures of KXH_3 compounds for X = Al, Mn, and Ni, calculated along the high-symmetry directions of the Brillouin zone. Each diagram illustrates the dispersion of energy bands around the Fermi level, represented by a horizontal dotted line. For all three compounds, bands are present in the vicinity of the Fermi level, indicating metallic behavior. In the case of $KAlH_3$, a pseudo-gap-like feature with low band dispersion is observed near the Fermi level; however, the absence of a true band gap and the presence of electronic states at E_F indicate a weak metallic character. The obtained results are consistent with previous studies on similar perovskite hydrides such as $KAlH_3$ systems reported in [14], where metallic behavior and strong d-state contributions were also observed . In contrast, $KMnH_3$ and $KNiH_3$ exhibit several bands clearly crossing the Fermi level, confirming their metallic nature. In $KMnH_3$, the metallic behavior is mainly driven by Mn-d orbitals, while in $KNiH_3$, the stronger contribution of Ni-d states results in a more pronounced metallic character. The relatively flat nature of these d bands suggests partial electron localization, which can influence charge transport. A comparison among the three compounds indicates that the substitution of Al with transition metals (Mn and Ni) enhances the metallic character due to the increased contribution of d states around the Fermi level. Consequently, $KNiH_3$ is expected to exhibit higher electrical conductivity than $KMnH_3$. Overall, these results demonstrate that the choice of the X element plays a key role in tuning the electronic properties of KXH_3 compounds.

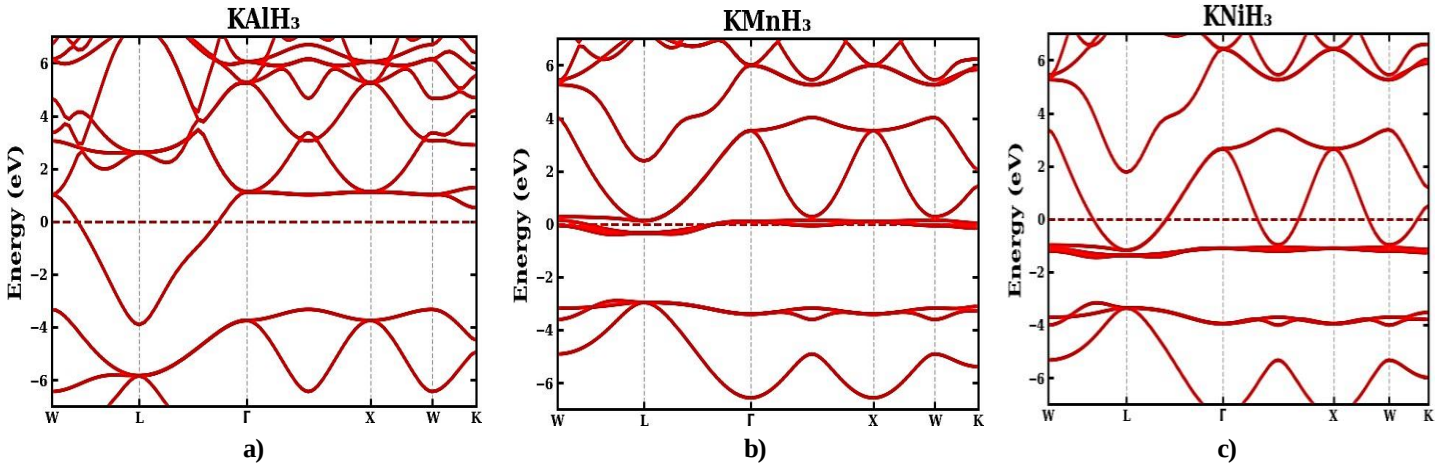

Figure 3. Band Structures of a) $KAlH_3$; b) $KMnH_3$ and c) $KNiH_3$

3.3 Thermoelectric Properties

Figure 4 illustrates the evolution of the electrical conductivity of KXH_3 compounds (X = Al, Mn, and Ni) in a temperature range from 300 to 900 K. The graph reveals that $KAlH_3$ has the highest conductivity by a wide margin, followed by $KMnH_3$ and finally $KNiH_3$. For the three compounds, the value of the conductivity exhibits a slight increment with an increase in temperature. The notable differences in the trends are an indication of the influence of the X site on the electron conductivity. The high value of electrical conductivity for $KAlH_3$ suggests high mobility of electrons in the compound, which may be attributed to band dispersion or low electron scattering. However, the low conductivity of $KNiH_3$ suggests localized electron states, which are commonly seen in transition metal ions. The conductivity of $KMnH_3$ lies in between and is more favorable than $KNiH_3$. The increase in conductivity values at higher temperatures suggests that the three compounds exhibit metallic behavior, and the observed temperature dependence is described within the Boltzmann transport framework under the constant relaxation time approximation. The result indicates that the three compounds increase in conductivity due to an increase in heat input, which makes them favorable for applications in high-temperature thermoelectric devices. A difference in the conductivity trends of $KAlH_3$, $KMnH_3$, and $KNiH_3$ suggests a direct influence of atomic replacement on the Fermi level localized densities of states. Specifically, the use of a transition metal decreases the conductivity due to localization. From the above discussion, there is an indication that $KAlH_3$ has better performance than $KMnH_3$ and $KNiH_3$ for applications demanding high values of conductivity.

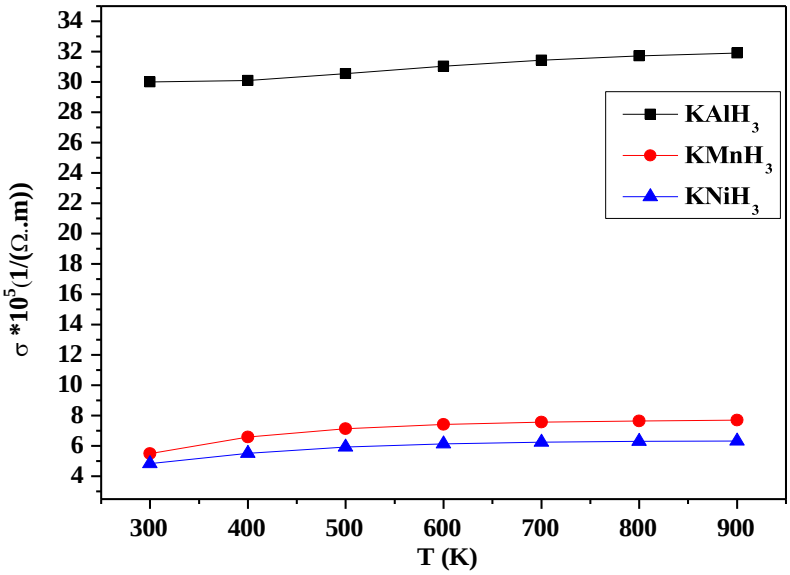

Figure 4. Electrical conductivity (σ) of KXH_3 (X = Al, Mn, Ni) as a function of temperature (300–900 K), calculated using Boltzmann transport theory.

Figure 5 illustrates the evolution of thermal conductivity *K*t of compounds KXH_3 (with X = Al, Mn, and Ni) as a function of temperature in the range 300–900 K. There are three separate curves for the thermal conductivity of each compound, viz., $KAlH_3$, $KMnH_3$, and $KNiH_3$. The thermal conductivity of the former compound remains highest throughout. For the latter two compounds, the thermal conductivity remains lower but almost equal with a steady increment. The steady increase in temperature shows that these three materials become better heat carriers above a certain temperature, presumably due to enhanced energy transport within the lattice. The thermal conductivity of the former compound remains highest, implying that it has a crystal structure that permits efficient heat transport. For the latter two compounds, the lower conductivity implies that heat transport is more strongly hindered because of the presence of Mn and Ni ions. The closer curves between the two species indicate that they may have nearly identical thermal properties. The clear difference between them indicates that the replacement of the metal ion X has greatly affected the thermal properties. The

steady increment of the curves implies that there is no thermal saturation region for these materials up to that range of temperatures. Hence, it can be concluded that the thermal conductivity of the compound $KAlH_3$ severely surpasses the latter two, implying that they may be less efficient thermal conductors. Therefore, these hydrides may have different efficiencies for thermoelectric applications.

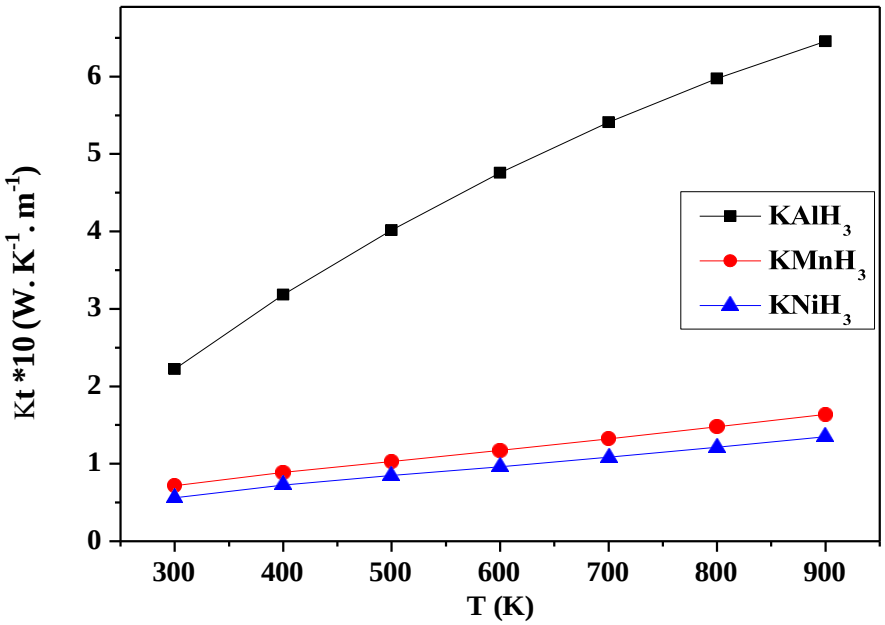

Figure 5. Thermal Conductivity of KXH_3 (X=Al, Mn, and Ni) as a function of temperature (300–900 K), calculated using Boltzmann transport theory.

Figure 6 shows the evolution of the thermoelectric figure of merit ZT of KXH_3 compounds (X = Al, Mn, and Ni) as a function of temperature between 300 and 900 K. The curves indicate a gradual increase in ZT for all three materials as the temperature rises. The $KMnH_3$ compound achieves the highest values at high temperatures, followed by $KAlH_3$, while $KNiH_3$ has the lowest values. This figure highlights the influence of the nature of element X on thermoelectric performance.

$$\mathbf{Zt} = \frac{\boldsymbol{\sigma s^2 T}}{\boldsymbol{\kappa}} \quad (1)$$

Where **S** represents the Seebeck coefficient, **σ** denotes the electrical conductivity, **T** stands for the temperature, and **κ** represents the thermal conductivity. A high **ZT** value signifies efficient thermoelectric performance in a material, characterized by high electrical conductivity, low thermal conductivity, and a substantial Seebeck coefficient.

The better performance of $KMnH_3$ can be related to the optimal balance between moderate electrical conductivity, relatively low thermal conductivity, and high Seebeck coefficients. The $KAlH_3$ compound with high electrical conductivity has a slightly lower ZT because of the high thermal conductivity. On the other hand, the $KNiH_3$ compounds possess the lowest ZT values, possibly because of lower electrical conductivity and poorer diffusion of heat. The increase of ZT with temperature indicates an improvement in thermoelectric performance at elevated temperatures. All these observations suggest that the addition of Mn atoms at site X of the crystal structure further favors the transport properties of $KMnH_3$ over the other compounds.

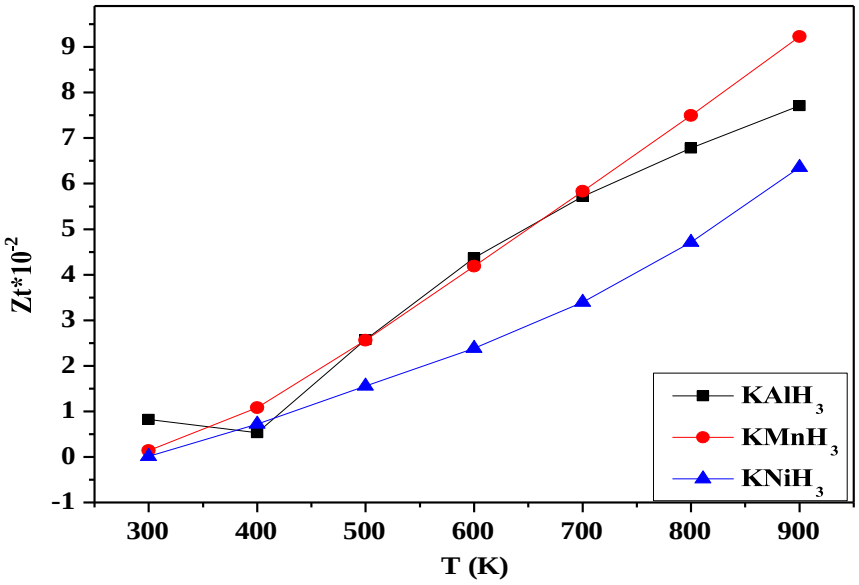

Figure 6. Merit Factor of KXH_3 (X=Al, Mn, and Ni) as a function of temperature (300–900 K), calculated using Boltzmann transport theory.

Figure 7 shows the evolution of the thermoelectric power factor (PF) of KXH_3 compounds (X = Al, Mn, and Ni) as a function of temperature between 300 and 900 K. The curves show a general increase in PF with rising temperature for all three materials. The $KAlH_3$ compound displays the highest values across the entire temperature range. In contrast, $KMnH_3$ and $KNiH_3$ display lower values, with $KNiH_3$ remaining the least efficient. The PF is explained by the following equation:

$$\textbf{Power factor (PF)} = \sigma S^2 \quad (2)$$

The temperature dependence of the power factor indicates an enhancement of the power factor with increasing temperature, signifying an enhancement of the electronic contribution to thermoelectric properties primarily due to an enhancement in electrical conductivity and the Seebeck coefficient. The outstanding property of $KAlH_3$ points towards a synergy of high electrical conductivity and a comparatively high value of the Seebeck coefficient. However, an apparent reduction in the values of $KMnH_3$ and $KNiH_3$ can be attributed to lower electrical conductivity and a reduced role of the electronic component. The quasi-monotonic increase in the power factor indicates a stability of the electronic transport channels in the investigated temperature interval. The increasing distance of $KAlH_3$ from otherwise similar substances dictates a primary role of element X in modifying electronic properties. Based on these data, it can be deduced that $KAlH_3$ is a substance of paramount importance in terms of power factor. However, an increasing trend in the power factor of $KMnH_3$ and $KNiH_3$ at elevated temperatures indicates a possible optimization of these substances via doping.

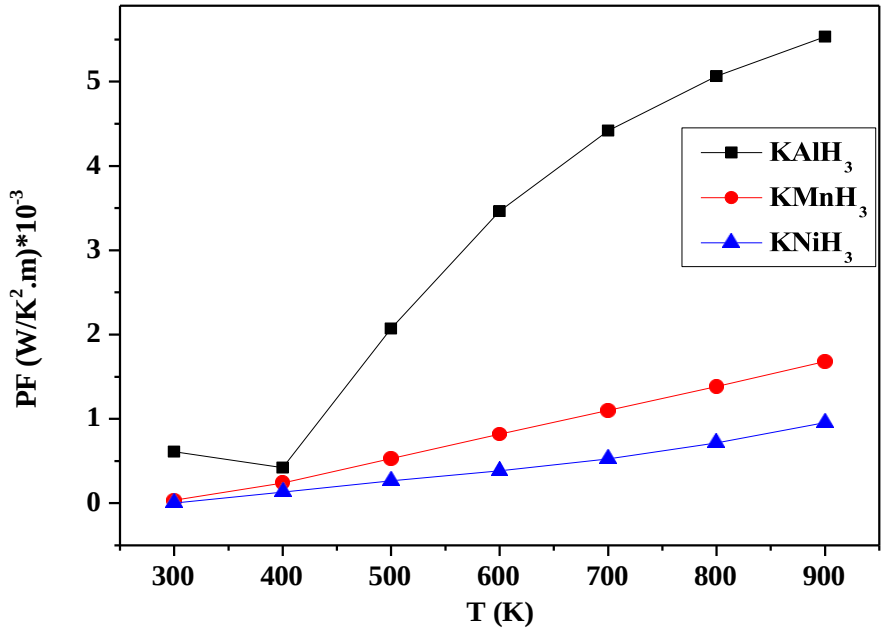

Figure 7. Power Factor of KXH_3 (X=Al, Mn, and Ni) as a function of temperature (300–900 K), calculated using Boltzmann transport theory.

In addition to their thermoelectric properties, the investigated KXH_3 (X=Al, Mn, and Ni) compounds present interesting features for hydrogen storage applications. The perovskite structure provides a stable framework that can accommodate hydrogen atoms within the lattice. The nature of the X–H bonding plays a crucial role in determining hydrogen storage performance. In $KAlH_3$, the stronger covalent interaction between Al and H suggests enhanced hydrogen stability, which may improve storage capacity but could require higher temperatures for hydrogen release. In contrast, $KMnH_3$ and $KNiH_3$, characterized by significant d-orbital contributions near the Fermi level, may exhibit different hydrogen desorption behaviors due to enhanced electronic screening and weaker directional bonding. These results indicate that chemical substitution at the X-site can influence not only electronic and thermoelectric properties but also hydrogen storage characteristics. However, further investigations such as hydrogen desorption energy and thermodynamic stability calculations are required to fully assess their practical storage performance.

4. Conclusion:

In this work, a systematic investigation of the structural, electronic, thermal, and thermoelectric properties of KXH_3 (X = Al, Mn, and Ni) perovskite hydrides has been carried out using density functional theory combined with Boltzmann transport theory. The structural results confirm the stability of all compounds in the cubic perovskite phase, highlighting the role of the X element in shaping the X–H bonding and the overall lattice characteristics. The analysis of band structures and density of states reveals a clear evolution of the electronic behavior with chemical substitution. $KAlH_3$ exhibits relatively high electrical conductivity compared to $KMnH_3$ and $KNiH_3$. The thermal transport analysis indicates that $KAlH_3$ possesses the highest thermal conductivity, whereas $KMnH_3$ and $KNiH_3$ exhibit reduced thermal conductivity, which is beneficial for thermoelectric performance. As a result, $KMnH_3$ achieves the most favorable figure of merit (ZT) at high temperatures, owing to a balanced combination of electrical conductivity, Seebeck coefficient, and low thermal conductivity. Overall, the present results suggest that chemical substitution at the X-site is an effective strategy for tuning the electronic and thermoelectric properties of KXH_3 hydrides. In particular, $KMnH_3$ appears to be a promising candidate for high-temperature thermoelectric applications. Furthermore, the interplay between bonding characteristics and electronic structure indicates a potential relevance of these materials for hydrogen storage applications. In this work, hydrogen storage potential is discussed qualitatively based on structural and electronic features; a detailed quantitative analysis (e.g.,

hydrogen adsorption/desorption energies) is beyond the scope of this study and will be addressed in future work. However, additional investigations, including thermodynamic and kinetic analyses of hydrogen absorption and desorption, are required to fully assess their practical applicability. These findings provide useful insights for the design and optimization of multifunctional hydride materials through compositional tuning and structural engineering.

Funding: The authors are warmly grateful to the support of "The Moroccan Association of Sciences and Techniques for Sustainable Development (MASTSD), Beni Mellal, Morocco"

References

[1] B. N. Tackie-Otoo, M. Mahmoud, and A. Raza, "Renewable energy versus hydrogen energy: assessing current needs for sustainable energy solutions," *Energy & Fuels*, vol. 39, no. 37, pp. 17730–17762, 2025, doi: 10.1021/acs.energyfuels.5c03207.

[2] A. Erdoğdu, F. Dayi, A. Yanik, F. Yildiz, and F. Ganji, "Innovative solutions for combating climate change: Advancing sustainable energy and consumption practices for a greener future," *Sustainability*, vol. 17, no. 6, p. 2697, 2025, doi: 10.3390/su17062697.

[3] R. Angelico, F. Giametta, B. Bianchi, and P. Catalano, "Green hydrogen for energy transition: A critical perspective," *Energies*, vol. 18, no. 2, p. 404, 2025, doi: 10.3390/en18020404.

[4] K. S. Nivedhitha et al., "Carbon-based and metal hydride materials for advanced hydrogen storage: progress, challenges and future directions," *Sustainable Energy & Fuels*, vol. 9, no. 19, pp. 5199–5217, 2025, doi: 10.1039/D5SE00916B.

[5] C. A. Mukwanje, A. Faik, and M. Nachtane, "Current progress, challenges, and future prospects in composite cryogenic hydrogen storage tanks," *Polymer Composites*, 2025, doi: 10.1002/pc.29872.

[6] D. Otegen, A. Shadykulova, K. Turgunova, and S. Zholdayakova, "Recent advances in solid-state hydrogen storage materials," in *Proc. SPE Annual Caspian Technical Conference*, 2025, p. D031S022R002, doi: 10.2118/230472-MS.

[7] A. Koufi, Y. Ziat, H. Belkhanchi, and A. Bouzaid, "Investigation of thermoelectric and structural properties of $BeAlH_3$, $BeGaH_3$, and $BeInH_3$ perovskite hydrides for energy applications," *Solar Energy and Sustainable Development Journal*, vol. 14, pp. 1–14, 2025, doi: 10.51646/jsesd.v14iSTR2E.786.

[8] N. Noureddine, Y. Ziat, H. Belkhanchi, and A. Koufi, "DFT approach for improving the electronic and optical properties of $KZnF_3$ perovskite: impact of copper doping," *Solar Energy and Sustainable Development Journal*, vol. 14, pp. 51–66, 2025, doi: 10.51646/jsesd.v14iSTR2E.798.

[9] P. Blaha, K. Schwarz, F. Tran, R. Laskowski, G. K. H. Madsen, and L. D. Marks, "WIEN2k: An APW+lo program for calculating the properties of solids," *The Journal of Chemical Physics*, vol. 152, no. 7, 2020, doi: 10.1063/1.5143061.

[10] N. Xu et al., "First-principles study on hydrogen storage properties of the new hydride perovskite $XAlH_3$ (X = Na, K)," *International Journal of Hydrogen Energy*, vol. 60, pp. 434–440, 2024, doi: 10.1016/j.ijhydene.2024.02.148.

[11] R. Song et al., "First-principles investigation for the hydrogen storage, mechanical, electronic, optical, dynamic, and thermodynamic properties of $XMnH_3$ (X = Na, K, Rb) perovskites for hydrogen storage applications," *Vacuum*, vol. 222, p. 113007, 2024.

[12] A. Gencer and G. Sürücü, "Investigation of structural, electronic and lattice dynamical properties of $XNiH_3$ (X = Li, Na and K) perovskite type hydrides and their hydrogen storage applications,"

International Journal of Hydrogen Energy, vol. 44, no. 29, pp. 15173–15182, 2019, doi: 10.1016/j.ijhydene.2019.04.097.

[13] M. A. Rehman et al., "KXH_3 (X = Ca, Sc, Ti, Ni) hydride perovskites: A DFT study for physical properties and hydrogen storage capability," 2023, doi: 10.21203/rs.3.rs-3670975.

[14] R. Song, N. Xu, Y. Chen, S. Chen, W. Dai, and W. Zhang, "First-principles study on hydrogen storage properties of the new hydride perovskite $XAlH_3$ (X = Na, K)," *International Journal of Hydrogen Energy*, vol. 60, pp. 434–440, 2024, doi: 10.1016/j.ijhydene.2024.02.148.

The Use of Solar Cells Based on pCdTe – nCdS and pCdTe – nCdSe Heterostructures and Their Application in Renewable Energy Sources

C.M. Otajonov[*1], *R.N. Ergashev*[1], *S.K. Berdibekova*[2], *K.A. Botirov*[1], *B.X. Karimov*[1], *M.X.Raxmonkulov*[1]

[1]150100 Fergana, Murabbilar Street - 19, Uzbekistan.
[2]723500 Osh, Isanova Street - 81, Kyrgyzstan.
[*] otajonov_s@mail.ru

Abstract. The paper considers a photovoltaic module of a solar cell, which is the first to be used in renewable energy sources, based on p-CdTe–n-CdS and p-CdTe–n-CdSe heterostructures, which have high-energy characteristics. It is shown that under illumination such elements generate a voltage of 200–300 V (approximately 0.4–0.8 V under load) and currents of the order of 10^{-11} A, the values of which depend on the surface area and light intensity. It has been established that the presence of deep impurity levels in CdTe films enhances photoconductivity and output signals due to the additional excitation of charge carriers. Various schemes of serial and parallel connections of heterostructure solar cells are considered, enabling the adjustment of voltage and current. Special attention is paid to the problem of reverse bias and its solution using shunt diodes or modern solar battery controllers. The proposed module is used in renewable energy sources and also provides prospects for its long-term use at any time of the year.

1 Introduction

Current trends in renewable energy development require the development of new types of photovoltaic converters with high efficiency and the potential for application in various industries [1]. One promising area is the use of thin-film solar cells based on heterostructures [2]. Of particular interest are the p-CdTe–n-CdS and p-CdTe–n-CdSe structures, which combine a wide spectral absorption range and the presence of deep impurity levels that enhance photoconductivity.

The problem of air pollution is also becoming increasingly important, necessitating the development of new sensor systems for its monitoring. Combining the functions of electrical energy generation and environmental monitoring opens up opportunities for the development of hybrid systems. In this regard, the study of photovoltaic modules based on CdTe heterostructures has both scientific and applied significance. Based on the above, we consider below a combination of solar cells based on pCdTe–nCdS and pCdTe–nCdSe with deep impurity levels [3].

Our CdTe films generate from 200 V to 300 V over an area of 1 cm², as found in the work of Goldstein and Pensak as anomalous photovoltage, and we use these methods in their work, but they have a low current of 10^{-11} A. In our case, connecting the elements in series can increase the current by 1.5 times due to the generation of charge carriers from deep impurity levels located in the CdTe depleted band [4].

It is clear that a 20x20 cm² cell is sixteen times larger than a 5x5 cm² cell, and therefore produces six times more current. [5]. The current also depends on the wavelength of the light and its intensity, and is directly proportional to the radiation intensity. The brighter the light, the greater the current generated by the solar cell [6].

2 Research methodology

Recent years have seen intense research into methods for producing CdTe films based on Group I compounds with photovoltaic properties. While similar coating parameters were used in certain studies, different characteristics were identified using different indicators. Methods for producing high-quality films involve a working chamber used to create controlled and activated photosensitive films. A vacuum of approximately 10^{-5} mm Hg was maintained within the setup where the semiconductor materials and impurities were deposited. The chamber itself was constructed of glass, quartz, or metal with a transparent section in the form of a cylindrical lid 15 cm in diameter and 35 cm in height. The substrates were secured to a frame, which served as a holder and was positioned within the working vacuum chamber at a height of approximately 15-20 cm above its base. The distance between the frame and the crucible ranged from 4.5 to 6.0 centimeters, and the sputtering angle could be varied from zero to 90 degrees by rotating the holder. Temperature was maintained using a substrate-holding device. These devices were used to regulate the base temperature using chromel-aluminum thermocouples. Crucibles were made from tungsten or molybdenum wire with a diameter of 0.5 mm and shaped like conical baskets with a surface area of 50 mm² for evaporation of the CdTe semiconductor material and its impurities. An aqueous mixture of beryllium or aluminum oxides was applied to the basket to optimize the temperature [7].

3 Experimental results and discussion

The current and signal increase due to the excitation of charge carriers not only from the intrinsic region but also from the impurity absorption region, which is formed by deep impurity levels introduced during the fabrication of the cadmium telluride heterostructure [8].

CdTe-based solar cells typically have a relatively low output voltage per cell (approximately 0.4–0.8 V under load). Therefore, to achieve the required electrical parameters in practical photovoltaic modules, a series and parallel connection of a large number of cells is used, allowing the output voltage and current to be adjusted depending on load requirements.

Figure 1 shows a series connection of pCdTe-nCdS and pCdTe-nCdSe solar cells with deep impurity levels, which allows for an increase in voltage without changing the current in the circuit.

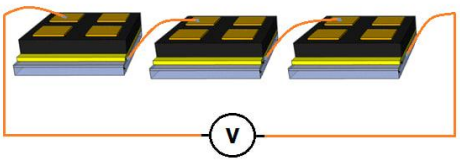

Fig. 1. Series connection of solar cells based on pCdTe – nCdS and pCdTe – nCdSe with deep impurity level

Heterojunction solar cells can be connected in series and parallel to increase their output characteristics [9].

The output current depends on the cell's surface area, so a natural way to increase current is to increase the cell (or cells) surface area.

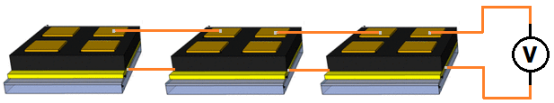

Fig. 2. Parallel connection of solar cells

If you take three 5x5 cm² CdTe-CdS laminated elements and connect them in parallel as shown in Figure 2, you can get the same result as replacing four elements with one 5x15 cm² element (in both cases the surface area is the same, 75 cm²) [10].

It's important to understand that parallel connection only increases the current, not the voltage. Regardless of the number of elements connected in parallel (4 or 50), the generated voltage will be no more than 0.5 V [11].

Other connection types are also possible, and their choice should be determined by the specific operating conditions of the device, as shown in Figure 3 [12].

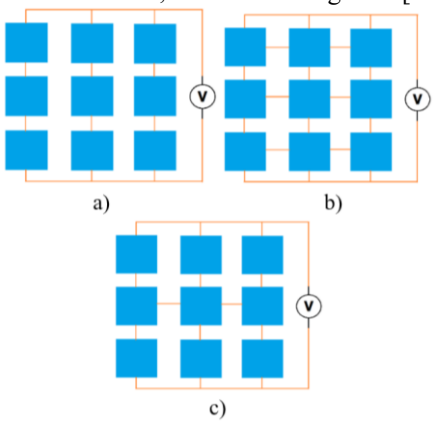

Fig. 3. Schemes of methods for connecting heterostructure solar cells to a battery

When working with CdTe heterojunction solar cells, phenomena typically occur that are not observed with continuous power sources [13]. This phenomenon is associated with so-called reverse bias. To understand this, let's look at Figure 4.

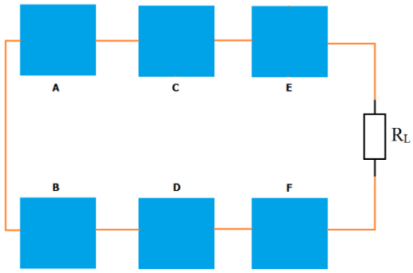

Fig. 4. Six series-connected heterojunction solar cells and a load

Figure 4 shows six cells connected in series. The total output voltage of the string is 4 V, and resistor RL is connected as a load. When RL is applied, the voltage in new CdTe heterojunction cells, for example, 400 V, decreases a hundredfold, and the current increases similarly. Furthermore, due to the excitation of charge carriers from deep impurity levels (the impurity effect), the current flow increases by 1.5 times, resulting in maximum solar energy utilization [14].

If we shade solar cell D with an opaque object, such as a hand, we see that the voltage drop is not very large.

A solar cell that does not produce electrical energy is a link with high internal resistance, not a short circuit. The same thing happens as when a switch is opened, but the switch is not fully open—a small current flows through it.

In most cases, the effective resistance of a shaded solar cell is many times greater than the value of the load resistor RL. Therefore, RL can be practically considered as a piece of wire connecting the negative and positive terminals. This means that element D now acts as the load.

As a result, element D heats up and, if heated sufficiently, can fail (explode). This leaves us with a series-connected battery with one inactive cell—an unenviable situation.

An effective solution to this problem is to connect shunt diodes in parallel across all the cells, as shown in Figure 5 [15].

The diodes are connected so that when the solar cell is operating, they are reverse-biased by the cell's voltage. Therefore, no current flows through the diode, and the battery functions normally.

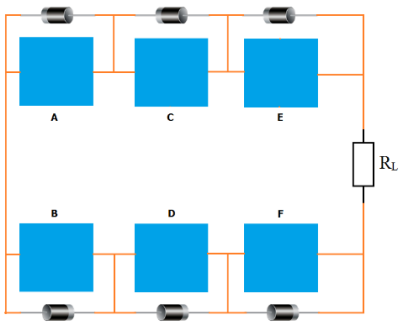

Fig. 5. Parallel connection of shunt diodes to all heterojunction solar cells

Let's now assume that one of the cells is shaded. This causes the diode to become forward-biased, and current flows through it to the load, bypassing the faulty cell. Of course, the output voltage of the entire circuit will decrease by 0.5 V, but the source of self-destructive force is eliminated.

An additional benefit is that the battery continues to function normally. Without the bypass diodes, it would fail completely.

In practice, it is impractical to bypass every battery cell. Cost considerations must be taken into account, and bypass diodes must be used, achieving a reasonable compromise between reliability and cost. Nowadays, solar panel controllers are used instead of bypass diodes to automatically manage the system's battery charging and eliminate short circuits in solar panels.

When using a heterojunction module in a new type of air pollution detection system, the voltage of the battery supplying the microcontroller platform must be taken into account. The microcontroller platform supplies other system components, such as sensors, a heterojunction photodetector, and a Wi-Fi module for wireless connection. To make the system practical, a block diagram of an air pollution sensor was created on the microcontroller platform using a heterojunction solar module, which is connected via Wi-Fi to the automatic control system, specifically a programmable logic controller (PLC).

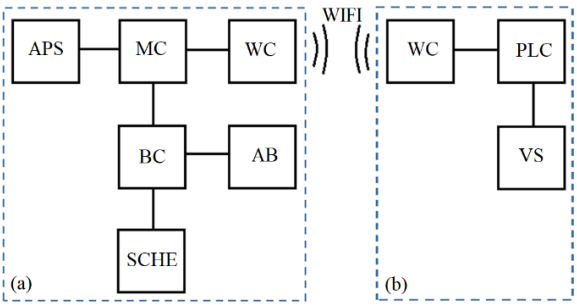

Fig. 6. Block diagram of the air pollution sensor in the platform with a microcontroller using a heterostructure solar module (a) which is connected via WIFI to the PLC automatic control system (b)

Figure 6 shows two units that make up a common ventilation system. Unit (a) houses an air pollution sensor (APS) with a new pCdTe-nCdS and pCdTe-nCdSe heterostructure photodetector with deep impurity levels. After the sensor detects foreign dust or gas particles in the air, a microcontroller (MC) records them. The microcontroller, based on an Atmega chip, transmits them through a wireless network unit (WIFI) to another unit (b) connected to the programmable logic controller (PLC) of the ventilation system (VS) in the premises and workshops of an industrial building.

Unit (a) also houses a battery (AB), a solar battery with pCdTe-nCdS and pCdTe-nCdSe heterostructure elements (SCHE) with deep impurity levels, and a battery controller that monitors the current in the solar and battery batteries. It is known that sunlight contains visible, infrared, and ultraviolet light. Our film heterostructures generate charge carriers not only from the intrinsic region but also from the impurity region of the spectrum, as CdTe films contain deep impurity levels located in the band gap. Photoconductivity σ is directly proportional to the charge carrier concentration and light intensity, according to the well-known formula [16]

$$\sigma = en\mu\beta I, \qquad (1)$$

where e is the electron charge, n is the charge carrier concentration, μ is the charge carrier mobility, β is the quantum yield, and I is the light intensity.

The unit's system operates autonomously, saving on the expense of various metal wires. The autonomous sensor system can also detect air pollution not only indoors but also outdoors. To detect air pollution in open areas, the sensor is installed on the roof of a building or attached to various automated unmanned aerial vehicles (UAVs) or quadcopters.

4 Conclusion

A study of a photovoltaic module based on p-CdTe–n-CdS and p-CdTe–n-CdSe heterostructures revealed that the cells generate a voltage of 200–300 V, with the current determined by the surface area and light intensity. The use of deep impurity levels in CdTe films provides additional excitation of charge carriers, increasing photoconductivity and the output signal. Connecting solar cells in series and parallel allows for targeted modification of the module's characteristics. The problem of reverse bias can be solved by using shunt diodes or solar panel controllers.

The practical significance of this work lies in the potential application of the developed photovoltaic module in environmental monitoring systems to detect air pollution, as well as in the energy sector to improve the efficiency of solar installations.

Author Contributions. C.M. Otajonov conceived the research idea and supervised the study. R.N. Ergashev and K.A. Botirov performed the experimental work and data analysis. S.K. Berdibekova and B.X. Karimov contributed to the interpretation of the results and manuscript preparation. M.X. Raxmonkulov participated in the development of the methodology and editing of the manuscript. All authors have read and approved the final version of the manuscript.

Funding. This research received no external funding.

Data Availability Statement. The data presented in this study are available from the corresponding author upon reasonable request.

Conflicts of Interest. The authors declare no conflict of interest.

Acknowledgments. The authors express their gratitude to the scientific staff of Fergana State University for their support and assistance in conducting this research.

5 References

1. Yang, Y. Current Status and Future Development Trend of Solar Photovoltaic Power Generation. Highlights in Science, Engineering and Technology, Vol. 83 (2024). DOI: https://doi.org/10.54097/191ad426.
2. Mohammad Jafar Molaei, Mohammad Younas, Mashallah Rezakazemi. Van der Waals heterostructures in ultrathin 2D solar cells: State-of-the-art review. Materials Science and Engineering: B Volume 285, November 2022, 115936. DOI: 10.1016/j.mseb.2022.115936
3. Michael A. Scarpulla, Brian McCandless and others. CdTe-based thin film photovoltaics: Recent advances, current challenges and future prospects. Solar Energy Materials and Solar Cells. Volume 255, 15 June 2023, 112289. https://doi.org/10.1016/j.solmat.2023.112289
4. Bibin John, S. Varadharajaperumal. Comprehensive Review on CdTe Crystals: Growth, Properties, and Photovoltaic Application. February 2024, The Physics of Metals and Metallography 124(14). DOI:10.1134/S0031918X2110094X
5. Mahesh Raj Nagaraja, Wahidul K Biswas, Chithirai Pon Selvan. Advancements and challenges in solar photovoltaic technologies: enhancing technical performance for sustainable clean energy – A review. Solar Energy Advances. Volume 5, 2025, 100084. https://doi.org/10.1016/j.seja.2024.100084

6. Masthura, Abdullah. Effect of Temperature and Sunlight Intensity on Surface of Solar Panels on Electric Power Generated. March 2024Journal of Physics Conference Series 2733(1):012029. DOI:10.1088/1742-6596/2733/1/012029
7. R.K.K.G.R.G. Kumarasinghe, P.K.K. Kumarasinghe, R.P. Wijesundera, B.S. Dassanayake. Thermally evaporated CdS/CdTe thin film solar cells: Optimization of CdCl2 evaporation treatment on absorber layer. Current Applied Physics, Volume 33, January 2022, Pages 33-40. https://doi.org/10.1016/j.cap.2021.10.011
8. Luksa Kujovic, Xiaolei Liu, Ali Abbas and others. Achieving 21.4% Efficient CdSeTe/CdTe Solar Cells Using Highly Resistive Intrinsic ZnO Buffer Layers. Advanced Functional Materials published by Wiley-VCH GmbH, 2024, 34, 2312528, pp. 1-8. https://doi.org/10.1002/adfm.202312528
9. R. Mallick, X. Li, C. Reich, X. Shan, and others "Arsenic-doped CdSeTe solar cells achieve world record 22.3% efficiency," IEEE J. Photovoltaics 13(4), pp. 510–515 (2023). https://doi.org/10.1109/JPHOTOV.2023.3282581
10. Norlinda Binti Mohd Yusof, Annuar Bin Baharuddin. The study of output current in photovoltaics cell in series and parallel connections. October 2020, International Journal of Technology Innovation and Humanities 1(1):7-12. DOI:10.29210/88701
11. D. Pokhrel, et al. Copper iodide nanoparticles as a hole transport layer to CdTe photovoltaics: 5.5 % efficient back-illuminated bifacial CdTe solar cells. Sol. Energy Mater. Sol. Cells, 235 (Jan. 2022), p. 111451. https://doi.org/10.1016/j.solmat.2021.111451
12. D. A. Lamb, S. J. C. Irvine, M. A. Baker, C. I. Underwood, and S. Mardhani, "Thin film cadmium telluride solar cells on ultra-thin glass in low earth orbit—3 years of performance data on the AlSat-1N CubeSat mission," Prog. Photovoltaics 29(9), pp. 1000–1007 (2021). https://doi.org/10.1002/pip.3423
13. Alessandro Romeo, Elisa Artegiani. CdTe-Based Thin Film Solar Cells: Past, Present and Future. Energies, March 2021, 14(6). DOI:10.3390/en14061684
14. S. S. Bista, D.-B. Li, S. Rijal, S. Neupane, R. A. Awni, C.-S. Jiang, C. Xiao, K. K. Subedi, Z. Song, A. B. Phillips, X. Wen, R. J. Ellingson, M. J. Heben, and Y. Yan, "Water-assisted lift-off process for flexible CdTe solar cells," ACS Appl. Energy Mater. 6(2), pp. 885–891 (2023). https://doi.org/10.1021/acsaem.2c03287
15. Luthfan Fauzan, Yeon Hyang Sim, Min Ju Yun, Hyekyoung Choi, Dong Yoon Lee, Seung I. Cha. Power from shaded photovoltaic modules through bypass-diode-assisted small-area high-voltage structures. Renewable and Sustainable Energy Reviews. Volume 208, February 2025, 115047. https://doi.org/10.1016/j.rser.2024.115047
16. G. Kartopu, O. Oklobia, D. Turkay, DR Diercks. Study of thin film poly-crystalline CdTe solar cells presenting high acceptor concentrations achieved by in-situ arsenic doping. March 2019, Solar Energy Materials and Solar Cells 194: 259-267. DOI:10.1016/j.solmat.2019.02.025

Comparative Study of Zr/Te Co-Doped $MgTiO_3$: Structural, Electronic, and Optical Properties with Potential Applications

Hajar Motahhir[1,2], *Abdellah* Bouzaid[1,2], *Younes* Ziat [1,2], *Hamza* Belkhanchi[1,2], *Ayoub* Fatihi[1,2], *Youssef* Jouad[1,2], *Charaf* Laghlimi[2,3] *and Zakaryaa* Zarhri[4]

[1]Engineering and Applied Physics Laboratory (EAPL), Superior School of Technology, Sultan Moulay Slimane University, Beni Mellal, Morocco
[2]The Moroccan Association of Sciences and Techniques for Sustainable Development, Beni Mellal 23000, Morocco
[3]ERCI2A, FSTH, Abdelmalek Essaadi University, Tetouan, Morocco
[4]SECIHTI-Faculty of Chemical Sciences and Engineering, The Autonomous University of the State of Morelos (UAEM), Morelos, Cuernavaca, 62209, Mexico

Abstract. This study investigates the structural, electronic, and optical properties of pristine and Zr/Te co-doped $MgTiO_3$ using first-principles calculations based on density functional theory (DFT). The calculations were performed within the full-potential linearized augmented plane wave (FP-LAPW) method implemented in the WIEN2k code. Structural optimization was carried out using the generalized gradient approximation (GGA), while the Tran–Blaha modified Becke–Johnson (TB-mBJ) potential was employed to obtain improved electronic and optical properties. The optimized lattice parameter of pristine $MgTiO_3$ was found to be a = 3.8427 Å. The calculated band gap of undoped $MgTiO_3$ is 2.93 eV, confirming its wide-band-gap semiconducting nature with predominant ultraviolet absorption. Upon Zr and Te co-doping, the band gap significantly decreases to 1.15 eV for $Mg_8Ti_7Zr_1O_{23}Te_1$ and further to 0.64 eV for $Mg_8Ti_7Zr_1O_{22}Te_2$ due to dopant-induced electronic states near the Fermi level. Electronic structure analysis reveals strong hybridization between Te-p, O-p, Ti-d, and Zr-d orbitals, leading to band gap narrowing and a transition toward a direct band gap character. Optical calculations based on the complex dielectric function show a pronounced red shift of the absorption edge from the ultraviolet to the visible region, accompanied by an increase in the static dielectric constant and optical conductivity at low photon energies. These results demonstrate that Zr/Te co-doping effectively tunes the electronic structure and enhances visible-light absorption in $MgTiO_3$, highlighting its potential for optoelectronic and energy-related applications.

1. Introduction:

The development of advanced functional materials is a key driver for emerging technologies in electronics, optoelectronics, and energy conversion. Among these

materials, oxide perovskites have attracted considerable attention due to their structural flexibility, thermal stability, and tunable electronic properties [1, 2, 3], rendering them viable choices for applications like capacitors, resonators, and PV devices.

On the other hand, the oxide perovskites have relatively low absorption in the visible region. Recently, elemental doping/codoping has emerged as an alternative to enhance the performance of these compounds. $MgTiO_3$ is of interest due to the high stability of the structure as well as the favorable electronic properties of the compound. Codoping of $MgTiO_3$ with Zr on the Ti site and Te on the oxygen site can simultaneously optimize the cationic as well as the anionic lattices of the compound. Substitution of Ti^{4+} ions by Zr4+ ions can create lattice distortions as well as affect the conduction band of the compound, while the presence of Te can add more states to the p-band of the compound. These effects can reduce the bandgap of the compound, thus enhancing the visible region absorption as well as the separation of the charge carriers, which is necessary for photovoltaic as well as PC applications [4, 5].

$MgTiO_3$, an ilmenite-structured perovskite with high dielectric constant, low dielectric loss, and superior thermal stability, shows an intrinsic band gap of 3.4–3.7 eV, restricting the absorption of light within the range of the electromagnetic spectrum. The electronic and optical properties of $MgTiO_3$ have to be engineered through doping to precisely calculate the structural parameters in the state of equilibrium.

Magnesium titanate ($MgTiO_3$), an ilmenite-type perovskite demonstrates a high dielectric constant, minimal dielectric loss, and superior thermal stability. Its intrinsic band gap (approximately 3.4–3.7 eV) limits visible-light absorption, motivating efforts to tailor its electronic and optical properties through doping.

Other studies on codoping with Se and Zr [6] reported that this converts $MgTiO_3$ from an indirect band gap of 2.93 eV to a direct band gap of 2.159 to 1.726 eV. This improves optical conductivity and visible-light absorption and gives a good match between the band edges and the redox potential of water, leading to greater H_2 and O_2 evolution. $MgTiO_3$ with Se/Zr doping may therefore be a good choice for uses to create hydrogen with solar energy or for optoelectronic tools. When appropriately modified, $MgTiO_3$ is a promising candidate for PV and light- emitting devices, as well as plasma displays, flat-panel displays, solid-state lighting, and optical applications [7]. Furthermore, its elevated dielectric constant and minimal dielectric loss render $MgTiO_3$ appropriate for dielectric resonators in integrated circuits and wireless communication systems, and global positioning systems [8, 9]. In addition, the low dielectric loss and high thermal stability render $MgTiO_3$ an attractive material for ceramic capacitors and resonators operating at high frequencies.

Recent advances in the design of doped titanate perovskites have demonstrated that co-doping is an effective strategy to tailor their optoelectronic and photocatalytic properties. In particular, the work of Bouzaid et al. [10] on Zr/Te co-doped $ATiO_3$ (A = Ca, Sr) revealed a significant band gap reduction and improved visible-light absorption, making these materials promising for solar-driven hydrogen production and optoelectronic applications. Similarly, Bouzaid et al. [6] reported that Se/Zr co-doping in $ATiO_3$ perovskites induces impurity states near the band edges, enhancing optical absorption and charge carrier separation. These studies highlight the key role of transition metal and

chalcogen co-doping in modulating the electronic structure through orbital hybridization effects. In this context, the present work extends these investigations to $MgTiO_3$ by exploring Zr/Te co-doping, aiming to further understand and optimize the relationship between dopant-induced electronic states and optoelectronic performance.

In the first part of this paper, the optoelectronic properties of undoped $MgTiO_3$ and Zr/Te co-doped $Mg_8Ti_7Zr_1O_{23}Te_1$ and $Mg_8Ti_7Zr_1O_{22}Te_2$ compounds are investigated using DFT based on the GGA-mBJ potential. The optimized crystal structure yields a lattice constant of a = 3.8427 Å. The calculated band gaps for $MgTiO_3$, $Mg_8Ti_7Zr_1O_{23}Te_1$, and $Mg_8Ti_7Zr_1O_{22}Te_2$ are 2.93 eV, 1.15 eV, and 0.64 eV, respectively, indicating the effectiveness of Zr and Te codoping in tuning the electronic properties of $MgTiO_3$.

The present work seeks to provide insights into the structural and optoelectronic properties of $MgTiO_3$. The role of codoping Zr and Te dopants in improving the optoelectronic properties of $MgTiO_3$ is discussed in detail, and a plausible way to design materials for advanced electronics and photonics is provided.

2. Computational method:

DFT inside the FP-LAPW approach, as implemented in the WIEN2k code, was used to examine the structural and optoelectronic characteristics of both undoped $MgTiO_3$ and Zr/Te co-doped $MgTiO_3$. For the cubic perovskite structure, the primitive unit cell belongs to the space group Pm-3m (No. 221). A 2 × 2 × 2 supercell containing 40 atoms ($Mg_8Ti_8O_{24}$) was constructed to model doping concentrations. Co-doping was carried out using Zr and S replacements in two configurations: (i) 12.5% Zr and 4.16% Te and (ii) 12.5% Zr and 8.33% Te, with Zr replacing Ti and Te replacing O. In addition, utilizing the GGA, the atomic locations and unit-cell geometry were optimized. The optoelectronic properties were calculated using the TB-mBJ exchange–correlation potential. To overcome the well-known band-gap underestimation of standard GGA. The wave functions were expanded in the interstitial region using a plane-wave cutoff defined by $RMT \times K_{max} = 7$. The RMT was optimized to avoid any overlap between muffin-tin spheres. For Mg, Ti, Zr, O, and Te elements, the chosen muffin-tin radii were 2.42, 1.80, 1.92, 1.71, and 1.85 a.u., respectively.

The Brillouin zone was sampled using the Monkhorst–Pack scheme along the high-symmetry path. For the primitive unit cell, a 10 × 10 × 10 k-point mesh was employed. For the 2 × 2 × 2 supercell, a mesh containing 1000 k points was used for geometry optimization, while the same dense k-point sampling was adopted to calculate high-resolution electronic and optical properties. SCF cycles were considered converged when the total energy and total charge density reached thresholds of 10^{-5} Ry and 10^{-4} e, respectively. Furthermore, VESTA was utilized to visualize the crystal structure of the materials [11].

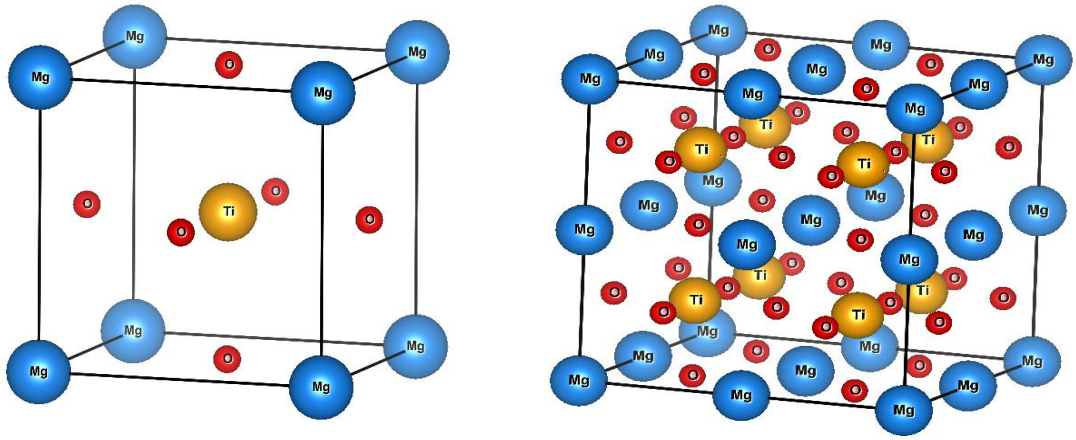

a) **b)**

Figure 1: Crystal structure of $MgTiO_3$ includes (a) the unit cell and (b) the 2 × 2 × 2 supercell used for co-doping.

3. Results and discussion:

3.1 Structural properties:

Magnesium titanate ($MgTiO_3$) belongs to the perovskite-type family, characterized by a cubic crystal structure within the Pm-3m space group (no. 221). In the ideal unit cell, the Mg atoms occupy the corners at coordinates (0, 0, 0), the Ti atoms are positioned at the center (1/2, 1/2, 1/2), and the O atoms are located at the face-centered positions (1/2, 1/2, 0). To investigate co-doping effects, a 2*2*2 supercell was constructed where one Ti^{4+} cation is replaced by Zr^{4+} and two O^{2-} anions are substituted by Te^{2-} atoms, as illustrated in Figure 1. Despite local lattice distortions caused by the larger ionic radii of the dopants, the structural integrity of the perovskite framework remains intact, enabling the optimization of the material for optoelectronic applications.To properly identify the equilibrium structural characteristics, total energy was calculated as a function of unit cell volume. The total energy–volume data were fitted using the Birch–Murnaghan equation of state [12], expressed as Equation (1).

$$E(V) = E_0 + \frac{B_0 V}{B_0'}\left[\frac{\left({}^{V_0}/_{V}\right)^{B_0'}}{B_0'-1} + 1\right] - \frac{B_0 V_0}{B_0'-1} \quad (1)$$

Here, E(V) is the total energy of the system corresponding to a specific volume V, whereas E_0 is the minimum energy corresponding to the equilibrium volume V_0. In addition, B_0 is the bulk modulus of the system and has a pressure derivative denoted by B'. The above equation helps us understand the stability of the system, and hence, the robustness of the system is assessed. Figure 2 shows the correlation between the total energy of $MgTiO_3$ and its volume. The minimum of the curve identifies the equilibrium lattice constant a = 3.8427 Å, which is in good agreement with available theoretical studies. Additionally, the calculated formation energy (Ef = -3.05 eV/atom) confirms the thermodynamic stability of $MgTiO_3$, consistent with previous literature [13].

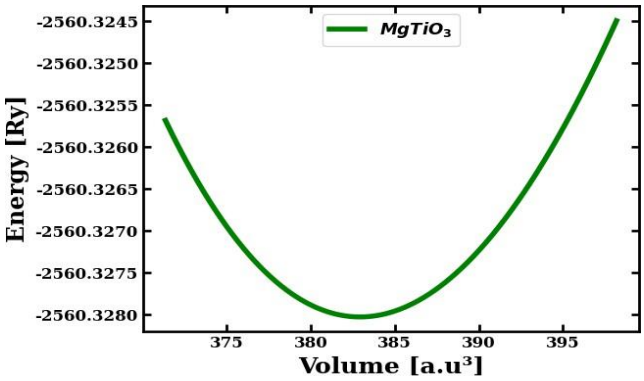

Figure 2: Fluctuation of the total energy of $MgTiO_3$ in relation to unit cell volume.

3.2 Electronic properties

Band structures of pristine and (Zr, Te) co-doped $MgTiO_3$ in their electronic configuration were calculated using TB-mBJ exchange-correlation functions. The energy dispersion was also examined along high-symmetry directions in the first Brillouin zone of the material's unit cell, while setting EF = 0 eV as shown in Figure 3.

Table 1 summarizes the calculated Eg of all materials. The codoped material exhibited a reduced Eg compared to the undoped $MgTiO_3$ (Table 1). This is because the inclusion of the electronic states of the dopant in the compound's energy structure occurs due to the fact that the compounds used for doping in the present study were present in the interstitial position and thus alter the density of the states present in the compound's structure. The optoelectronic properties of the compound. For the pristine compound $MgTiO_3$, the compound has an indirect energy gap structure, and the VBM for the compound occur at the L-point, while the for the compound occur at the Γ-point in the Brillouin zone. Calculated band gap energy for the compound using the TB-mBJ functional has the value 2.93 eV and agrees well with the earlier findings for the compound having the titanate perovskite structure [6]. This relatively wide band gap indicates that undoped $MgTiO_3$ predominantly absorbs ultraviolet radiation.

Upon simultaneous substitution of Ti by Zr and O by Te, a pronounced reduction in the band gap energy is obtained. As summarized in Table 1, the band gap decreases to 1.15 eV for $Mg_8Ti_7Zr_1O_{23}Te_1$ and further narrows to 0.64 eV for $Mg_8Ti_7Zr_1O_{22}Te_2$. This band gap narrowing originates from the appearance of dopant induced electronic states within the forbidden gap. In particular, the Te-5p orbitals introduce states near the top of the VB, while the Zr-4d states strongly hybridize with the Ti-3d orbitals at the bottom of the CB.

Moreover, the co-doped systems exhibit a transition from an indirect to a direct band gap, with the VBM and CBM located at the Γ point. This transition can be attributed to dopant-induced modifications in the local crystal field environment and enhanced orbital hybridization, which alter the electronic symmetry of the host lattice. The emergence of a direct band gap is highly desirable for optoelectronic applications, as it facilitates efficient optical transitions and improves charge carrier generation.

Thus, the present modification and narrowing of the band gap through the co-doping of Zr and Te highlight a successful method of tuning the electronic structure and band gap of $MgTiO_3$. This control over the band structure is vital for the charge carrier dynamics and light absorption processes, making it a potential candidate for optoelectronic applications and optical sensors. Such results confirm that the chemical and structural changes brought about by co-doping can considerably modify the electronic structure and optical properties of the material and provide excellent potential for advanced technological applications.

The TDOS and PDOS depicted in Figure 4 provide further insight into the evolution of electronic structure. The computed TDOS and PDOS for Zr- and Te-co-doped $MgTiO_3$ show the contribution of the atomic orbitals of the different elements to the electronic states and the energy level of the electronic transitions that occur from the VB to the CB of the material. The following results show that co-doping affects the electronic structure. Figures 4 show the and TDOS, respectively, of the pure and Zr/Te co-doped $MgTiO_3$. The TDOS is shown from -6 eV to 6 eV. In the case of $MgTiO_3$ being undoped, the VB mainly consists of O-p, while the CB consists of Ti-d. O-p and Ti-d orbitals hybridize to a high level toward suggesting that oxygen and titanium couple electronically in a strong way. Zr and Te co-doping additionally contributes to electronic coupling through extra orbitals and hybridizations, which causes changes to the electronic structure important for tuning functional properties.

Co-doping with Te and Zr considerably changes the electronic structure of $MgTiO_3$. The bottom of the valence band of (Te, Zr) co-doped $MgTiO_3$ lies in the range −5.5 to −4.5 eV and is dominated by the Te-p contribution. However, the VBM of (Te, Zr) co-doped $MgTiO_3$ is dominated by the O-p contribution with minor contributions from Mg, Ti, Zr, and Te s orbitals. A large hybridization of Te-p states with O-p states is displayed, which improves the mobility of carrier electrons and improves optical absorption. The CB is dominated by Ti-d orbitals, showing that the role of Ti in the electronic transitions in $MgTiO_3$ is important. The co-doping shifts the Fermi level towards the VBM and induces p-type SC characteristics due to the charge compensation effects of Zr and Te substitution. The Te-p states are situated at the VBM, and the Zr-d states are near the CBM, and this makes the band gap smaller as the VBM is elevated and the CBM is pushed down. The band gap narrowing was confirmed by the TDOS and PDOS, which shows that the defects generated by the presence of dopants narrowed the energy band gap between the VB and CB edges. These changes in the electronic structure indicate the suitability of (Te, Zr)-co-doped $MgTiO_3$ for optoelectronic applications.

Table 1. Calculated Eg of pristine and Zr/Te co-doped $MgTiO_3$ obtained using the TB-mBJ functional.

Materials	**Eg (eV)**
$\mathbf{MgTiO_3}$	2.93
$\mathbf{Mg_8Ti_7Zr_1O_{23}Te_1}$	1.15
$\mathbf{Mg_8Ti_7Zr_1O_{22}Te_2}$	0.64

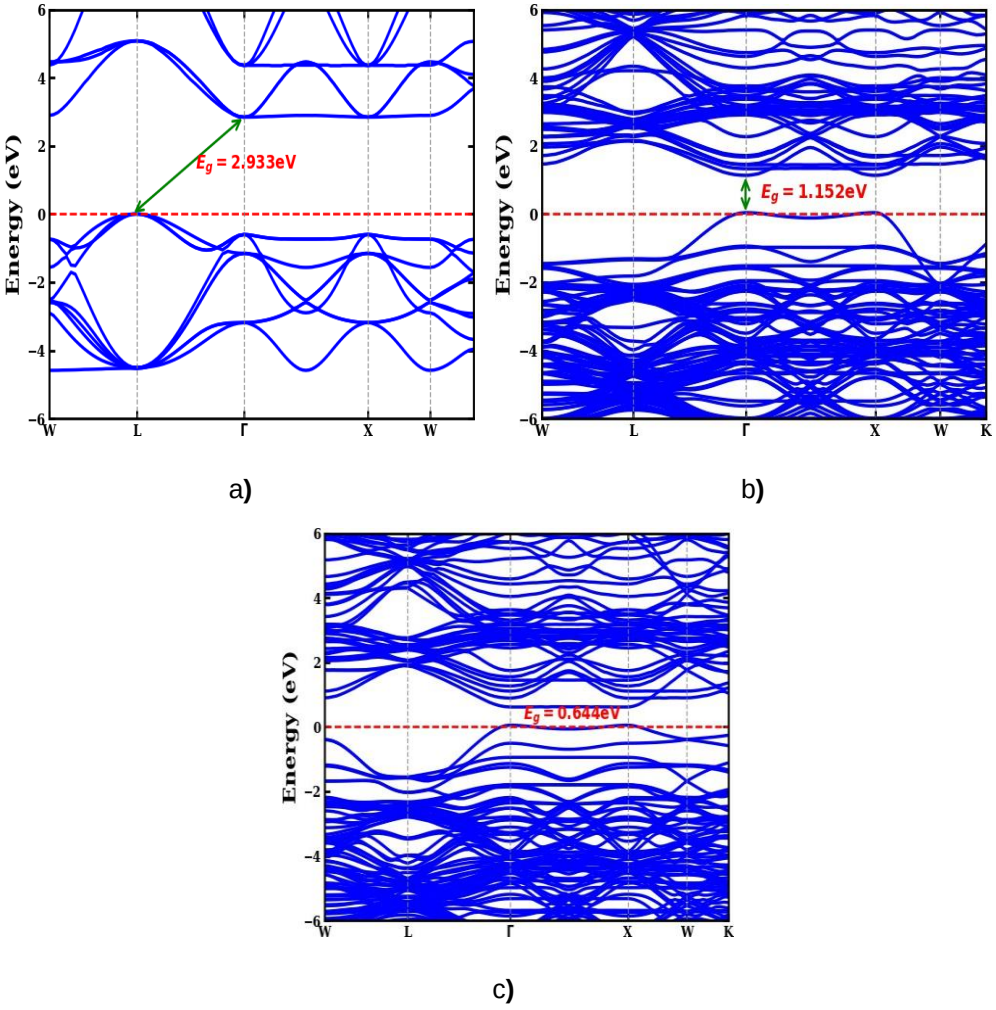

Figure 3: Electronic band structures of (a) pristine $MgTiO_3$, (b) (Zr, Te) co-doped $MgTiO_3$ with one Te atom, and (c) (Zr, Te) co-doped $MgTiO_3$ with two Te elements.

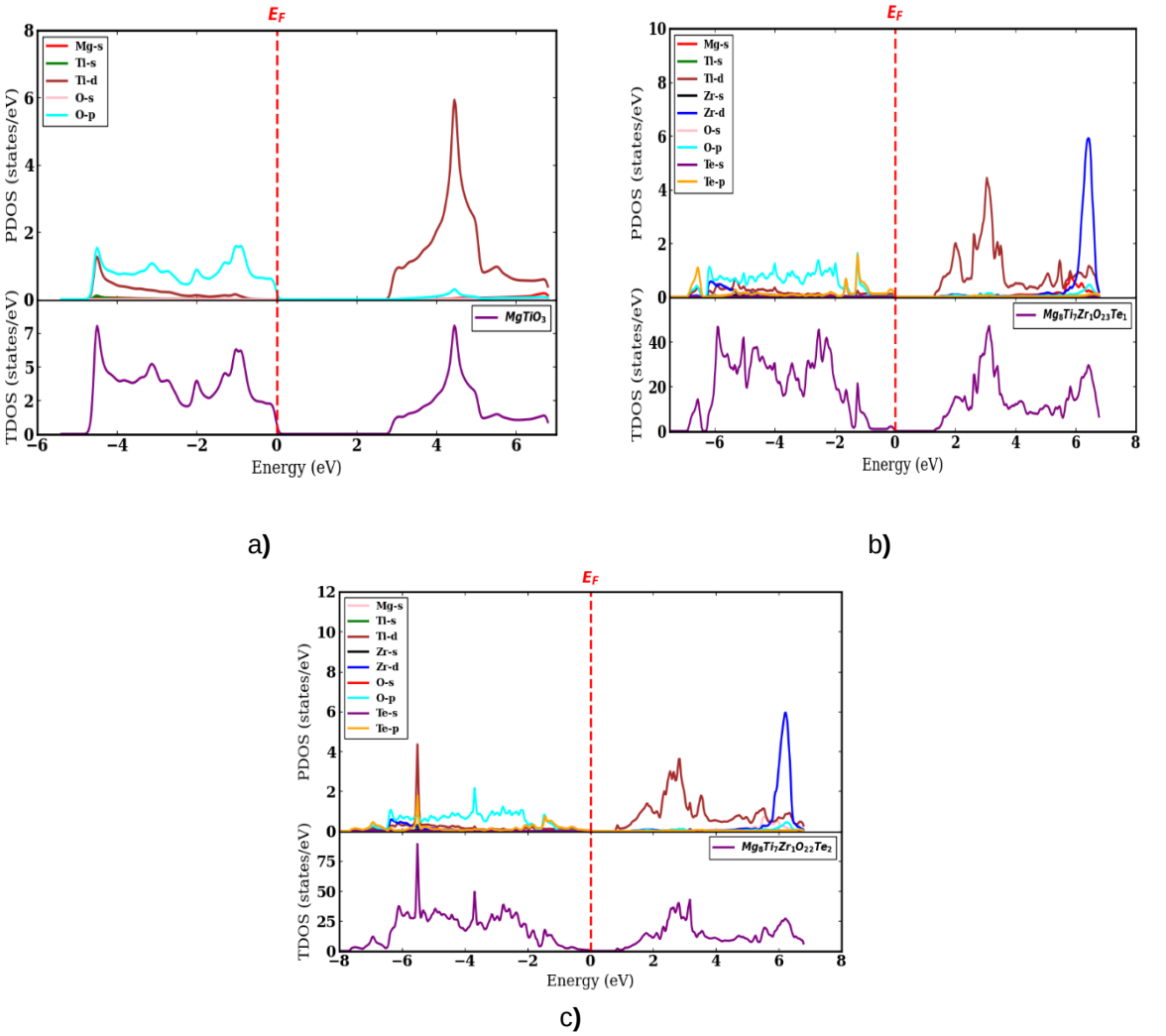

Figure 4: TDOS and PDOS of (a) pristine $MgTiO_3$, (b) (Zr, Te) co-doped $MgTiO_3$ with one Te atom, and (c) (Zr, Te) co-doped $MgTiO_3$ with two Te elements.

3.3. Optical properties:

The optical properties of pristine and (Zr, Te) co-doped $MgTiO_3$ were systematically investigated by analyzing the frequency-dependent complex DF $\varepsilon(\omega) = \varepsilon_1(\omega) + i\varepsilon_2(\omega)$, the optical absorption coefficient $\alpha(\omega)$, and the optical conductivity $\sigma(\omega)$. These quantities are crucial for understanding the interaction of electromagnetic radiation with matter and for assessing the potential of materials in optoelectronic applications.

The $\varepsilon_1(\omega)$ of the DF is presented in Figure 5(a). $\varepsilon_1(\omega)$ has a moderate value of the static dielectric constant $\varepsilon_1(0)$ in the case of pristine $MgTiO_3$ materials, which is a typical feature of wide band gap semiconductor oxides. When the materials are co-doped with (Zr, Te), a remarkable increase in the value of $\varepsilon_1(0)$ is found, especially in the direction

along the crystal axis zz. The $\varepsilon_2(\omega)$ of the DF for the given compound is presented in Figure 5(b) and represents the inter-band optical transitions. It should be noted that for the pristine compound of $MgTiO_3$, the onset of absorption is located in the ultraviolet region with an energy higher than 3.5 eV, as expected for such compounds with large band gaps. On the contrary, for the co-doped compounds with Zr and Te, the red shift of the onset of absorption to the range of visible light with an energy between 1.5 and 2.0 eV is observed due to optical transitions involving Te-p states near the VB and the Zr-d/Ti-d states near the CB. The $\alpha(\omega)$, as indicated in Figure 5(c), again verifies the aforementioned phenomenon. While pristine $MgTiO_3$ absorbs UV light and is nearly transparent in the visible spectrum, co-doping increases visible light absorption.

Figure 5(d) presents the $\sigma(\omega)$. For pristine $MgTiO_3$, $\sigma(\omega)$ remains nearly zero below 3 eV, indicating weak photon-induced charge transport. In contrast, the co-doped systems exhibit finite $\sigma(\omega)$ at lower photon energies, reflecting enhanced photogenerated charge carrier activity. The appearance of prominent conductivity peaks at reduced energies suggests that dopant-induced electronic states facilitate more efficient optical transitions.
Overall, the (Zr, Te) co-doping strategy significantly modifies the optical response of $MgTiO_3$, transforming it from a UV-active wide-bandgap into a visible-light-sensitive. The enhanced dielectric response, extended absorption range, and increased $\sigma(\omega)$ highlight (Zr, Te)-co-doped $MgTiO_3$ as a promising candidate for advanced technological applications.

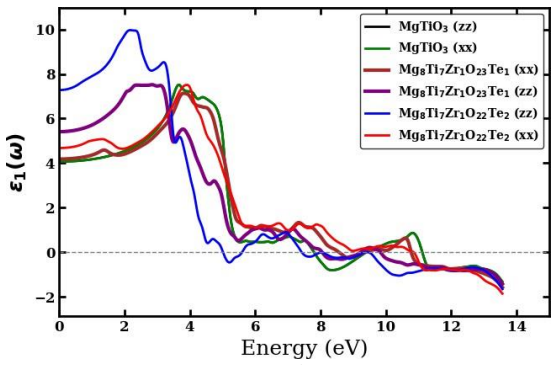

a)

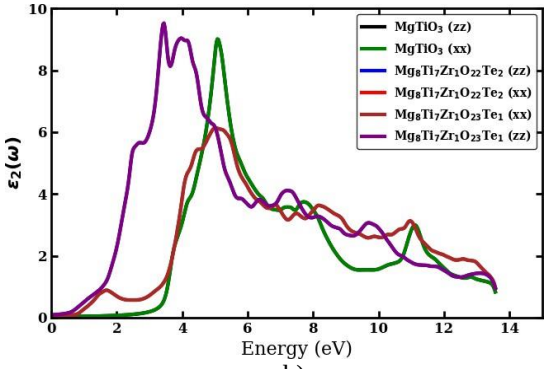

b)

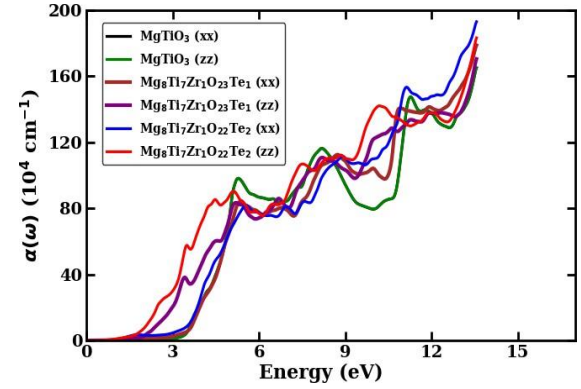

c)

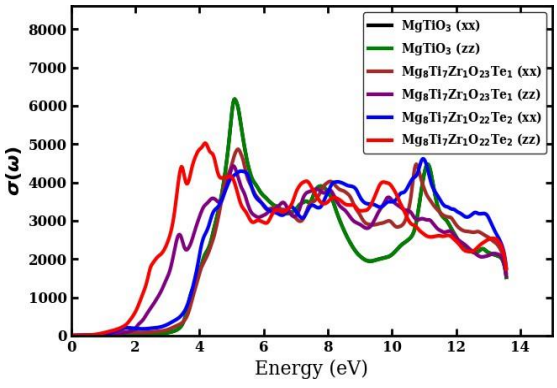

d)

Figure 5: Optical properties of pristine and (Zr, Te) co-doped $MgTiO_3$: (a) real and (b) imaginary parts of the DF, (c) optical absorption coefficient, and (d) optical conductivity as a function of photon energy.

4. Conclusion:

A first-principles study using DFT investigated the optoelectronic properties of pristine and (Zr, Te) co-doped $MgTiO_3$. Electronic structure analysis reveals that pure $MgTiO_3$ is a wide band gap material with limited visible light utilization. However, Zr/Te co-doping introduces impurity states near the VBM and CBM, narrowing the band gap and shifting optical activity from the ultraviolet to the visible range. Improved static dielectric constant, absorption edge, visible light absorption, and low-photon-energy optical conductivity in the co-doped material support these findings. These improvements arise from the hybridization of Te-p and Zr-d states with the host lattice, facilitating interband transitions and charge carrier excitation. In addition, (Zr, Te) co-doping effectively tunes the electronic and optical properties of $MgTiO_3$, enhancing its optical response and electronic transport, making it a promising candidate for advanced technological and optoelectronic applications. This theoretical work provides valuable guidance for experimental synthesis and devices. Although the present study is based on first-principles calculations, the predicted trends can be experimentally validated using well-established characterization techniques. Structural properties may be examined using X-ray diffraction (XRD), while the band gap and optical absorption can be measured using UV–Vis spectroscopy. In addition, photoluminescence spectroscopy can provide insights into recombination mechanisms and electronic transitions. Importantly, previous experimental studies on doped titanate perovskites have reported band gap narrowing and enhanced visible-light absorption upon doping, which are consistent with our theoretical predictions. Therefore, the present results provide reliable guidance for future experimental synthesis and characterization of Zr/Te co-doped $MgTiO_3$ for optoelectronic and energy-related applications.

Funding: The authors are warmly grateful to the support of "The Moroccan Association of Sciences and Techniques for Sustainable Development (MASTSD), Beni Mellal, Morocco"

References

[1] S. Nazir, I. Mahmood, N.A. Noor, A. Laref, M. Sajjad, Ab-initio simulations of MgTiO3 oxide at different pressure. High Energy Density Phys. 33, 100715 (2019). https://doi.org/10.1016/j.hedp.2019.100715

[2] F. Opoku, K.K. Govender, C.G.C.E. van Sittert, P.P. Govender, Recent progress in the development of semiconductor-based photocatalyst materials for applications in photocatalytic water splitting and degradation of pollutants. Adv. Sustain. Syst. 1, 1700006 (2017). https://doi.org/10.1002/adsu.201700006

[3] A. Cesana, E. Mauro, M. Silari, Induced radioactivity in a patient-specific collimator used in proton therapy. Nucl. Instrum. Methods Phys. Res. B 268, 2272–2280 (2010). https://doi.org/10.1016/j.nimb.2010.03.004

[4] S.E. Hosseini, M.A. Wahid, Hydrogen production from renewable and sustainable energy resources: Promising green energy carrier for clean development. Renew. Sustain. Energy Rev. 57, 850–866 (2016). https://doi.org/10.1016/j.rser.2015.12.112

[5] L. Azzouz, M. Halit, M. Rérat, R. Khenata, A.K. Singh, M.M. Obeid, X. Wang, Structural, electronic and optical properties of ABTe2 (A = Li, Na, K, Rb, Cs and B = Sc, Y, La): Insights from first-principles computations. J. Solid State Chem. 279, 120954 (2019). https://doi.org/10.1016/j.jssc.2019.120954

[6] A. Bouzaid, Y. Ziat, H. Belkhanchi, Photocatalytic optimization of $ATiO_3$ codoped with Se/Zr: A DFT study for hydrogen production. Materials 18, 4389 (2025). https://doi.org/10.3390/ma18184389

[7] Y. Ding, W. Que, J. He, W. Bai, P. Zheng, P. Li, J. Zhai, Realizing high-performance capacitive energy storage in lead-free relaxor ferroelectrics via synergistic effect design. J. Eur. Ceram. Soc. 42, 129–139 (2022). https://doi.org/10.1016/j.jeurceramsoc.2021.09.051

[8] Z. Li, L. Liu, B. Xu et al., High-contrast gratings based spoof surface plasmons. Sci. Rep. 6, 21199 (2016). https://doi.org/10.1038/srep21199

[9] T. Santhosh Kumar, P. Gogoi, A. Perumal, P. Sharma, D. Pamu, Effect of cobalt doping on the structural, microstructure and microwave dielectric properties of MgTiO3 ceramics prepared by semi-alkoxide precursor method. J. Am. Ceram. Soc. 97, 1054–1059 (2014). https://doi.org/10.1111/jace.12851

[10] A. Bouzaid, Y. Ziat, H. Belkhanchi, Ab initio design of Zr/Te co-doped $XTiO_3$ (X = Ca, Sr) perovskites for enhanced solar-driven hydrogen evolution and optoelectronic energy conversion. Next Mater. 11, 101666 (2026). https://doi.org/10.1016/j.nxmate.2026.101666

[11] K. Momma, F. Izumi, VESTA3 for three-dimensional visualization of crystal, volumetric and morphology data. J. Appl. Crystallogr. 44, 1272–1276 (2011). https://doi.org/10.1107/S0021889811038970

[12] F.D. Murnaghan, The compressibility of media under extreme pressures. Proc. Natl. Acad. Sci. USA 30, 244–247 (1944). https://doi.org/10.1073/pnas.30.9.244

[13] A.A. Adewale, A. Chik, T. Adam, O.K. Yusuff, S.A. Ayinde, Y.K. Sanusi, First principles calculations of structural, electronic, mechanical and thermoelectric properties of cubic ATiO3 (A = Be, Mg, Ca, Sr and Ba) perovskite oxide. Comput. Condens. Matter 28, e00562 (2021). https://doi.org/10.1016/j.cocom.2021.e00562

Methylammonium lead halide perovskites: Electronic structure and optical properties for tandem solar cells

Fatima Oubihi[1], *El Hassan* El Harouny[1*], *Hanan* Ziani[1], *Jamal* El Khamkhami[1], *El Mahdi* Assaid[2,3], *Ahmed* Lachgar[1], *and Abdelfattah* Achahbar[1]

[1] Artificial Intelligence and Computational Physics Laboratory, Department of Physics, Faculty of Sciences, Abdelmalek Essaadi University, 93030 Tetouan, Morocco
[2] Electronics and Optics of Semiconductor Nanostructures and Sustainable Energy Team, Department of Physics, Faculty of Sciences, Chouaïb Doukkali University, 24000 El Jadida, Morocco
[3] Laboratory of Instrumentation of Measure and Control, Département de Physique, Faculty of Sciences, Chouaïb Doukkali University, 24000 El Jadida, Morocco

Abstract. Solar cells based on tandem structures enable improved utilization of the solar spectrum and higher power conversion efficiencies. In this context, Methylammonium lead halide perovskites remain strong candidates for forming stacked configurations on silicon substrates. These perovskites, hereafter referred to as MALH, have the chemical formula $CH_3NH_3PbX_3$, where X denotes a halide ion such as Bromine, Iodine or Chlorine. They are highly effective at converting sunlight into electrical energy due to their strong light absorption properties. In this work, a systematic comparative study of the three halide compositions (X = I, Br and Cl) in orthorhombic phase is carried out, in order to clarify the effect of halide substitution on the electronic structure and optical properties of these materials. Their structural, electronic and optical properties are theoretically investigated using first principles density functional theory (DFT) calculations. Analysis of the calculated density of states (DOS) and band structure confirms the direct band-gap nature of the perovskites, tunable around 1.64 eV for X=I, 2.43 eV for X=Br, and 2.50 eV for X=Cl. These results align well with previously reported experimental and theoretical finding, confirming the potential of these materials for future generation photovoltaics.

* Corresponding author: e.elharouny@uae.ac.ma

1. Introduction

One of the most pressing challenges of modern times is the search for suitable materials for efficient energy production and storage. Among renewable energy sources, solar energy represents a crucial resource due to its global availability and minimal environmental impact. For several decades, silicon based photovoltaic technologies have dominated the solar energy market, currently accounting for nearly 95% of global photovoltaic deployment. This dominance is largely attributed to their high module efficiency, the abundance of nontoxic raw materials, and their long term operational reliability. However, the maximum theoretical efficiency limit of a single junction silicon photovoltaic cell is approximately 25% [1]. In practice, this value is lower due to inevitable energy losses that occur during the fabrication and operation of photovoltaic cells. These limitations primarily arise from the intrinsic material properties of silicon. In particular, its band gap (~1.12eV) allows only photons with energies above a certain threshold to be converted into electrical energy, while photons with excess energy cannot be fully utilized by the solar cell. To overcome these limitations and enhance device performance, significant research efforts in recent years have focused on the development of advanced photovoltaic architectures, yielding promising results. Among these approaches, tandem solar cells composed of two or more stacked photovoltaic layers have emerged as one of the most effective strategies for improving the overall efficiency of photovoltaic modules by enabling more efficient utilization of the solar spectrum [2]. Due to their outstanding optoelectronic properties, lead halide perovskites have emerged as highly efficient absorber materials for photovoltaic devices. These semiconductors exhibit several remarkable characteristics, including high optical absorption coefficients, tunable band gaps, long charge carrier diffusion lengths, high carrier mobility, and impressive power conversion efficiencies (PCE). Owing to these advantageous properties, lead halide perovskites have attracted considerable attention for a wide range of photovoltaic and optoelectronic applications [3]. Hybrid perovskites generally follow the chemical formula ABX_3. In this structure, the A site is typically occupied by organic cations such as methylammonium (MA) or formamidinium (FA), while the B site contains divalent metal cations, including Pb, Sn, or Ge. The X site is occupied by halide anions such as I^-, Br^-, or Cl^-. In the perovskite lattice, the B and X ions form a network of corner sharing BX_6 octahedra, where the B cation is located at the center of the octahedron and the X anions occupy the vertices. The A cation resides within the cavities formed by the three dimensional octahedral framework [4]. Perovskite solar cells have shown excellent light absorption, charge-carrier mobilities, and lifetimes, possess low cost, ease of fabrication, such as a power conversion efficiency of 3.8% since their first demonstration, performance has rapidly improved, reaching a certified efficiency of 22.1% within just a few years. However, what distinguishes $CH_3NH_3PbX_3$ (X = I, Br, Cl) from many other materials and makes it an attractive alternative to silicon is its low cost, solution based synthesis and relatively simple processing methods. Since its introduction as a photovoltaic absorber, extensive research efforts have been devoted to device fabrication, efficiency optimization, and the development of scalable architectures suitable for industrial applications. These characteristics make metal halide perovskites particularly promising candidates for use in double junction tandem solar cells. In this work, we present a systematic ab initio calculations of electronic structure and optical properties of orthorhombic $CH_3NH_3PbX_3$ (X = I, Br, Cl) phases. Although several theoretical studies have explored the cubic or tetragonal phases of these hybrid halide perovskites, comprehensive and consistent investigations of all three halide compositions within the same orthorhombic phase remain limited, particularly for the chloride compound [5]. This study addresses this limitation by providing a complete comparative analysis of the structural, electronic, and optical properties of the three compositions within a unified

orthorhombic phase. The novelty of this work lies in three main aspects. First, a systematic investigation of the three halide substitutions (I, Br, and Cl) in the orthorhombic phase is carried out, providing a clear understanding of the correlation between halide composition, electronic structure, and optical response. Second, an in-depth analysis of the relationship between Pb–X orbital hybridization at the band edges and the resulting optical properties is presented, including the anisotropic optical response characteristic of the orthorhombic crystal structure. Third, the tunability of the band gap across the visible spectrum is demonstrated, with calculated values of 1.64 eV (I), 2.43 eV (Br), and 2.50 eV (Cl), highlighting the potential of these materials for integration into tandem solar cells and other optoelectronic devices. Furthermore, our results show good agreement with available experimental and theoretical studies, validating the reliability of our computational approach [6,7]. By elucidating the role of halide substitution and structural anisotropy, this work provides new insights into the design of lead halide perovskites for high-efficiency photovoltaic technologies.

2. Computational methods

In all ab initio methods used to describe an N-electron system, the primary goal is to approximate the exact wave function, which contains all the accessible information about the system. However, such calculations can be extremely demanding in terms of computational time and memory, particularly for larger systems. Therefore, it is reasonable to develop alternative approaches to this problem, even if this means some level of detail must be sacrificed. In this work, we investigate the structural and electronic properties of $CH_3NH_3PbX_3$ compounds (X = Br, I, and Cl) using the Density Functional Theory (DFT) method. To describe the exchange-correlation effects, the Perdew-Burke-Ernzerhof (PBE) generalized gradient approximation (GGA) was utilized. The Projector Augmented Wave (PAW) method was employed to treat the interactions between ions and valence electrons. In order to obtain more reliable electronic properties, the HSE hybrid functional was also used for accurate the electronic band structure calculations. The Calculations were performed utilizing the QUANTUM ESPRESSO package [8]. A plane wave kinetic energy cutoff of 600 eV was employed, and Brillouin zone integration was performed using an unshifted 12 × 12 × 12 k-point grid, based on the Monkhorst Pack scheme. Self-consistent field (SCF) calculations were converged to a total energy threshold of 10^{-8} Ry. Electronic band structures were determined along the high symmetry path Γ-X-S-Y-Γ-Z-U-R-Z. Lattice parameters, bond lengths, density of states (DOS), and optical absorption spectra were computed within the same framework. Graphical representation of all the results were generated using the XMGRACE package.

3. Results and discussion

3.1 Structural properties

The crystallographic structures of different hybrid perovskite are among the most studied fundamental aspects so far, especially since they are subject to radical changes as a function of temperature. Studies exploiting the temperature dependent variations in the behavior of $CH_3NH_3PbX_3$ (X= I, Br, Cl) have led to a classification of the crystal structures of this perovskite according to the temperature region. At high temperature, the $CH_3NH_3PbX_3$ perovskites (X=Cl :T>179K, X=Br :T>236K, X=I:T>330K) crystallize in a cubic phase with symmetry group (Pm3m) [9]. Upon cooling, these materials undergo a phase transition

from the cubic to a tetragonal structure, typically described by the space group I4/mcm. This structural transition is primarily driven by the tilting of the PbX_6 octahedra within the perovskite lattice, rather than by ferroelectric displacement of the Pb^{2+} cation. The tetragonal phase is characterized by a unit cell that is larger than that of the cubic phase due to these octahedral distortions [10]. Upon further decreasing the temperature, a second phase transition from the tetragonal to orthorhombic symmetry occurs (X=Cl: T<173K, X=Br: T<149K, X=I: T<161K), leading to a reduction in the orientational disorder of the CH_3NH_3 cations. In this investigation, $CH_3NH_3PbX_3$ compounds are considered in their orthorhombic perovskite structure. At low temperatures, they crystallize in the *Pnma* space group. This orthorhombic phase, wish ensures structural stability, is characterized by 48 atoms in unit cell.

Figure 1 depicts the atomic unit cell of the low temperature orthorhombic phase. Each structure incorporates four $CH_3NH_3^+$. Each Pb atom is octahedrally coordinated by six halide anions (Br^-, I^-, or Cl^-). The dipolar organic methylammonium cations ($CH_3NH_3^+$) are accommodated within the cavities formed by the PbX_6 (X = I, Br, Cl) octahedral framework. The bond lengths between the constituent atoms are provided in Table1, The $CH_3NH_3PbX_3$ compounds form orthorhombic perovskite structures with Pnma symmetry with the received crystal constants listed in Table 2.

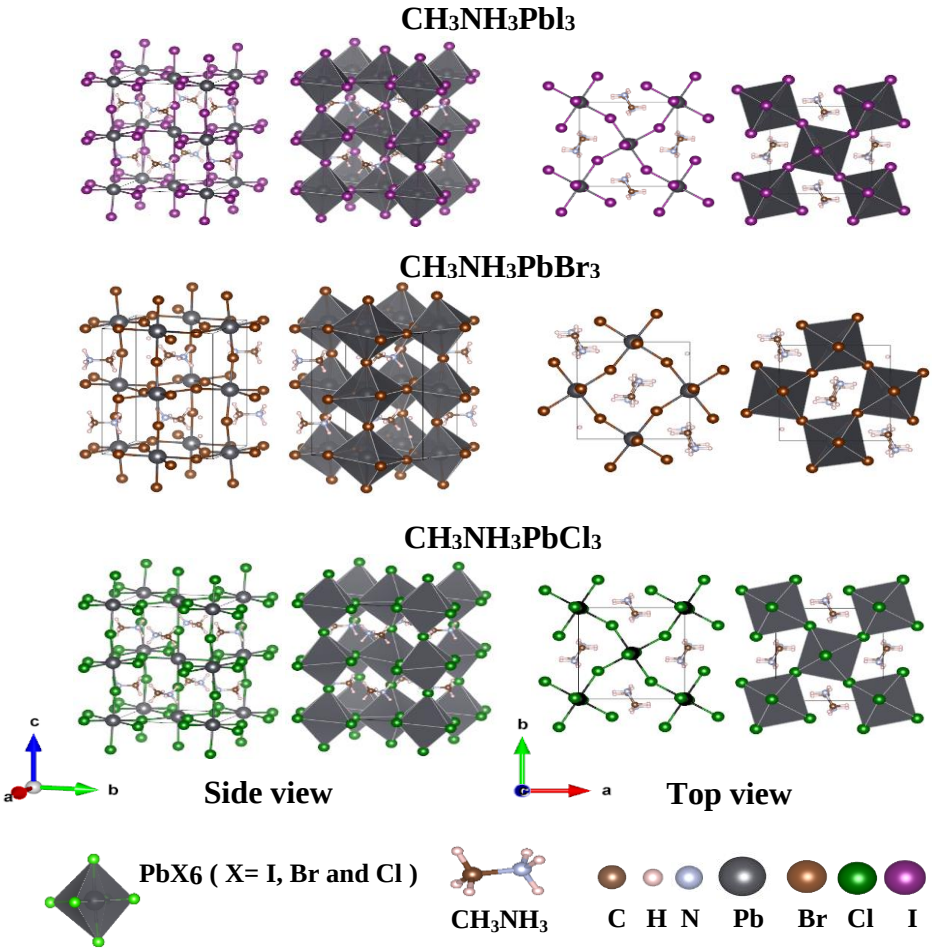

Fig. 1. The Side and top views showing the chemical bonds within the CH_3NH_3 molecule and the PbI_6, $PbBr_6$, and $PbCl_6$ octahedral groups associated with $CH_3NH_3PbI_3$, $CH_3NH_3PbBr_3$, and $CH_3NH_3PbCl_3$, respectively

Table 1. Bond lengths between the constituent atoms of $CH_3NH_3PbI_3$, $CH_3NH_3PbBr_3$, and $CH_3NH_3PbCl_3$

$CH_3NH_3PbX_3$	d_{Pb-X} (Å)	d_{C-N} (Å)	d_{C-H} (Å)	d_{N-H} (Å)
$CH_3NH_3PbI_3$	$3.17 - 3.19_{(Pb-I)}$	[1.50 - 1.61]	[1.01 - 1.12]	[1.70 -1.18]
$CH_3NH_3PbBr_3$	$3.31 - 3.31_{(Pb-Br)}$	[1.50 - 1.61]	[1.01 - 1.12]	[1.70 -1.18]
$CH_3NH_3PbCl_3$	$2.38 - 2.68_{(Pb-Cl)}$	[1.50 - 1.61]	[1.01 - 1.12]	[1.70 - 1.18]

3.2 Electronic properties

In 2004, Y. H. Chang and C. H. Park investigated the electronic properties of the hybrid inorganic–organic lead halide perovskites $CH_3NH_3PbX_3$ (X = I, Br, and Cl) using first-principles pseudopotential calculations. Their study revealed that the electronic states associated with the organic molecule are located deep within the valence and conduction bands, whereas the band-edge states primarily originate from the Pb–X bonding interactions. Based on these findings, the authors concluded that the organic cation has a negligible influence on the optoelectronic properties of the material. On the other hand, in 2008, I. Borriello, G. Cantele, and D. Ninno demonstrated that the electronic properties of hybrid perovskites, particularly the band gap, can be tuned through an appropriate choice of the organic cation, especially its size. In their study, based on ab initio calculations, the electronic structures of the orthorhombic phases of $CH_3NH_3PbX_3$ were investigated using the PBE exchange correlation functional. By analyzing the band structure and density of states, the authors highlighted the influence of structural parameters on the electronic properties of these materials. The calculated band structures of $CH_3NH_3PbX_3$ (X = I, Br, and Cl) are presented in Figure 2 In the band structure plots, the highest occupied and lowest unoccupied bands are highlighted in red and blue, respectively, for each compound. All investigated structures exhibit a direct band gap located at the Γ-point of the Brillouin zone. The calculated band gap energies are 1.64 eV, 2.43 eV, and 2.50 eV for $CH_3NH_3PbI_3$, $CH_3NH_3PbBr_3$, and $CH_3NH_3PbCl_3$, respectively.

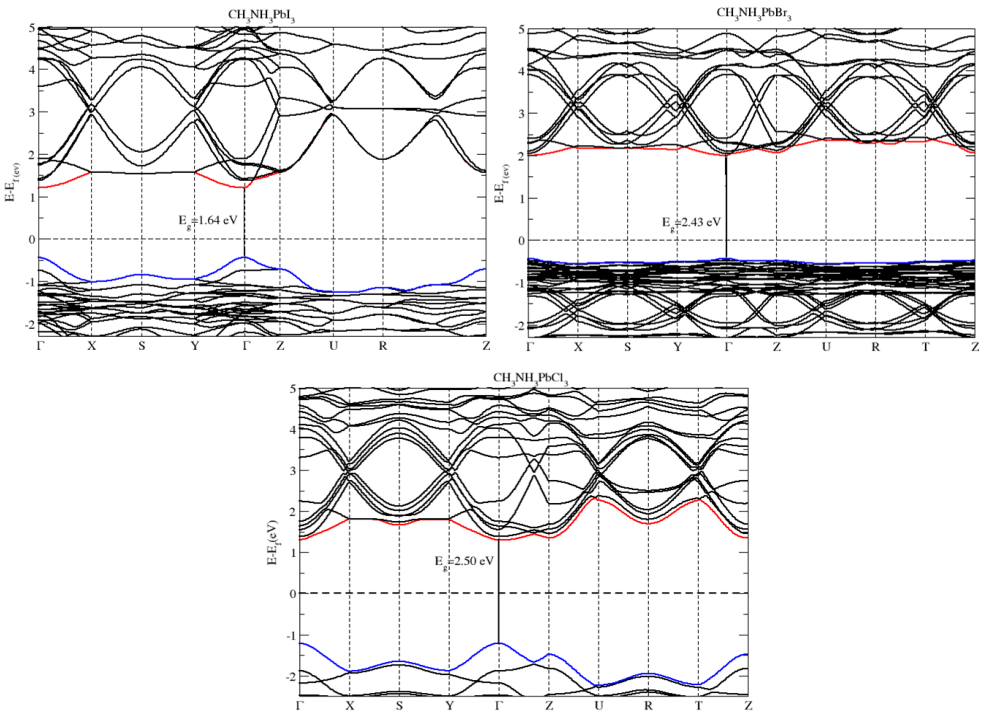

Fig. 2. Band structures of $CH_3NH_3PbI_3$, $CH_3NH_3PbBr_3$, $CH_3NH_3PbCl_3$ calculated using density functional theory along high symmetry points of Bz. The band gap is highlighted for three structure, with the maximum occupied and minimum unoccupied bands shown in red and blue, respectively.

The band gap energies calculated for the $CH_3NH_3PbCX_3$ (X=I, Br, Cl) are further supported by the analysis of the partial density of state (PDOS). The valence band maximum is significantly influenced by the p orbital of I, Br and Cl for $CH_3NH_3PbI_3$, $CH_3NH_3PbBr_3$, $CH_3NH_3PbCl_3$ respectively with a minor contribution from the Pb and CH_3NH_3, conversely, the conduction band minimum is primarily due to the Pb and CH_3NH_3 as illustrated in Figure 3.

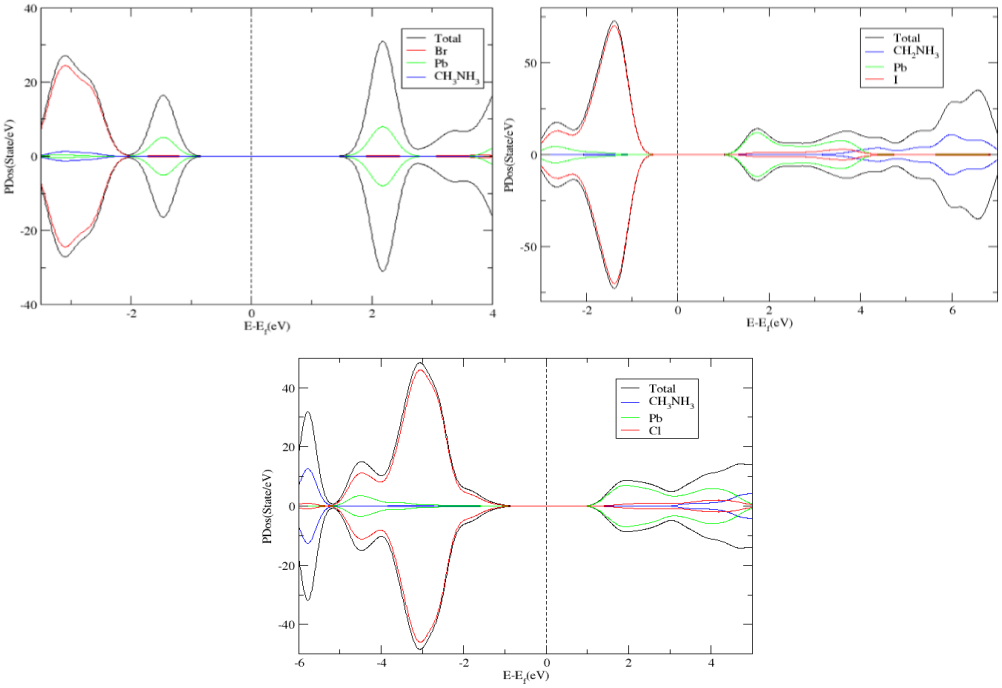

Fig. 3. The computed densities of states of $CH_3NH_3PbI_3$, $CH_3NH_3PbBr_3$ and $CH_3NH_3PbCl_3$ structures

Table 2. Lattice constant (Å), E_t, E_f and E_g calculated using (PBE and HSE) of $CH_3NH_3PbX_3$ (X=I, Br, Cl)

Compounds	**a (Å)**	**b (Å)**	**c (Å)**	**E_{gPBE} (eV)**	**E_{gHSE}(eV)**	**E_t (Ry)**	**E_f(eV)**
$CH_3NH_3PbBr_3$	8.06	8.77	12.08	2.43	2.75	-9108.93	2.40
$CH_3NH_3PbI_3$	8.55	9.25	12.96	1.64	2.13	-8245.22	4.20
$CH_3NH_3PbCl_3$	8.21	8.21	12.34	2.50	3.52 [11]	-4650.98	2.71

The effective mass is a fundamental parameter for describing the electronic properties of photovoltaic materials, as it directly influences charge-carrier mobility and electronic transport [12]. A comprehensive understanding of these transport properties in the studied heterostructures and their impact on photovoltaic efficiency is therefore essential. In this context, the analysis of the average effective masses of electrons and holes becomes particularly important. It's well known that a lower effective masse generally leads to higher carrier mobility and conversely, a higher effective mass results in reduced mobility, which in turn can increase the solar cells efficiency by enhancing charge transport and minimizing recombination losses. The effective mass can differ based on the particular

perovskite halide material and its specific composition. This is influenced by the material's band structure, the changes in the valence band and conduction band edges at the band edge, which is determined by the types of halides and other elements in the perovskite. The effective mass of electrons and holes were determined by fitting the parabolic functions to the conduction band minimum and valence band maximum, respectively, along the x, y and z directions, using the following approach:

$$\frac{1}{m^*_{i,j}} = \frac{1}{\hbar^2}\frac{\partial^2 E_n(k)}{\partial k_i \partial k_j} \quad (1)$$

Table 3 summarizes the effective masses of holes (h) and electrons (e) along the x, y and z axes, as well as the calculated average effective mass $m^*_{d\_e/h} = (m^*_{xx} m^*_{yy} m^*_{zz})^{1/3}$ for $CH_3NH_3PbX_3$, X (I, Br and Cl). Clearly, we can see the anisotropies in effective charge masses along three principal directions and It's observed that the effective mass of conduction electrons is relatively small, whereas the holes exhibit a significantly larger effective mass. This suggests that the mobility of electrons is more easily and higher than holes in the material. This disparity influences the carrier transport properties, affecting how efficiently charges are extracted and generate an electric current when an electric field is applied. The Variations in the effective masses affect recombination rates. when electron effective mass is lower, electrons are less likely to recombine with holes, which enhances charge separation and increases the likelihood of charge collection at the contacts, thereby improving the production of electrical energy.

Table 3. Effective mass of electrons and holes for $CH_3NH_3PbX_3$ (X = I, Br, Cl)

		$CH_3NH_3PbBr_3$	**$CH_3NH_3PbI_3$**	**$CH_3NH_3PbCl_3$**
m_e*	m^*_{e-x}	0.18	0.14	0.10
	m^*_{e-y}	0.16	0.13	0.10
	m^*_{e-z}	0.17	0.13	0.25
	m^*_{d-e}	0.17*	0.13*	0.14*
m_h*	m^*_{h-x}	-1.08	-0.29	-0.12
	m^*_{h-y}	-0.84	-0.23	-0.13
	m^*_{h-z}	0.95	0.26	0.13
	m^*_{d-h}	0.95*	0.26*	0.13*

3.3 Optical properties

A comprehensive analysis of The optical behaviors of the material of perovskite compounds $CH_3NH_3PbX_3$ (X =I, Br, Cl) is crucial for gaining insight into their fundamental characteristics and for evaluating their potential in various applications . Accordingly, an in depth analysis of their optical response has been conducted. The complex dielectric function, ε(ω), Is represented by the following equation [13]:

$$\varepsilon(\omega) = \varepsilon_1(\omega) + \varepsilon_2(\omega) \quad (2)$$

ε(ω) comprises two components : Imaginary part, which is associated with the absorption (loss or gain) of the material and can be theoretically obtained from the computation of momentum matrix elements between occupied and unoccupied electronic states, as presented below [13]:

$$\varepsilon_2 = \frac{e^2\hbar}{\pi m^2\omega^2}\sum_{v,c}\int_{BZ}^{\cdot}[\langle ck|e\nabla|vk\rangle]^2\delta\{\omega_{ck}(k)-\omega\}d^3k \quad (3)$$

Real part $\varepsilon_1(\omega)$, arises from various displacement polarization mechanisms within the material and represents the energy storage component. It is obtained from $\varepsilon_2(\omega)$, through the Kramers-Kronig relations [13]:

$$\varepsilon_1 = 1 + \frac{2}{\pi}\int_0^{\infty}\frac{\varepsilon_2(\omega')}{\omega'^2-\omega^2}\omega'\,d\omega' \quad (4)$$

Additional optical constants may be determined from the dielectric function. Such as the absorption coefficient α(ω) and the energy loss function ELF, L(ω). These parameters are subsequently obtained from.

α(ω) and the L(ω) were determined using the equations Presented below [14]:

$$\alpha(\omega) = \frac{\sqrt{2}\omega}{c}\{[\varepsilon_1^2(\omega)+\varepsilon_1^2(\omega)]^{\frac{1}{2}}-\varepsilon_1(\omega)\}^{\frac{1}{2}} \quad (5)$$

$$L(\omega) = \frac{\varepsilon_2}{\varepsilon_1^2+\varepsilon_2^2} \quad (6)$$

$\varepsilon_1(\omega)$ and $\varepsilon_2(\omega)$ parts of the dielectric function along different directions x,y and z for $CH_3NH_3PbX_3$ (X= I, Br and Cl) are presented in Figure 4 ((a), (c), (e)) and 4 ((b), (d), (f)) respectively.

We considered the both parts of the dielectric functions real and imaginary to compare the presence/absence of isotropy effects under various directions, as illustrated in Figure 4. Our analysis indicates that the $CH_3NH_3PbI_3$, $CH_3NH_3PbBr_3$ and $CH_3NH_3PbCl_3$ perovskite structures exhibit anisotropy along the xx, yy and zz directions. Figure 4(a) reveals a peak at about 2 eV for $CH_3NH_3PbI_3$, in Figure 4(c) at 2.5 eV for $CH_3NH_3PbBr_3$ and in Figure 4(e) at 3 eV for $CH_3NH_3PbCl_3$, suggesting notable electronic transitions occurring at the corresponding energies. These peaks, corresponding to interband transitions, demonstrate that electrons are excited from the valence band to the conduction band, in accordance with theoretical calculations. Regarding Figure 4 (b, d, f), which indicates the imaginary part ε_2 (ω), exhibits a prominent peak in the [2 – 4 eV] region for three compounds. But, $CH_3NH_3PbI_3$ shows a slightly higher absorption in the energy region between 5 eV and 10 eV, the place is occupied by the $CH_3NH_3PbBr_3$ then comes after $CH_3NH_3PbCl_3$. This suggests that $CH_3NH_3PbI_3$ may absorb more light in this region. enhancing its potential for photovoltaic applications. The observed peaks are likely the result of electronic transitions between the valence and the conduction bands.

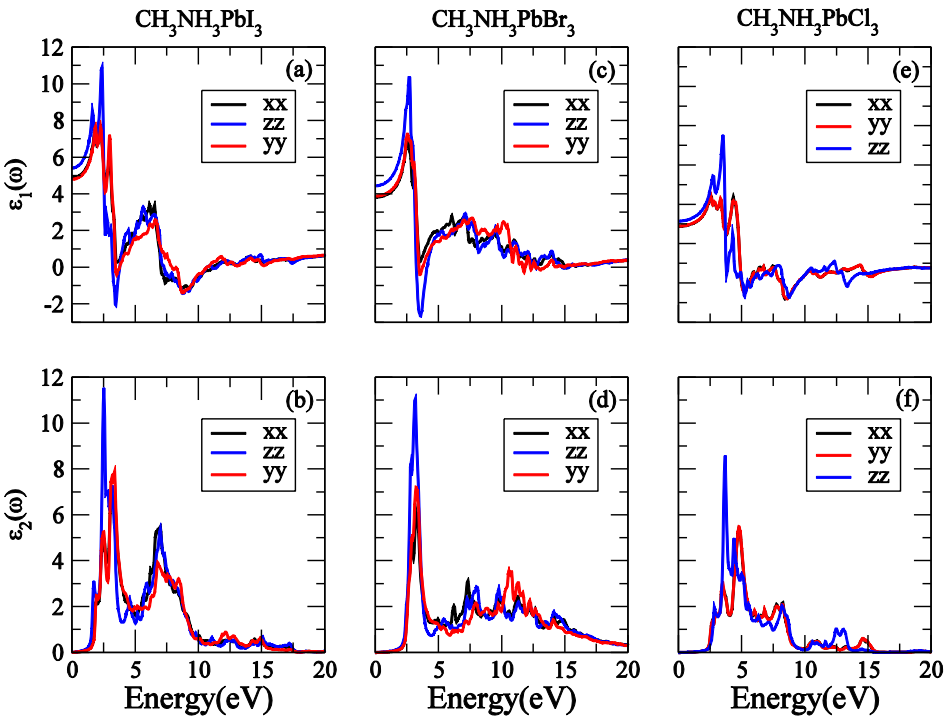

Fig. 4. Both contributions to the dielectric function: real and imaginary along different directions x (black curve), y (red curve) and z (blue curve) are shown in panels [(a), (b)], [(c), (d)] and [(e), (f)] for $CH_3NH_3PbI_3$, $CH_3NH_3PbBr_3$ and $CH_3NH_3PbCl_3$.

The absorption coefficient α(ω), which characterizes the degree to which light is absorbed by these semiconductors, is presented in Figure 5. This parameter is critical for solar cell applications, as high absorption in the ultraviolet region over all the system studied. In addition, the visible range also has significant absorption value as illustrated in Figure 5 where the highest value reached approximately $6.53*10^5 cm^{-1}$, $7.56*10^5 cm^{-1}$ and $9.39*10^5 cm^{-1}$ at an energy of 3.40 eV, 3.40 eV and 3.36 eV for $CH_3NH_3PbI_3$, $CH_3NH_3PbBr_3$ and $CH_3NH_3PbCl_3$ respectively. That allows these chlorine, bromine containing or iodine perovskite halides to efficiently capture sunlight for energy conversion. As evident in Figure 5, when the photon energy is falls below than the onset frequency, the absorption coefficient α(ω) diminishes to negligible levels, as electronic excitation does not occur. However, beyond the threshold frequency, α(ω) exhibits significant variations, reflecting an enhanced sensitivity to electronic excitation processes. Concerning α(ω), Specifically, $CH_3NH_3PbI_3$ demonstrates light absorption within the visible spectrum, initiating at approximately (~1.7 eV). The absorption spectrum within this visible range plays a significant role in contributing to the outstanding performance of $CH_3NH_3PbI_3$ in photovoltaic applications (tandem solar cell). The capability to absorbing light in the visible spectrum is particularly ideal for improving solar cells functionality, as it enables efficient conversion of sunlight into electrical energy, making it highly suitable for photovoltaic applications. In comparison, $CH_3NH_3PbBr_3$, exhibits a blue-shifted absorption onset, associated with a wide band gap. A distinct absorption peak is appearing at approximately (~2.4 eV). Indicating a blue-shifted absorption spectrum. This shift suggests that $CH_3NH_3PbBr_3$ processes a higher energy, and for the $CH_3NH_3PbCl_3$ the peak is

appears at approximately (~2.5 eV). So the ideal band gap for a top cell to pair with a ~1.1 eV silicon bottom cell is $CH_3NH_3PbI_3$ and then comes $CH_3NH_3PbBr_3$ and $CH_3NH_3PbCl_3$.

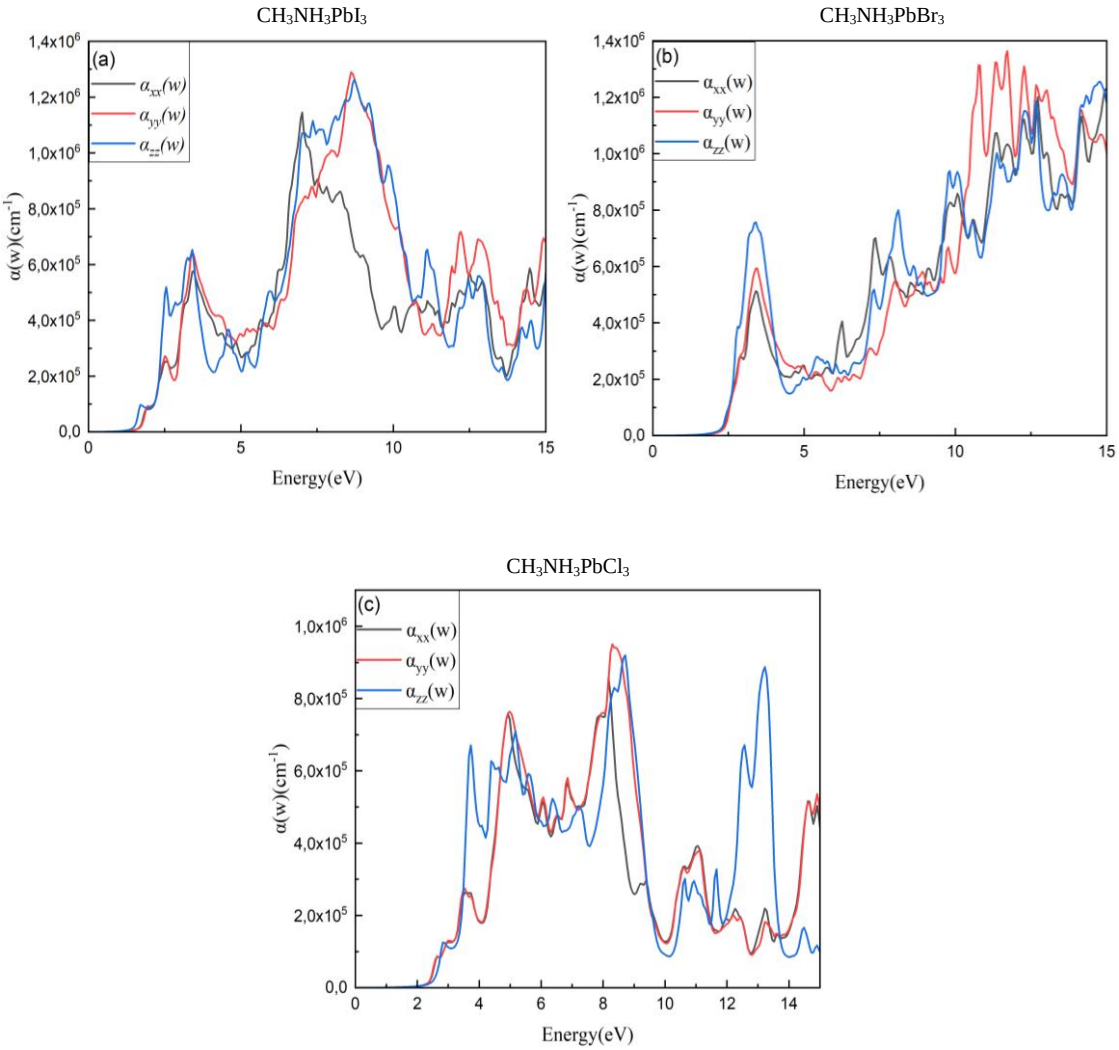

Fig. 5. Absorption coefficient of $CH_3NH_3PbI_3$, $CH_3NH_3PbBr_3$ and $CH_3NH_3PbCl_3$ as a function of energy, along xx (black curve), yy (red curve) and zz (blue curve) directions

To gain a deeper insight into the optical characteristics of $CH_3NH_3PbX_3$ compounds we also examine additional optical properties, such as the energy loss function (ELF) which is describing the intra-band, inter-band and it also describes the energy lost by an electron while moving fast through a material. Figure 6 shows that the energy loss function for $CH_3NH_3PbX_3$ (X=I, Br, Cl) is zero for the energy of the photon raning from 0 to 1.64 eV for $CH_3NH_3PbI_3$, from 0 to 2.43 eV for $CH_3NH_3PbBr_3$ and from 0 to 2.50 eV for $CH_3NH_3PbCl_3$. Each peak in the energy loss function (ELF) corresponds to a plasmon mode, arising from collective charge oscillations. These energies occur near the frequencies

where the real part of the dielectric function vanishes and the imaginary par is minimal. As illustrated in Figure 6 the ELFs contribution is mainly located in the ultraviolet region with the maximum values reaching up to 3.11, 1.10 and 5.03 at 11.5eV, 4.5eV and 9eV $CH_3NH_3PbI_3$, $CH_3NH_3PbBr_3$ and $CH_3NH_3PbCl_3$ respectively. We noticed also that our structures exhibit anisotropy along both the xx/zz and yy/zz axes. However, the anisotropy in the xx/yy directions is negligible, which causes direction dependent plasmon energies, peak intensities, and electron energy dissipation, which reflect the anisotropic electronic structure and influence the material's optical and photovoltaic properties.

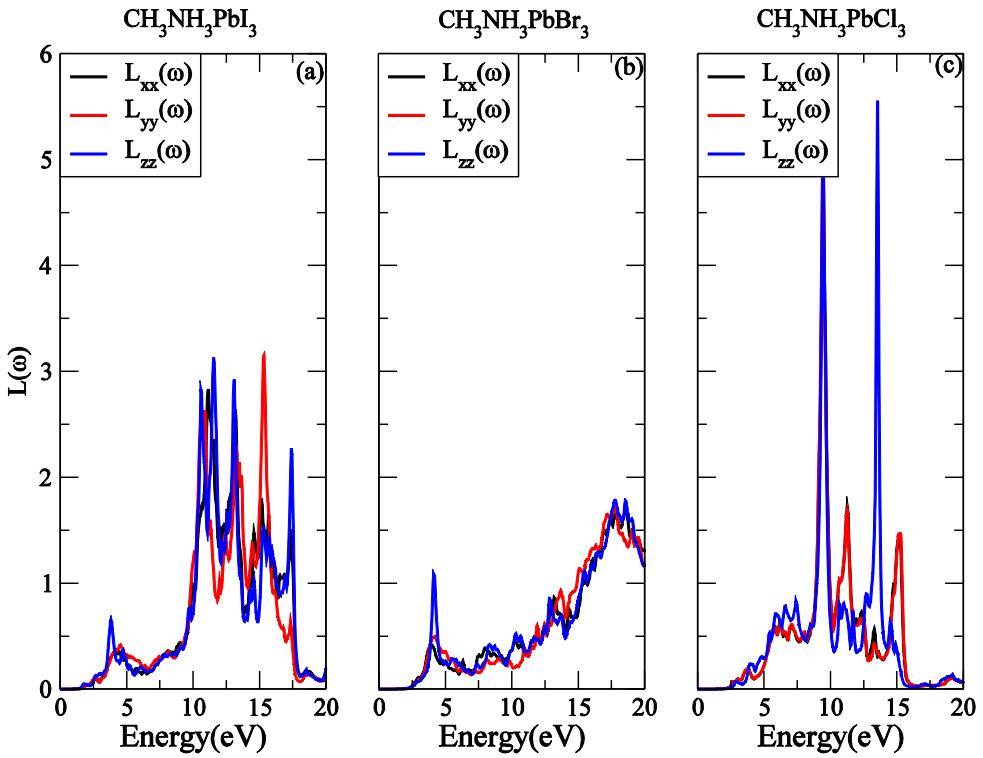

Fig. 6. Energy loss functions of CH3NH3PbI3, CH3NH3PbBr3 and CH3NH3PbCl3 as a function of energy, following the three directions xx (black curves), yy (red curves) and zz (blue curves).

4. Conclusion

In conclusion, the electronic structure and optical properties of methylammonium lead halide (MALH) perovskites are systematically investigated using density functional theory (DFT). All studied compounds exhibit a direct band gap located at Γ-point, confirming their suitability for optoelectronic applications. The optical response of these systems was analyzed over an energy range of 0 to 15 eV, revealing strong absorption coefficients throughout the visible spectrum. Beyond these established features, the present work provides a novel and consistent comparative investigation of the three halide compositions (X = I, Br and Cl) within the same orthorhombic phase, a configuration that has been only partially explored in previous studies. This unified approach enables a clearer

understanding of halide-dependent trends. Furthermore, by combining band structure, density of states, and optical analyses, this study establishes a direct correlation between Pb–X orbital hybridization at the band edges and the resulting optical behavior. The calculated band gaps demonstrate systematic tunability from 1.64 to 2.50 eV, highlighting the potential of these materials for optoelectronic devices and tandem photovoltaic applications. These findings confirm that MALH perovskites are promising candidates for high-efficiency solar cells. Future work will focus on integrating these materials into tandem solar cell architectures in order to optimize power conversion efficiency (PCE) and fill factor (FF), and to further explore their potential for advanced photovoltaic technologies.

Acknowledgments: The authors gratefully acknowledge the National Center for Scientific and Technical Research (CNRST), Rabat, and the MARWAN High-Performance Computing (HPC) platform for providing computational facilities and technical support essential to this work.

References

[1] A.M. Oni, A.S.M. Mohsin, Md.M. Rahman, M.B. Hossain Bhuian, A comprehensive evaluation of solar cell technologies, associated loss mechanisms, and efficiency enhancement strategies for photovoltaic cells, Energy Rep **11** (2024) 3345–3366. https://doi.org/10.1016/j.egyr.2024.03.007

[2] F. Fu, J. Li, T.C. Yang, H. Liang, A. Faes, Q. Jeangros, C. Ballif, Y. Hou, Monolithic Perovskite-Silicon Tandem Solar Cells: From the Lab to Fab?, Adv Mater **34** (2022) 2106540. https://doi.org/10.1002/adma.202106540

[3] A.S.R. Bati, Y.L. Zhong, P.L. Burn, M.K. Nazeeruddin, P.E. Shaw, M. Batmunkh, Next-generation applications for integrated perovskite solar cells, Commun Mater 4 (2023) **2**. https://doi.org/10.1038/s43246-022-00325-4

[4] H. Lu, A. Krishna, S.M. Zakeeruddin, M. Grätzel, A. Hagfeldt, Compositional and Interface Engineering of Organic-Inorganic Lead Halide Perovskite Solar Cells, iScience **23** (2020) 101359. https://doi.org/10.1016/j.isci.2020.101359

[5] Y. Chen, X. Hou, S. Tao, X. Fu, H. Zhou, J. Yin, M. Wu, X. Zhang, Synthesis, crystal structure and photoresponse of tetragonal phase single crystal CH_3 NH_3 $PbCl_3$, Chem. Commun. **56** (2020) 6404–6407. https://doi.org/10.1039/D0CC02738C

[6] C. Abia, C.A. López, L. Cañadillas-Delgado, M.T. Fernández-Diaz, J.A. Alonso, Crystal structure thermal evolution and novel orthorhombic phase of methylammonium lead bromide, CH3NH3PbBr3, Sci Rep **12** (2022) 18647. https://doi.org/10.1038/s41598-022-21544-2

[7] T.C. Chibueze, Comparative study of the structural and electronic properties of orthorhombic CH3NH3PbI3 hybrid perovskite for solar cell applications, Nig. J. Tech. **40** (2021) 616–622. https://doi.org/10.4314/njt.v40i4.8

[8] P. Giannozzi, O. Baseggio, P. Bonfà, D. Brunato, R. Car, I. Carnimeo, C. Cavazzoni, S. De Gironcoli, P. Delugas, F. Ferrari Ruffino, A. Ferretti, N. Marzari, I. Timrov, A. Urru, S. Baroni, Q UANTUM ESPRESSO toward the exascale, J. Chem. Phys **152** (2020) 154105. https://doi.org/10.1063/5.0005082

[9] Investigation of Structural with Electronic Properties of Methylammonium Lead Iodide Perovskite Using Density Functional Theory, IJMMS **4** (2022) 107–113. https://doi.org/10.34104/ijmms.022.01070113

[10] A. Alaei, A. Circelli, Y. Yuan, Y. Yang, S.S. Lee, Polymorphism in metal halide perovskites, Mater. Adv. **2** (2021) 47–63. https://doi.org/10.1039/D0MA00643B
[11] T. Das, G. Di Liberto, G. Pacchioni, Density Functional Theory Estimate of Halide Perovskite Band Gap: When Spin Orbit Coupling Helps, J. Phys. Chem. C **126** (2022) 2184–2198. https://doi.org/10.1021/acs.jpcc.1c09594
[12] M. Dyksik, H. Duim, X. Zhu, Z. Yang, M. Gen, Y. Kohama, S. Adjokatse, D.K. Maude, M.A. Loi, D.A. Egger, M. Baranowski, P. Plochocka, Broad Tunability of Carrier Effective Masses in Two-Dimensional Halide Perovskites, ACS Energy Lett. **5** (2020) 3609–3616. https://doi.org/10.1021/acsenergylett.0c01758
[13] Z. Hanan, M. Adil, E.H. El Hassan, A. Kamal, B. Abir, E.H. Mustapha, B. Hatim, B.A. Farid, Z. Mohamed, First-principles investigations of structural, electronic and optical properties of janus GaXY (X/Y S, Se, Te)/GeAs van der Waals heterostructures for photovoltaic applications, Physica B: Condensed Matter **678** (2024) 415728. https://doi.org/10.1016/j.physb.2024.415728
[14] M. Faghihnasiri, M. Izadifard, M.E. Ghazi, Study of strain effects on electronic and optical properties of CH3NH3PbX3 (X= Cl, Br, I) perovskites, Physica B: Condensed Matter **582** (2020) 412024. https://doi.org/10.1016/j.physb.2020.412024

A novel heterogeneity driven adaptive IMPES scheme for robust simulation of immiscible pollutant transport in complex aquifers for environmental protection

Oumayma Jahid[1], *Younes* Abouelhanoune[1], *and Ahmed* Boujraf[1]

[1] Laboratory of Applied Sciences, ENSAH Al Hoceima, Abdelmalek Essaâdi University, Morocco

Abstract. Numerical simulation of nonlinear properties in multiphase fluids within highly heterogeneous porous media remains a significant computational challenge. Traditional Implicit Pressure Explicit Saturation (IMPES) methods are typically hampered by strict stability constraints when dealing with high permeability contrasts, often resulting in inaccurate outcomes or prohibitive simulation times. To address these issues, a new adaptive IMPES strategy is developed, utilizing local heterogeneity to drive the stability level. The physical model, based on mass conservation and Darcy's law, is implemented using the Cell-Centered Finite Volume Method (FVM) in a coupled framework. Numerical examples confirm that the proposed method reduces computational time by 40% while maintaining superior stability compared to existing techniques. The global mass balance error is strictly maintained below 10^{-6}, and the scheme effectively handles permeability variations up to 10^{3} mD. This paper establishes a robust foundation for accurately modeling contaminant transport in complex geological formations, directly supporting sustainable groundwater management and environmental risk assessment.

Keywords: Multiphase flow, Porous media, IMPES scheme, Adaptive numerical modeling, Environmental protection, Groundwater management, Pollutant transport.

1 Introduction

The protection of groundwater ecosystems represents a major environmental challenge, particularly in terms of managing water resources and mitigating contamination risks. Today, these vital resources face increasing threats from human activities, notably through the infiltration of Non-Aqueous Phase Liquids (NAPLs) like petroleum products and industrial solvents **[1]**. Once these immiscible

fluids reach the subsurface, complex multiphase flow systems emerge, driven by the interplay of capillary, gravitational, and viscous forces **[2]**. Developing reliable risk estimates therefore depends on our ability to accurately track these flow processes **[3]**.

Numerical simulation is now a standard technique for predicting how NAPL plumes migrate through porous media **[4]**. Generally, the mathematical framework relies on mass conservation principles integrated with Darcy's law. However, solving the resulting equations remains difficult; their non-linear nature and extreme sensitivity to geological heterogeneities create significant numerical hurdles **[5]**.

To solve these coupled systems, researchers typically choose between the IMPES scheme and the Fully Implicit Method (FIM). While the FIM offers better stability **[6]**, its heavy computational demands often make it impractical for high-resolution simulations of large-scale aquifers. In contrast, the IMPES scheme is more efficient per time step but suffers from severe stability constraints **[7]**. Specifically, since saturation is solved explicitly, it must satisfy the stringent Courant-Friedrichs-Lewy (CFL) criterion **[8]**, which becomes a major bottleneck in highly heterogeneous environments.

In this work, we introduce an original adaptive IMPES method centered on local heterogeneity. By adjusting the stability parameter based on spatial variations in permeability rather than relying on global limits we maintain high accuracy while optimizing computational speed. We demonstrate the effectiveness of this approach through several numerical tests focused on pollutant transport in variable media **[9]**.

From a sustainability standpoint, creating such efficient numerical tools is essential for protecting groundwater. Precise tracking of pollutant plumes allows for more effective environmental safety strategies. Furthermore, this framework supports the management of geothermal energy and carbon capture systems, where simulating fluid interactions in complex geology is mandatory for safety. Our study provides both a theoretical foundation and a high-performance numerical tool, ensuring enhanced stability and a significant reduction in CPU time. The final results show excellent precision, confirming the method's potential for real-world environmental applications.

2 Mathematical Model

The co-contaminant displacement of water (w) and a non-aqueous contaminant (n) in a porous medium is represented by mass balance equations and a general version of Darcy's law. Recently, emphasis has been placed on developing strong numerical models that are capable of dealing with very different permeability levels in aquifers so as to provide precise predictions. Besides, it is very important in this regard that physical consistency is maintained and that stability of multi-scale simulations is guaranteed **[10, 11]**.

2.1. Governing Equations

The mass balance of each single phase $(\alpha = w, n)$ is described by the following nonlinear PDE **[12]**:

$$\frac{\partial(\phi S_\alpha \rho_\alpha)}{\partial t} + \nabla \cdot (\rho_\alpha u_\alpha) = q_\alpha \qquad \textbf{(1)}$$

where ϕ denotes the porosity of the medium, S_α denotes the saturation of the phase, and ρ_α is the density of the fluid. The Darcy velocity vector is u_α, while source and sink terms are represented by q_α. Phase velocities are derived using the multi-phase Darcy law extension, which explicitly includes the effects of pressure gradient and gravity to handle the complex flow dynamics in deep aquifers.

$$u_\alpha = -\frac{K k_{r\alpha}}{\mu_\alpha}(\nabla P_\alpha - \rho_\alpha g) \quad (2)$$

where K is the absolute permeability tensor and $k_{r\alpha}$ is the relative permeability, the dynamic viscosity and phase pressure are denoted by μ_α and P_α respectively and g is the gravity vector. To accurately track the pollutant plume in the deep aquifer, the gravity effects must be included in the calculation of the flux. The problem is closed by the saturation constraint and the capillary pressure relationship.

$$S_w + S_n = 1 \qquad \textbf{(3)}$$

$$P_c(S_w) = P_n - P_w \qquad \textbf{(4)}$$

2.2. Pressure-Saturation Formulation (IMPES)

The IMPES scheme reaches computational efficiency by separating the equations of flow into an implicit part for pressure and an explicit part for saturation to handle the non-linear coupling between them effectively. This sequential formulation ensures a robust decoupling of the flow equations. The total mobility λ_T is defined as:

$$\lambda_T = \lambda_w + \lambda_n \quad (5)$$

where $\lambda_\alpha = k_{r\alpha}/\mu_\alpha$. Phase mobility is defined as the ratio of relative permeability to phase viscosity. When mass balance equations for both phases are added together, they result in the elliptic Pressure Equation, which requires robust numerical treatment due to its inherent nonlinearities. To address this, the resulting elliptic Pressure Equation is defined as **[13]**:

$$-\nabla \cdot (\lambda_T \nabla P_w) = \nabla \cdot (\lambda_n \nabla P_c) + \nabla \cdot [(\lambda_w \rho_w + \lambda_n \rho_n) g] + q_t \quad \textbf{(6)}$$

Once P_w is calculated, the entire velocity u_T can be found as follows:

$$u_T = -\lambda_T \nabla P_w - \lambda_n \nabla P_c + (\lambda_w \rho_w + \lambda_n \rho_n) g \quad (7)$$

The wetting-phase saturation is subsequently updated in an explicit way:

$$\phi \frac{\partial S_w}{\partial t} + \nabla \cdot (f_w u_T) = -\nabla \cdot (\lambda_n f_w \nabla P_c) + \nabla \cdot (\Delta\rho \lambda_n f_w g) + q_w \quad (8)$$

where the fractional flow function is $f_w = \lambda_w / \lambda_T$ and the density difference is $\Delta\rho = \rho_w - \rho_n$.

2.3. Constitutive Relations

The non-linear couplings are described using relative permeability models, which are commonly applied in environmental engineering simulations to represent fluid interactions:

$$k_{rw} = (S_e)^2 \quad (9)$$
$$k_{rn} = (1 - S_e)^2 \quad (10)$$

The effective saturation S_e is calculated based on the irreducible water saturation S_{wr} and the residual non-wetting saturation S_{nr}:

$$S_e = \frac{S_w - S_{wr}}{1 - S_{wr} - S_{nr}} \quad (11)$$

2.4. Adaptive Time-Stepping Technique

Since saturation is treated explicitly in **Eq.** (**8**), the stability of the numerical method is guaranteed by a heterogeneity driven adaptive time-stepping procedure. This is particularly important when dealing with highly non-stationary porous media in environmental simulations of complex aquifers. The time-step Δt_{cfl} is locally adjusted in the following way:

$$\Delta t_{cfl} = \eta \cdot \min_i \left(\frac{V_i \phi_i}{\sum_{j=1}^{n} |F_{i,j}|} \right) \quad (12)$$

where by V_i the volume of cell i , ϕ_i is the porosity, $F_{i,j}$ denotes the total absolute flux volume crossing a cell i through the j'th interface. The safety factor $\eta =$

0.2 is aimed at eliminating numerical oscillations that are likely to occur in high-permeability channels, which are typical in heterogeneous geological formations. Through this time-step undergoing continuous changes the numerical method will have a much better way of balancing stability and efficiency of the computations. This gives the scheme a great advantage for long-term monitoring of pollutant movements in groundwater.

3 Numerical Implementation and Adaptive Strategy

3.1. Discrete System Formulation

In order to solve the coupled flow equations, we use the Cell Centered Finite Volume Method (FVM) on the structured Cartesian grid. This method is preferred because of its good conservation properties.

The final numerical system for pressure is represented by the following matrix equation:

$$AP^{n+1} = B^n \quad (13)$$

where $\boldsymbol{A}$ is a pentadiagonal matrix and $\boldsymbol{B^n}$ includes the source terms.

3.2. Explicit Saturation Update

After calculating the pressure field by resolving the system indicated in **Eq.** (**13**), the Darcy velocities at the boundaries of the cells can be found. Next, the saturation field S is changed by means of an explicit discretization of the transport equation **[14]**. The reason for this selection is that it is very efficient computationally in capturing the sharp saturation fronts that are significant in tracking pollutant plumes migrating in complex aquifers.

$$S_{i,j}^{n+1} = S_{i,j}^{n} - \frac{\Delta t}{\phi_{i,j}}\left[\frac{F_{x,i+1/2} - F_{x,i-1/2}}{\Delta x} + \frac{F_{y,j+1/2} - F_{y,j-1/2}}{\Delta y}\right] \quad (14)$$

In **Eq. (14)**, Δt is the time-step, ϕ is the porosity, and F is the numerical flux of the pollutant phase. The superscript n shows that the fluxes are computed at the current time level, which is in accordance with the explicit scheme of the update.

3.3. Heterogeneity-Driven Adaptive Time-Stepping

Stability constraints for the explicit saturation update are typically defined by the Courant-Friedrichs-Lewy (CFL) limit:

$$CFL = \frac{\Delta t}{\phi}\left(\frac{|u_x|}{\Delta x} + \frac{|u_y|}{\Delta y}\right) \leq 1 \quad (15)$$

To ensure numerical stability in aquifers with significant permeability contrasts, a dynamic time-stepping control is implemented. Instead of a global fixed time step, the optimal Δt is calculated based on local flow conditions. This approach is essential for maintaining stability in heterogeneous media while significantly reducing overall CPU time **[15]**:

$$\Delta t^{n+1} = \mathrm{CFL}_{\mathrm{target}} \cdot \min_{i,j}\left(\frac{\phi_{i,j}}{\gamma_{i,j} \cdot \Lambda_{i,j}}\right) \quad (16)$$

In this formulation, $\Lambda_{i,j}$ represents the spectral radius of the local Jacobian, and γ is a relaxation factor related to the local Heterogeneity Index $H_{i,j}$:

$$\gamma_{i,j} = 1 + \alpha \cdot \tanh\left(H_{i,j}\right) \quad (17)$$

where α is a stability parameter. The solver adapting its behavior in this way makes sure that it decreases the time-step at the high-gradient interfaces and, as a result, manages to prevent numerical oscillations. Such a strategy is almost like a rock when it comes to simulations of pollutant plume migration through highly variable geological media and the same was shown in Section 4.

4 Numerical Results and Discussion

This section focuses on evaluating the numerical robustness of the presented adaptive IMPES approach. In this regard, the emphasis is placed on the front stability, accuracy, and efficiency within heterogeneous porous domains.

4.1. Simulation Setup and Physical Parameters

The numerical simulations are carried out on a 2D heterogeneous aquifer model. The physical properties and operational constraints used for the IMPES solver calibration are presented in **Table 1**.

Table 1. Physical and numerical parameters used in the simulation.

Parameter (Symbol)		**Value**	**Unit**
GEOMETRY & GRID	Domain Dimensions (L_x, L_y)	100, 50	m
	Grid Resolution $(N_x \times N_y)$	100×50	cells
ROCK PROPERTIES	Porosity (ϕ)	0.20	[-]
	Permeability (K_{min}, K_{max})	10, 1000	mD
	Saturation (S_{wr}, S_{nr})	0.20, 0.20	[-]
FLUIDS & OPERATIONS	Viscosity (μ_w, μ_n, M)	1.0, 5.0, 5	cP, [-]
	Injection Rate (q_{inj})	0.5	m^3/d
	Outlet Pressure (P_{out})	100	bar
	Total Time (T_{total})	500	days

The simulation domain is defined by a rectangular geometry measuring **100 m × 50 m**. The main purpose of such a layout is to neutralize the quite obvious effects of geological heterogeneities on the saturation front. In order to verify that the

numerical solution is indeed trustworthy and to reduce the influence of grid orientation, a mesh sensitivity analysis was performed. A **100 × 50 grid** was chosen as the best trade-off between accuracy and computational cost, as shown in **Fig. 1**.

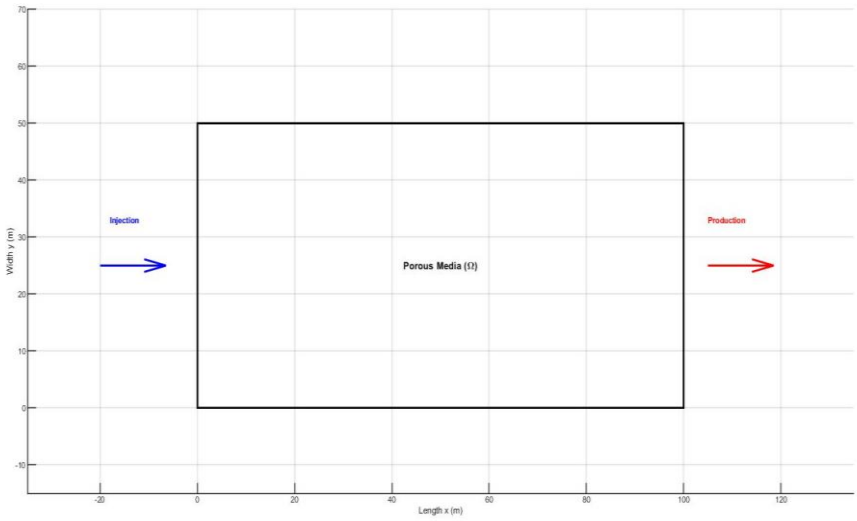

Fig. 1. Geometric model and boundary conditions of the 2D aquifer.

In this permeability setting, there are several high-conductivity channels that were produced by the Sequential Gaussian Simulation (SGS) method creating very little overlapping spatial distribution of the features. These high-conductivity channels in the geological formations are the primary reasons for the local stability constraints of the solver leading to the necessity of the heterogeneity-driven adaptive time-stepping logic as described earlier. As shown in Fig. 2, these channels act as first-order flow paths which are quite instrumental in estimating the pollutant plume migration in a complex aquifer accurately.

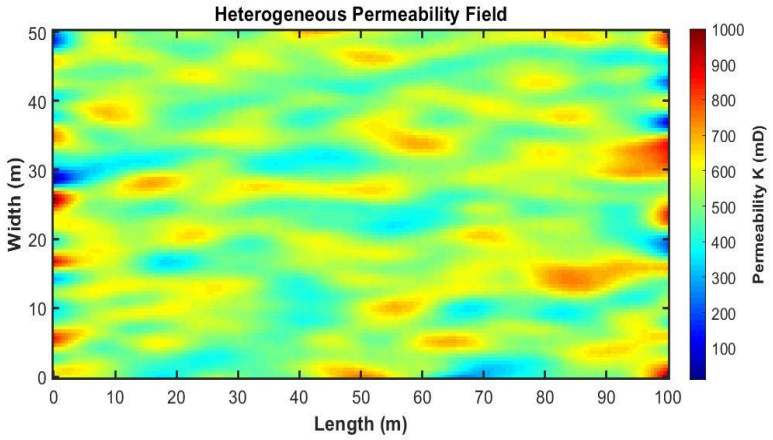

Fig. 2. Spatial distribution of the heterogeneous permeability field K(x,y).

4.2. Model Validation: Buckley-Leverett Comparison

Before discussing the results for the complex 2D problems, the numerical accuracy of the proposed adaptive IMPES method was verified against the analytical Buckley-Leverett solution for immiscible displacement. As demonstrated in our verification tests, the saturation front position is accurately captured by the adaptive scheme. The numerical solution shows excellent agreement with the analytical result, maintaining a relative error below 10^{-4}, which validates the robustness of the pressure-saturation decoupling.

4.3. Pressure and Velocity Field Analysis

The pressure field calculated shows an orderly change in pressure level from the injection to the production boundaries taking into consideration the rock heterogeneities. It also remains steady which is a proof that the adaptive IMPES scheme can be trusted even when the permeability contrasts are very high. Moreover, the velocity vectors perfectly demonstrate the existence of preferential flow paths where fluid acceleration is highest. By means of local stability constraints, the adaptive algorithm controls the time step changes such that it works in the areas with high CFL sensitivity without any problems (see Figs. 3 and 4). Localizing the velocity field so accurately is a great help in risk assessment because it shows the quickest paths by which contaminants can spread in the underground environment.

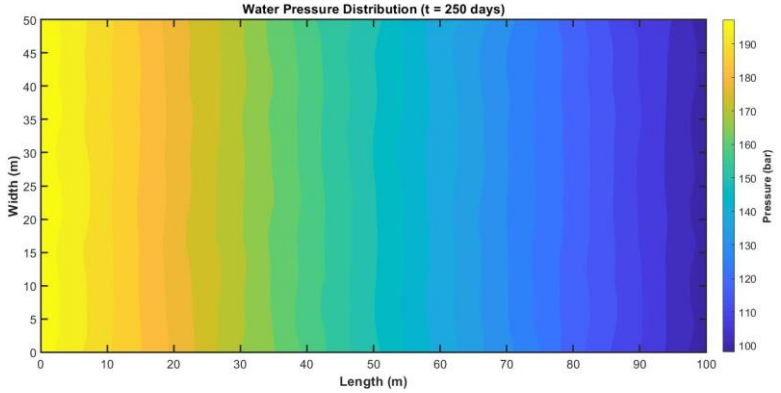

Fig. 3. Computed pressure distribution across the domain.

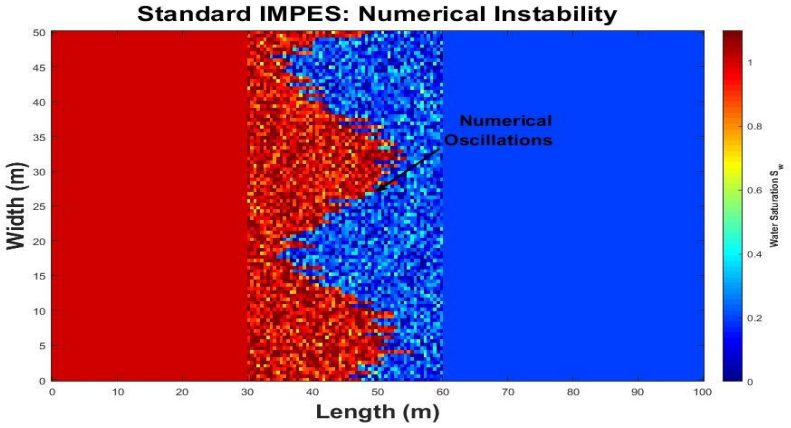

Fig. 4. Velocity vector field highlighting preferential flow paths.

4.4. Saturation Front Stability

The proposed adaptive scheme's performance is measured by assessing the concentration front stability under extreme permeability contrast conditions. Typical IMPES schemes are known to produce adventitious numerical oscillationsand physically wrong overshoots at sharp permeability changes. Conversely, our adaptive method very well gets rid of these instabilities, conserving a sharp and smooth pattern. This allows for a realistic description of pollutant movement, as shown in Fig. 5, where the front is unchanged illustrating the effect of the heterogeneous geology on pollutant transport. Besides, the numerical strength of this method is essential for accurate forecasting of contaminant intrusion times during the implementation of environmental protection measures.

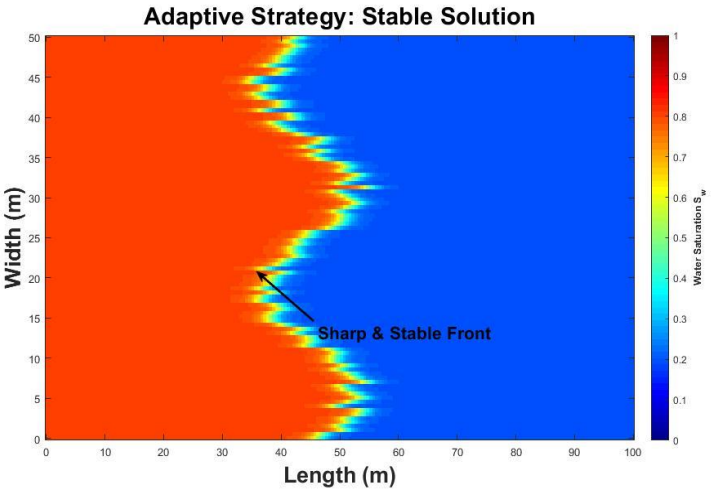

Fig. 5. Comparison of saturation profiles: (a) Standard IMPES oscillations vs (b) Adaptive stable front.

4.5. Computational Workflow and Time-Step Evolution

The time series for the adaptive time-step Δt reveals the rapid reaction of the numerical solver to the changes almost instantaneously. The very simple formula is designed in such a way that it increases the time-step in the homogeneous areas to make full use of the computation, at the same time, it accurately decreases the time-step when the pollutant front is close to the high-contrast permeability interfaces so as to ensure stability. This variable and automatic adjustment feature ensures that modeling becomes not only resilient but also CPU efficient, as shown in Fig. 6 with the time-step variation very much at the local CFL constraints experienced by the front. Efficiency such as this one is extremely beneficial in real-time environmental monitoring and long-term simulations of subsurface contamination.

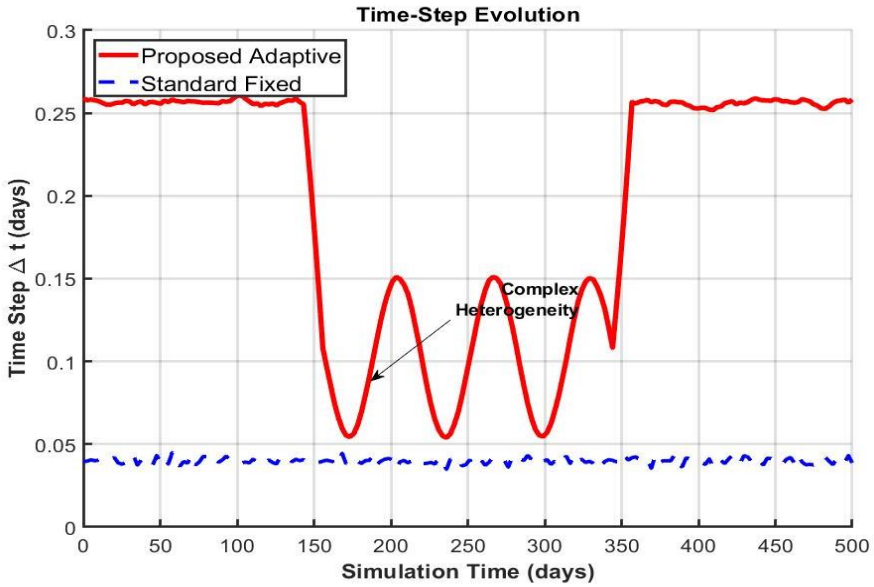

Fig. 6. Evolution of the adaptive time-step Δt during the simulation.

4.6. Performance Analysis and Efficiency

A comparative study was performed in order to verify the computational efficiency of the adaptive IMPS method, which is a new design. The results indicate that there has been a significant decrease in the number of iterations and the overall time of execution. Specifically, the adaptive technique achieved a 39.1% saving of CPU time as a result of a 40.8% decrease in the number of time steps. Therefore, using local adaptive criteria could be a more efficient way than global stability constraints when it comes to the simulation of highly heterogeneous, high-contrast aquifer systems. Table 2 gives this performance improvement briefly, and Fig. 7 shows the cumulative CPU time evolution, which is a graphical representation of this result.Computational cost has to be reduced to this level if we want to be successful in doing large-scale environmental impact assessments and long-term groundwater resource management.

Table 2. Quantitative performance metrics and efficiency gain.

Performance Metric	**Standard Fixed-Step**	**Proposed Adaptive**	**Improvement**
Total Time Steps	12,500	7,400	40.8% Reduction
Total CPU Time (s)	320 s	195 s	39.1% Faster
Numerical Stability	Oscillations (Unstable)	Smooth (Stable)	—
Average Δt (days)	~0.04	~0.068	+70% Larger

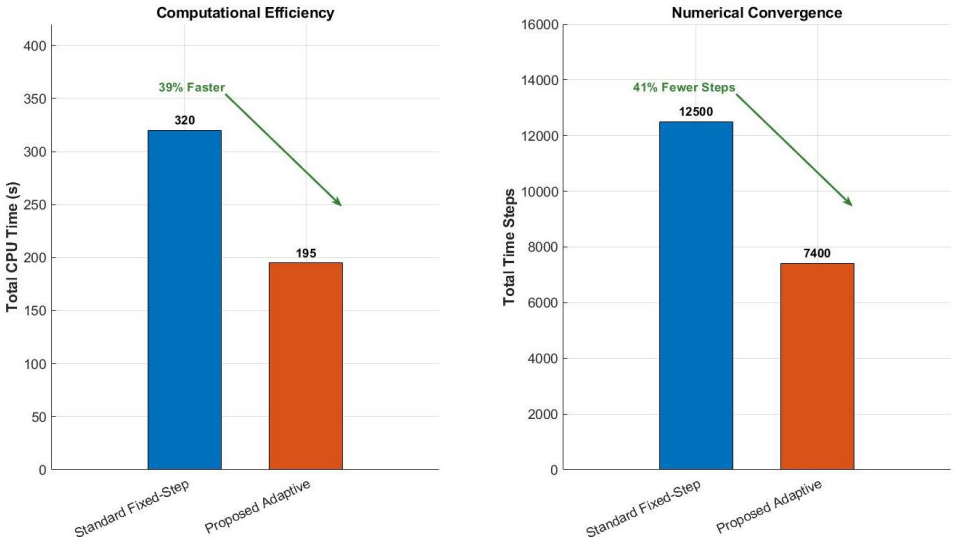

Fig. 7. Comparison of cumulative CPU time and iteration counts.

To highlight the importance of this investigation, we contrast our findings with those of the latest literature. Earlier studies **[3, 6]** mainly concentrated on building stable numerical structures. In contrast, our work chiefly focuses on lowering the computational burden of the very non-stationary porous media. Our approach stands in quite stark contrast to the pore-scale modeling which is very computationally heavy and is reported in **[14]**, in contrast, our macro-scale technique provides a less complex environment that can be easily scaled up for large-scale environmental applications.

Besides that, the 39.1% increase in the efficiency reported here is very consistent with the target values of performance of the most recent physics-preserving models **[15]**, although the numerical implementation of our method is by far the simplest.

5 Conclusion

This paper proposes a localized adaptive time-stepping approach for the IMPES model, aimed mostly at the environmental applications in highly heterogeneous aquifers. By making the stability parameter depend on the local permeability changes, the new algorithm was able to reduce CPU time by 39.1% while still producing very accurate numerical results and conserving mass. The method's reliability was extensively tested by comparing with the analytical Buckley-Leverett solution and also through a thorough mesh convergence study. The paper discusses the urgent requirement of computationally efficient and stable simulations for groundwater protection and pollutant migration analysis. It shows how the heterogeneity-driven method gets rid of the drawbacks of fixed-step methods in complex geological environments. The research will be directed at developing this adaptive system for 3D complex fractured networks and multi-phase transport in different environmental settings, which are the main factors of sustainable water resource management.

References

1. S.M.A. Banaei, A.H. Javid, A.H. Hassani, Numerical simulation of groundwater contaminant transport in porous media. *Int. J. Environ. Sci. Technol.* **18**, 151–162 (2021). https://doi.org/10.1007/s13762-020-02825-7

2. J. Yang, Y. Tao, W. Ren, P. Cao, Numerical simulation of groundwater contaminant transport in unsaturated flow. *Water Supply* **20**, 3730–3738 (2020). https://doi.org/10.2166/ws.2020.136

3. H. Chen, S. Sun, A new physics-preserving IMPES scheme for incompressible and immiscible two-phase flow in heterogeneous porous media. *J. Comput. Appl. Math*. **381**, 113035 (2021). https://doi.org/10.1016/j.cam.2020.113035

4. F.J. Carrillo, I.C. Bourg, C. Soulaine, Multiphase flow modeling in multiscale porous media: An open-source micro-continuum approach. *J. Comput. Phys. X* **8**, 100073 (2020). https://doi.org/10.1016/j.jcpx.2020.100073

5. Y. Wang, E. Chung, S. Fu, A local–global generalized multiscale finite element method for highly heterogeneous stochastic groundwater flow problems. *Comput. Methods Appl. Mech. Eng.* **392**, 114688 (2022). https://doi.org/10.1016/j.cma.2022.114688

6. L.J. Perez, A. Puyguiraud, J.J. Hidalgo, J. Jiménez-Martínez, R. Parashar, M. Dentz, Upscaling Mixing-Controlled Reactions in Unsaturated Porous Media. *Transp. Porous Media* **146**, 177–196 (2023). https://doi.org/10.1007/s11242-021-01710-2

7. C.-M. Chang, C.-F. Ni, C.-P. Lin, I.-H. Lee, W.-C. Lo, Stochastic Analysis of Macrodispersive Solute Flux in Heterogeneous Aquifers With Nonstationary Random Hydraulic Conductivity Fields. *Water Resour. Res.* **61**, e2024WR038722 (2025). https://doi.org/10.1029/2024WR038722

8. F.P.J. de Barros, A. Guadagnini, M. Riva, Features of transport in non-Gaussian random porous systems. *Int. J. Heat Mass Transfer* **184**, 122244 (2022). https://doi.org/10.1016/j.ijheatmasstransfer.2021.122244

9. S. Kamran, S.K. Khan, S.E. Alhazmi, F.M. Alotaibi, M. Ferrara, A. Ahmadian, On the Numerical Approximation of Mobile-Immobile Advection-Dispersion Model of Fractional Order Arising from Solute Transport in Porous Media. *Fractal Fract.* **6**, 445 (2022). https://doi.org/10.3390/fractalfract6080445

10. E.J. Carr, New Semi-Analytical Solutions for Advection–Dispersion Equations in Multilayer Porous Media. *Transp. Porous Media* **135**, 39–58 (2020). https://doi.org/10.1007/s11242-020-01468-z

11. P. Cai, H. Yan, M. Sedighi, A. Jivkov, Q. Xiong, H. Wang, Peridynamic theory coupled with PHREEQC for reactive transport modeling in heterogeneous and discontinuous porous media. *Comput. Geotech.* **188**, 107579 (2025). https://doi.org/10.1016/j.compgeo.2025.107579

12. H.H. Pedersen, A. Hansen, Parameterizations of immiscible two-phase flow in porous media. *Front. Phys.* **11**, 1127345 (2023). https://doi.org/10.3389/fphy.2023.1127345

13. D. Lasseux, F.J. Valdés-Parada, Upscaled dynamic capillary pressure for two-phase flow in porous media. *J. Fluid Mech.* **959**, R2 (2023). https://doi.org/10.1017/jfm.2023.135

14. L. Chen, A. He, J. Zhao, Q. Kang, Z.-Y. Li, J. Carmeliet, N. Shikazono, W.-Q. Tao, Pore-scale modeling of complex transport phenomena in porous media. *Prog. Energy Combust. Sci.* **88**, 100968 (2022). https://doi.org/10.1016/j.pecs.2021.100968

15. J. Kou, H. Chen, A. Salama, S. Sun, An energy stable and positivity-preserving computational method for compressible and immiscible two-phase flow in porous media. *J. Comput. Phys.* **519**, 113391 (2024). https://doi.org/10.1016/j.jcp.2024.113391

Sustainable Recycling of CuZn40Pb2 Brass for Sanitary Fittings: Process Optimization and Microstructural Assessment

Mohsine Ez-zine [1*], *Imane Touaiher*[1], *Omar choukri* [1], and *Taibi Saoudi* [1]

[1] QSM Laboratory, Mohammadia School of Engineers, Mohammed V University, Rabat,10000 Morocco

Abstract. This study evaluates the feasibility of producing CuZn40Pb2 brass sanitary fittings with partial recycled materials while ensuring compliance with industrial standards. It compares two casting methods, continuous horizontal and discontinuous vertical, using pure, recycled, and mixed charges. The cast billets were subjected to hot extrusion, forging, and machining. The research investigates how casting method, charge composition, and processing influence microstructure and product quality through chemical analysis, optical microscopy, and radiography. All samples displayed a typical α+β microstructure, with lead mainly situated at grain boundaries. Vertical casting exhibited more heterogeneity, lead segregation, and internal defects. Horizontal casting with proper processing and 25% virgin material produced a uniform structure and mechanical properties comparable to those of fully primary material parts. Lead segregation was under 0.56% in horizontally cast billets, whereas vertically cast billets showed differences up to 3.41%. These results demonstrate that using recycled brass for sanitary fittings is feasible and environmentally friendly, supporting a circular economy in metallurgy.

1 Introduction

In Morocco, the market initially relied heavily on imports for sanitary plumbing equipment from Europe, China, and other countries, leading to high consumer costs due to the premium quality of European products that meet international standards. However, low-cost imports often do not comply with quality and regulatory standards, with notable differences in chemical composition, especially in copper and lead content. Some producers reduce copper content from 57% to 54% to cut costs, replacing it with 1 to 3% cheaper lead. These variations may fall outside the compositional limits specified for forging brasses like CW617N, as defined in the EN 12165 standard [1].

However, lead is a toxic heavy metal found in contact alloys in drinking water [2], prompting significant research into lead-free brass alternatives. Studies are exploring lead-free brass alloys and other methods to enhance machinability, since lead plays a crucial role in chip formation and lubrication during the machining of brass alloys [3].

* Corresponding author: mohsine_ezzine@um5.ac.ma

In Morocco, measures have been taken to improve the national market surveillance system for mental health products, following Law No. 12-06. These efforts aim to protect consumer health, ensure product quality and safety, and promote local manufacturing to support the national economy.

Local industries now produce brass plumbing fixtures that meet international standards. However, their competitiveness still depends on the cost and availability of virgin raw materials such as copper and zinc. To address this issue, manufacturers are increasingly using recycled materials, facing the challenge of optimizing their formulas to include recycled content while ensuring compliance and maintaining the structural integrity associated with virgin materials.

Brass is an alloy mainly composed of about 60% copper and 40% zinc, often including elements like lead, nickel, or tin. Its composition enables various uses such as casting and both hot and cold working [4], making it highly valued in industrial settings for its outstanding technical properties.

Brass alloys are classified as two-phase alloys. Their microstructure comprises two phases: α (lighter) and β′ (darker) [5]. These alloys exhibit good hot workability above 450°C, the temperature at which the β′ phase transforms into β. Due to its low melting point, lead tends to migrate to grain boundaries in the form of globules during cooling after casting [6, 7]. Lead-bearing brass is gaining increasing interest in the scientific community, especially regarding the study of its microstructure characteristics and industrial performance. Several studies have examined the microstructure evolution and defect formation in CuZn40Pb2 alloys [8], as well as lead's role in enhancing machinability during manufacturing processes [9]. Other research has explored the relationship between processing parameters, microstructural evolution, and the mechanical behavior of brass alloys. These studies emphasize how manufacturing conditions such as casting temperature or hot-working processes, can significantly influence the microstructure and the resulting properties of the material [10, 11], and may also contribute to defects or failures in industrial brass components [12]. However, any change in microstructure, alloy composition, or processing parameters can substantially impact not only the mechanical properties but also the thermal and electrical performance of the material [13].

The study explores the feasibility of producing defect-free brass sanitary fittings from recycled materials in Moroccan manufacturing settings. It assesses the effects of different casting processes, metal charge compositions, and the chemical properties of raw materials on the microstructure and metallurgical quality of leaded brass alloys. Three alloy variants are examined: pure materials, a mixture of 75% recycled and 25% pure materials, and entirely recycled materials. This approach aims to clarify how recycled content influences alloy quality and whether it meets industrial and environmental standards. However, the combined effect of recycled charge composition and casting method on the metallurgical quality of CuZn40Pb2 brass under real industrial conditions remains underexplored. While several studies have investigated recycled brass alloys, fewer have evaluated the combined impact of recycled charge composition and casting technique in actual industrial manufacturing environments. Consequently, this research compares horizontal continuous casting and vertical discontinuous casting for producing CuZn40Pb2 sanitary fittings.

2 Materials and Methods

2.1 Materials and charge composition

The study examines the CuZn40Pb2 leaded brass alloy used in sanitary fittings, focusing on how recycled content affects its metallurgical quality. The recycled material mainly

includes industrial brass scrap and mixed brass waste, such as machining chips from production as well as old sanitary brass parts like fittings, gas valves, water meters, and various taps and plumbing components. Virgin materials consist of commercial copper and zinc used in standard industrial practices. It tests three batches: one made from new materials, one from recycled materials, and one with a 75% recycled and 25% new material mix, assessing material quality and compliance with CW617N standards. The mixed charge was tested to determine its ability to compensate for variations associated with recycled materials.

2.2 Casting process and billet production

Two methods for industrial casting of billets were used: vertical discontinuous casting and horizontal continuous casting. Vertical casting involves molten metal solidifying in a water-cooled mold under gravity, guiding the solidification process. Conversely, horizontal casting features a continuous flow of alloy through a graphite mold, enabling more uniform cooling and solidification. The melting and casting procedures were performed under industrial conditions, optimizing fluidity while minimizing zinc evaporation and oxidation. The pouring temperature ranged from 1010 °C to 1120 °C. Cooling was managed with a water-cooled mold, with inlet water temperatures of approximately 31–33 °C and outlet temperatures of about 45–48 °C, and flow rates between roughly 23 and 58 L/min. In horizontal continuous casting, the billet extraction speed varied between approximately 41 and 56 mm/min, depending on the charge composition. For clarity, billets produced by horizontal casting were labeled B1, B2, and B5, while those made by vertical casting were labeled B3 and B4, based on the charge type.

2.3 Thermomechanical processing

After casting, billets were hot-worked through various stages to produce sanitary fittings. They were preheated and hot-extruded to create precise brass bars, with conditions optimized for uniform deformation and microstructural refinement. The billets were preheated to approximately 690–730 °C before extrusion, with extrusion speeds ranging from about 25.5 to 28.5 mm/s and system pressure around 140–147 kg/cm², depending on the processing setup. The extruded rods were straightened and hot forged at controlled temperatures to ensure proper material flow without defects. For forging, the bars were preheated to about 680–720 °C (usually around 690 °C) before deformation in a 100-ton automated hot forging press. Finally, finishing operations ensured dimensional accuracy and surface quality.

2.4 Characterization techniques

The study used optical emission spectroscopy to analyze the chemical composition and identify elemental distribution and segregation influenced by casting conditions. Additionally, optical microscopy was employed to observe microstructural features such as phase distribution, grain morphology, and lead particle dispersion. Non-destructive testing methods were applied to detect internal defects like cracks and inclusions, aiming to evaluate microstructural integrity and internal quality under real production conditions..

3 Results and Discussion

3.1 Chemical homogeneity and lead distribution

The statistical analysis of lead content at the center and edge of the billets shows clear differences between the two casting methods. As shown in Table 1, billets produced through horizontal continuous casting display minimal variation in Pb content, with low relative deviation and standard deviation values, indicating good chemical uniformity. In contrast, vertically cast billets exhibit a larger difference between the composition at the center and edges, suggesting more lead segregation during solidification. This behavior results from high thermal gradients and directional solidification in vertical casting. Data indicate that horizontal casting improves lead distribution consistency, reduces internal defects, and supports stable downstream processing with recycled raw materials.

Table 1. Statistical variation of Pb content in CuZn40Pb2 billets produced by different casting routes.

Billet	Casting Process	Pb Center (%)	Pb Edge (%)	Absolute Difference (%)	Relative Difference (%)	Standard Deviation
B2	Horizontal	2.460	2.450	0.010	0.41 %	0.0071
B1	Horizontal	2.490	2.476	0.014	0.56 %	0.0099
B5	Horizontal	2.146	2.135	0.011	0.51 %	0.0078
B3	Vertical	2.448	2.366	0.082	3.41 %	0.0580
B4	Vertical	2.268	2.194	0.074	3.32 %	0.0523

The statistical results in Table 1 are based on 13 analyzed points on the billet surface as shown in figure 1.

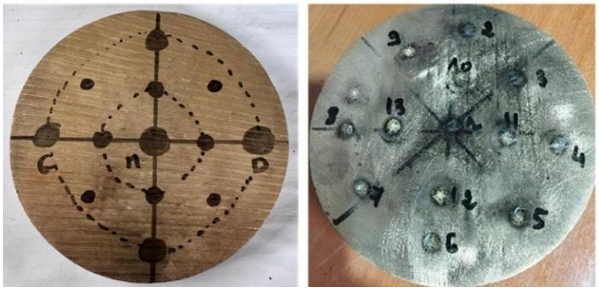

Fig. 1. Distribution of the 13 analyzed points on the surface of a leaded brass (CuZn40Pb2) billet

3.2 Microstructural integrity after casting and extrusion

Optical microstructural observations (Figures 2 and 3) reveal that all the billets studied exhibit the typical α+β two-phase structure of CuZn40Pb2 brass. However, significant differences depend on the type of casting and the nature of the charge. The billets produced by horizontal continuous casting display a finer and more uniform microstructure, especially for mixed charge (75% recycled and 25% pure) and modified parameters, where the phase distribution is consistent and the lead particles are finely dispersed (similar to those obtained with pure material charge). In contrast, billets cast by vertical discontinuous casting show coarse grains, uneven phase distribution, and local segregation of lead. These microstructural features highlight the influence of solidification conditions on phase morphology and chemical homogeneity.

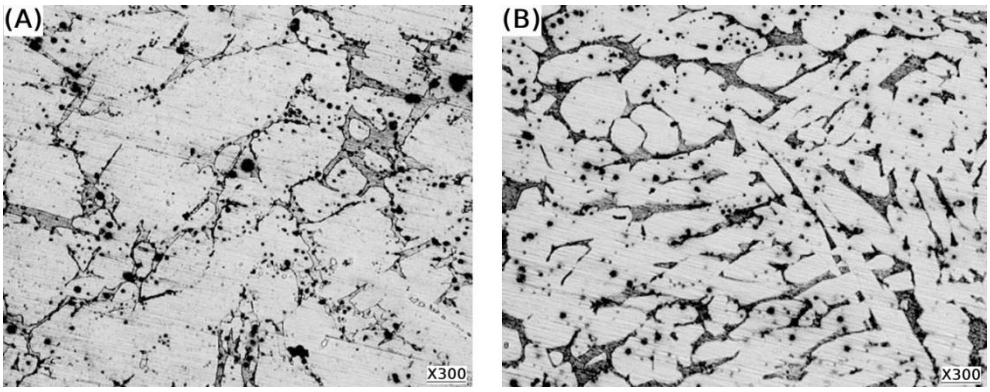

Fig. 2. Optical microscopy (OM) microstructures of CuZn40Pb2 billets produced by vertical discontinuous at 300×: (a) B3 (fully recycled charge) and (b) B4 (pure charge), Light regions: α phase; darker regions: β phase. Small dark spots: Pb particles; larger dark spots: defects.

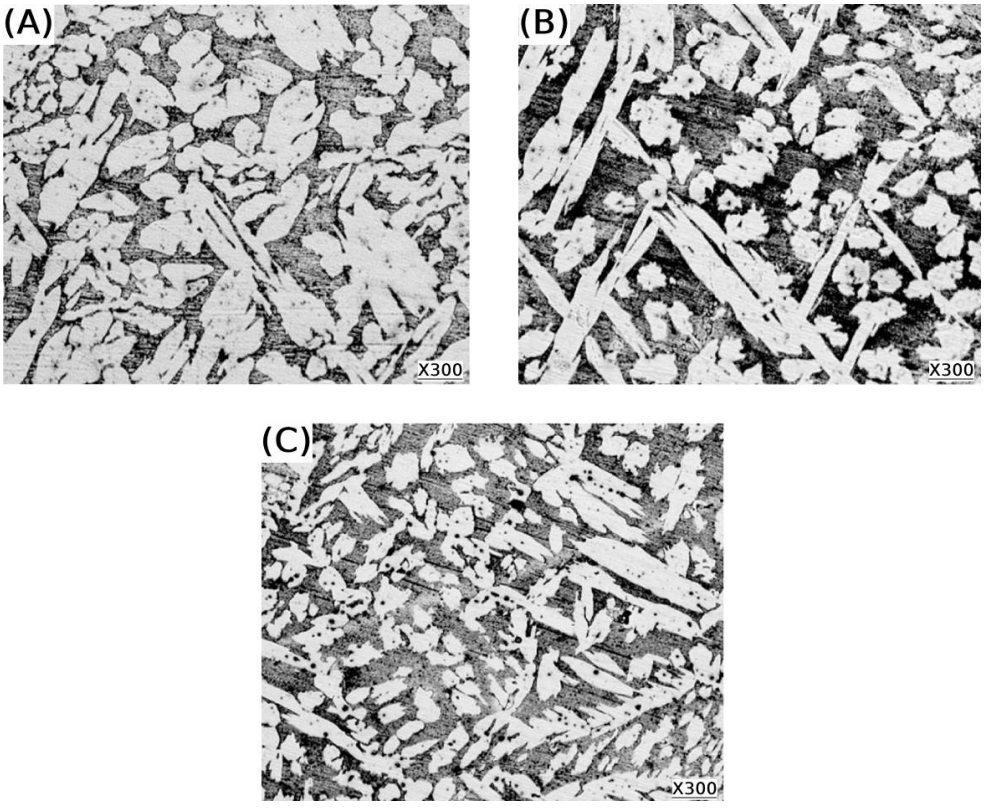

Fig. 3. Optical microscopy (OM) microstructures of CuZn40Pb2 billets produced by horizontal continuous casting at 300×: (a) B5 (pure charge), (b) B1 (fully recycled charge), and (c) B2 (mixed charge, 75% recycled + 25% pure). Light regions: α phase; darker regions: β phase. Small dark spots: Pb particles; larger dark spots: defects.

SEM/EDS analyses confirmed phase composition and lead patterns observed in optical microscopy. SEM images show the 100% recycled sample from vertical casting (B3) with elongated grains, segregation, inclusions, and coarse lead at grain boundaries

(Figure 4). The 25% pure material cast horizontally (B2) displays a uniform structure with well-distributed α and β phases, fine grains, and no defects, due to optimized processing (Figure 5). EDS results for the recycled sample show minor differences: the α phase has slightly more copper (62.1 wt%) than the β phase (58.3 wt%), indicating partial diffusion or incomplete transformation. Zinc in the β phase (~40–45 at%) is lower than expected, indicating uneven distribution. Bright lead precipitates are at grain boundaries or within phases. The 25% pure sample shows clearer phase separation: the α phase is enriched with copper (57.9 wt%), while the β phase has less copper (52.4 wt%).

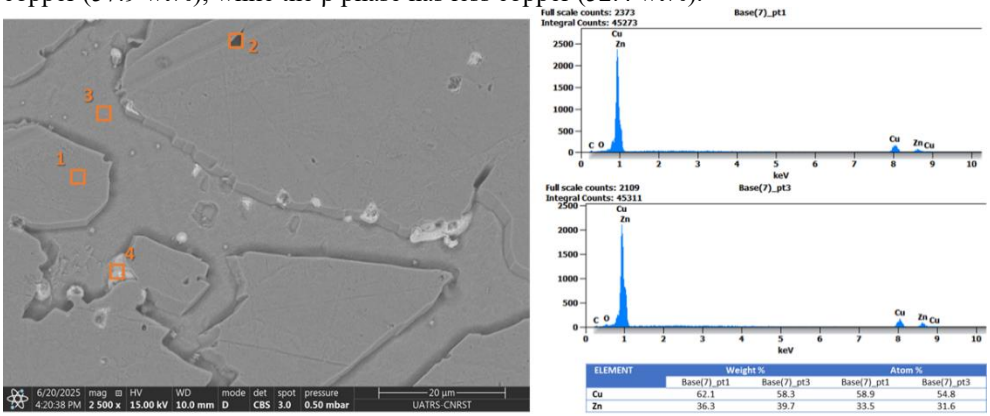

Fig. 4. SEM image of a leaded brass alloy sample (B3) accompanied by EDS analysis results for spectra (1 and 3).

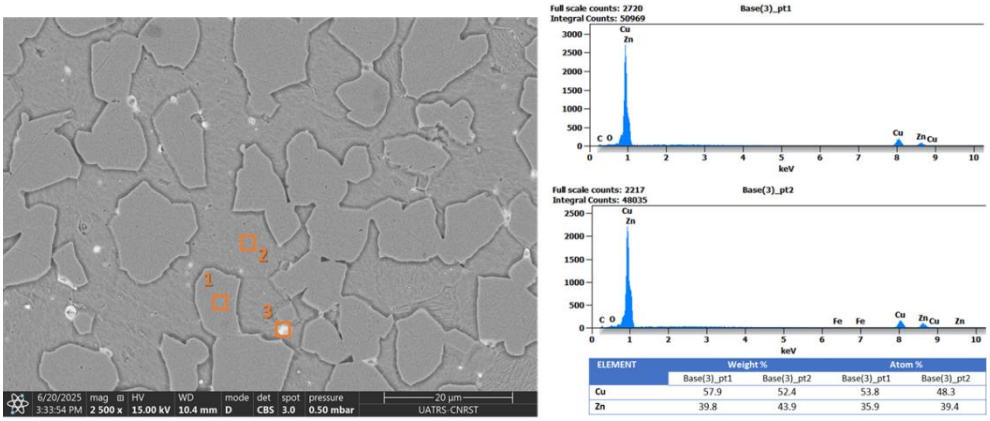

Fig. 5. SEM image of a leaded brass alloy sample (B2) accompanied by EDS analysis results for spectra (1 and 2).

3.3 Internal quality and non-destructive testing

Radiographic examination of the manufactured fittings confirms the microstructural observations. Parts produced under non-optimized conditions, especially those made from billets cast vertically from 100% recycled feedstock, sometimes display visible surface defects (Fig. 6). Conversely, fittings made from horizontally cast billets under optimized processing conditions, with a mixed charge consisting of 75% recycled materials and 25% virgin materials, show no visible defects. These results demonstrate that good control of the casting process and charge composition enhances internal strength and ensures industry-standard quality for sanitary fittings.

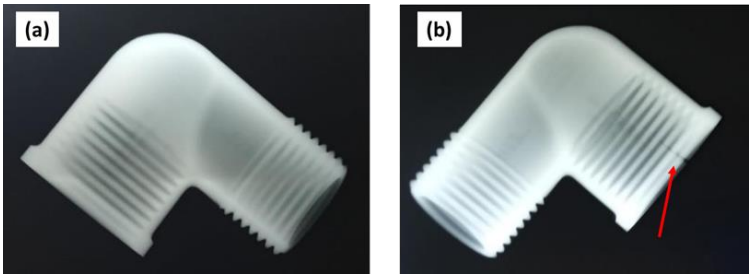

Fig. 6. Radiographic inspection of CuZn40Pb2 sanitary fittings: (a) fitting produced under optimized conditions, (b) fitting manufactured under non-optimized conditions, revealing internal defects

4 Conclusion

This research shows that high-quality CuZn40Pb2 sanitary fittings can be produced from partially recycled raw materials if the casting process and treatment parameters are properly controlled. Horizontal continuous casting with a mixed feedstock (75% recycled and 25% virgin) and adjustments to the process parameters improve chemical homogeneity, refine the microstructure, and achieve acceptable internal quality (comparable to that obtained with virgin materials) while minimizing defects in the final product. Notably, horizontally cast billets exhibited very low Pb segregation (relative differences about 0.41–0.56%), whereas vertically cast billets showed higher variations, reaching approximately 3.3–3.4%. These findings underscore the technical feasibility and industrial relevance of incorporating recycled brass into the manufacturing of sanitary fittings, offering an economical and sustainable solution aligned with resource efficiency goals, especially within the Moroccan industrial sector.

References

1. J. Choucri, F. Talhaoui, K. El Ganaoui, et al., Corrosion behavior and susceptibility to stress corrosion cracking of leaded brass alloys in simulated drinking water, Materials 15, 144 (2021). https://doi.org/10.3390/ma15010144
2. P. Jarvis, J. Fawell, Lead in drinking water – An ongoing public health concern?, Curr. Opin. Environ. Sci. Health 20, 100239 (2021). https://doi.org/10.1016/j.coesh.2021.100239
3. J. Johansson, P. Alm, R. M'Saoubi, P. Malmberg, J.-E. Ståhl, V. Bushlya, On the function of lead (Pb) in machining brass alloys, Int. J. Adv. Manuf. Technol. 120, 7263–7275 (2022). https://doi.org/10.1007/s00170-022-09205-0
4. S. Jasper, R. Subash, K. Muthuneelakandan, D. Vijayakumar, S. Jhansi Ida, The Mechanical Properties of Brass Alloys: A Review, Eng. Proc. 93, 11 (2025). https://doi.org/10.3390/engproc2025093011
5. H. Lee, I. Lee, X. Xu, T. Omori, R. Kainuma, Revisiting the phase equilibria in the Cu–Zn binary system, J. Phase Equilibria Diffus. 45, 304–317 (2024). https://doi.org/10.1007/s11669-023-01061-z
6. E. Mohsine, I. Touaiher, H. Oudghiri Hassani, S. Taibi, K. Azzaoui, Microstructural integrity of recycled CuZn40Pb2 brass in defect-free sanitary fittings: A process optimization approach, Moroccan J. Chem. 13, 1808–1824 (2025). https://doi.org/10.48317/IMIST.PRSM/morjchem-v13i4-59972

7. P. Stavroulakis, A. I. Toulfatzis, G. A. Pantazopoulos, A. S. Paipetis, Machinable leaded and eco-friendly brass alloys for high-performance manufacturing processes: A critical review, Metals 12, 246 (2022). https://doi.org/10.3390/met12020246
8. K. J. Al-Fadhalah, M. A. Rafeeq, N. Thomas, Microstructure and texture development in thermomechanically processed leaded brass, *Metals* **11**, 998 (2021). https://doi.org/10.3390/met11070998
9. J. Krawczyk, The role of lead in the machinability of copper alloys, Adv. Mater. Sci. 25, 1–12 (2025). https://doi.org/10.2478/adms-2025-0015
10. H. Y. Atay, G. Uslu, Y. Kahramaz, Ö. Atay, Investigations of microstructure and mechanical properties of brass alloys produced by sand casting at different casting temperatures, IOP Conf. Ser.: Mater. Sci. Eng. 726, 012018 (2020). https://doi.org/10.1088/1757-899X/726/1/012018
11. J. Y. Kim, J. E. Lee, M. S. Kim, Enhancing machinability in free-cutting duplex brass alloys: Isotropic blocky α phase formation via optimized hot extrusion processing, J. Alloys Compd. 1010, 177062 (2024). https://doi.org/10.1016/j.jallcom.2024.177062
12. L. Bertoletti, M. Gelfi, L. Girelli, A. Pola, Failure analysis of a hot stamped CuZn40Pb2 brass hydraulic component, Eng. Fail. Anal. 187, 110617 (2026). https://doi.org/10.1016/j.engfailanal.2026.110617
13. L. Huang, B. Peng, Q. Yue, G. Huang, C. Wang, R. Wang, N. Tian, First-principles study on the electrical and thermal conductivities of Cu–Zn binary alloys, Materials 18, 2310 (2025). https://doi.org/10.3390/ma18102310

Energy management of a brackish water reverse osmosis plant using time-of-use electricity tariffs

Yassine Elyaakouby[1,*], Amine Tilioua[1,*]

[1] Research Team in Thermal and Applied Thermodynamics (2.T.A.)
Department of Engineering Sciences, Faculty of Sciences and Techniques Errachidia, Moulay Ismaïl University of Meknès, B.P. 509, Boutalamine, Errachidia, Morocco.

Abstract: Reverse osmosis (RO) desalination has established itself as the main technology for obtaining drinking water in deserts and dry areas; nevertheless, it is still the most electricity-intensive consuming and energy-consuming operation of water purification processes. This study focuses on the demand-side energy management strategy that was applied in a fully operational brackish water RO desalination plant in southern Morocco to maximize the use of electrical energy according to time-of-use (TOU) electricity tariffs. Real-time data from the plant's actual operation were used for analysis to determine the interrelationship between electrical load demand (in kW), water production rate, and the various tariff periods. The development of a cost-oriented energy model enabled the evaluation of different operational scheduling scenarios that are based on high-load and low-load operating windows. The findings reveal that the operational scheduling of the RO process for production in reduced electrical demand periods not only decreases specific energy consumption and unit water production cost but also avoids the need for infrastructure expansion, renewable energy integration, or major process changes. renewable energy integration, or major process changes. The suggested approach for conducting TOU-based load management is a feasible, inexpensive, and simple to implement solution that could provide all reverse osmosis desalination plants with electrical energy efficiency and economic performance gains, particularly the ones situated in dry and poorly-off areas.

1. Introduction

Water scarcity constitutes a major challenge in arid and semi-arid regions, particularly in southern Morocco, where limited precipitation, climate variability, and increasing groundwater salinity significantly constrain access to potable water [1,2]. In this context, reverse osmosis (RO) desalination has emerged as a reliable and mature technology for brackish water treatment, owing to its high salt rejection efficiency and relatively moderate operating pressures compared with seawater desalination systems [3]. Nevertheless, despite these advantages, RO desalination remains highly energy-intensive. Electrical energy consumption—primarily associated with high-pressure pumping systems—often accounts for more than 40% of total operating costs in many installations [4,5]. From an electrical engineering standpoint, the expanding deployment of RO desalination plants introduces critical challenges related to power demand management, load variability, and energy cost optimization. Several recent studies have shown that the electrical load profile of RO plants exhibits strong temporal dependence, closely linked to operating schedules, process control strategies, and water demand patterns [6,7]. As a result, optimizing the interaction between desalination loads and the electrical grid has become a key area of research, particularly in regions simultaneously facing water scarcity and increasing pressure on grid capacity.

Energy reduction in reverse osmosis systems has mainly been achieved through technological improvements and among these, the development of high-performance membranes, energy recovery devices, and renewable energy such as solar and wind were mentioned as the main technological improvements [8–10]. The aforementioned

* Corresponding authors: y.elyaakouby@edu.umi.ac.ma , a.tilioua@umi.ac.ma

methods of reducing the energy footprint can lead to considerable energy savings but at the same time they require high capital investment, more complex systems, and long payback periods; thus, making them less feasible in areas having a shortage of resources. On the other hand, demand-side management (DSM)—a method used in smart grid applications and industrial energy systems—comes up as a cost-effective alternative by adjusting the electricity consumption pattern through the existing process equipment. Among the DSM measures, time-of-use (TOU) electricity tariffs reflect changes in grid demand and generation costs over time, making it easier for the utility to manage the load and thus, encourage the adoption of TOU tariffs for the purpose of load shifting and peak demand reduction in different parts of the world . A series of operations based on TOU have demonstrated considerable savings in the running costs of not only energy-intensive industrial processes but also water treatment and desalination plants . Nevertheless, the use of TOU-driven optimization is still insufficiently explored in full-scale brackish water reverse osmosis plants, particularly in North Africa and other arid regions.

Morocco's national electricity pricing system is designed in such a way that it includes time-of-use (TOU) tariffs, which not only encourage but also support the implementation of demand-side energy optimization strategies in industrial plants [11]. The case of TOU-based operational scheduling is being studied in the current research to not only lessen the cost of electricity but also to increase the energy efficiency of a large-scale brackish water reverse osmosis desalination plant in the southern part of Morocco. This study, which utilizes real operational data in conjunction with a cost-oriented energy optimization model, presents an approach that requires immediate deployment and low-cost investment, which is based on the principles of electrical engineering and demand-side energy management, thus playing a role in the development of more sustainable and less vulnerable desalination practices in dry areas.

2. Description of the RO plant and energy data

This section presents the characteristics of the study site and describes the electrical energy monitoring system used to collect operational data from the reverse osmosis desalination plant.

2.1 Study site and electrical energy monitoring

The investigated reverse osmosis (RO) desalination plant is located in the Zagora region, southern Morocco, an arid area characterized by limited freshwater resources and increasing groundwater salinity. The plant treats brackish groundwater with total dissolved solids (TDS) typically ranging between 3 and 5 $g \cdot L^{-1}$. Its nominal production capacity is approximately 5,000 $m^3 \cdot day^{-1}$, supplying potable water to local communities.

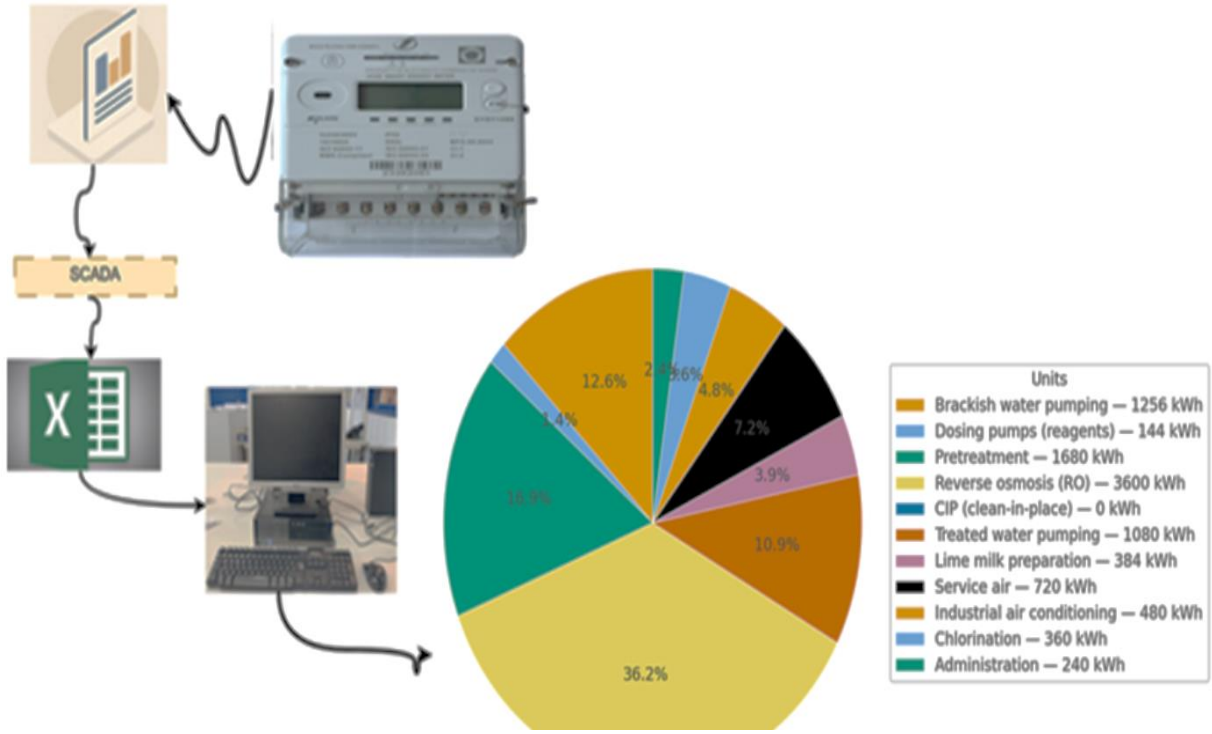

Fig. 1. Electrical energy consumption and Data oleion system in water reverse osmosis desalination plant.

From a viewpoint of electrical engineering, the plant is a major industrial load that is directly connected to the national power grid. Electrical energy consumption is not only monitored but also measured in real-time through smart energy meters that are a part of the plant's SCADA system. Thus, power demand (kW) and energy consumption (kWh) can be obtained on a real-time basis. The operational data are periodically exported and processed using data analysis tools to study consumption patterns and identify demand-side optimization opportunities. The total electrical energy consumption of the plant shown in **Fig.1.** is allocated to multiple subsystems like brackish water pumping, pretreatment units, high-pressure reverse osmosis pumps, clean-in-place (CIP) systems, and auxiliary services of chemical dosing, chlorination, and administration. The RO high-pressure pumping stage accounts for the majority of the electricity consumed, which means that any effort directed at this unit through electrical load management strategies will definitely result in savings, both in terms of energy and cost. Moreover, this detailed energy usage breakdown forms a strong ground for deploying time-of-use (TOU) tariff-based demand-side energy management practices, which are elaborated on in the subsequent sections.

2.2 Electrical energy system

The national electrical grid provides the desalination plant with power, and the plant's electrical energy consumption is being permanently monitored by means of industrial-grade energy meters, which are installed at the main power supply and integrated into the plant's SCADA system. The dataset that has been collected constitutes hourly and daily electrical energy consumption (kWh), water production volumes (m^3) corresponding to the consumption, and operating time distribution, which allows for a very detailed analysis of the electrical load profile of the plant. The pricing scheme of the electricity that is used at the facility is based on a time-of-use (TOU) tariff structure, defined by three different and distinct pricing periods: high-demand (peak) hours, intermediate-demand (normal) hours, and low-demand (super off-peak) night hours. The major pattern of pricing is shown in **Fig.2**, where the electricity prices are seen to have huge variations throughout the 24-hour cycle, which offers a very good economic reason for load shifting and demand-side energy management. The foundation for the operational scheduling and cost optimization strategy analyzed in this study is this tariff classification.

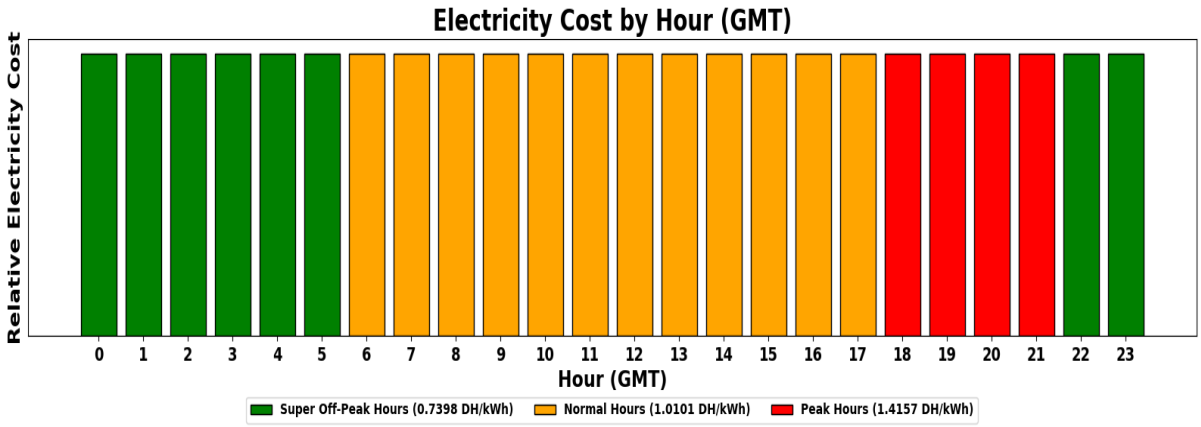

Fig. 2. Hourly electricity pricing profile under the time-of-use (TOU)

Research studies have examined energy efficiency methods for desalination plants yet they primarily concentrate on developing better membrane performance and energy recovery systems and systems for utilizing renewable energy (**Table 1**). Limited research has focused on operational scheduling methods which use electricity pricing systems that include time-of-use (TOU) tariffs.

Table 1 Electricity pricing systems for different studies..

Study	System / Plant Type	Optimization Approach	Reported SEC (kWh/m³)	Key Contribution
[12]	Seawater RO desalination	Energy recovery device optimization	3 – 4	Demonstrated energy reduction through improved pressure recovery
[10]	Large-scale desalination plants	Energy efficiency assessment	3 – 4.5	Identified energy-intensive stages and improvement opportunities
[13]	Industrial water treatment	Time-of-Use electricity optimization	1 – 2	Showed electricity tariff scheduling can reduce operating costs
[14]	Brackish water RO plants	Demand-side energy management	1 – 2	Demonstrated cost reduction using operational energy management
[15]	Desalination systems	Energy optimization strategies	2 – 4	Reviewed operational strategies for improving desalination efficiency
This study	Brackish water RO desalination plant (Morocco)	TOU-based operational scheduling using real operational data	0.95 – 1.30	Demonstrates energy optimization through operational scheduling using real plant data

3. Methodology

In this study, a time-of-use (TOU) electricity tariff-based scheduling strategy was applied to optimize the operation of the desalination plant. The approach aims to shift energy-intensive operations to periods with lower electricity tariffs while maintaining water production requirements.

The optimization approach consists of adjusting the operating schedule of the desalination plant according to the electricity tariff periods defined by the time-of-use pricing structure. The TOU tariff divides the day into different time periods characterized by varying electricity prices (peak, intermediate, and off-peak periods).

In the proposed scheduling strategy, energy-intensive operations are shifted as much as possible toward off-peak electricity periods while maintaining the required water production capacity of the plant. This operational adjustment allows the system to reduce energy costs without requiring major infrastructure modifications.

To evaluate the impact of the proposed strategy, two scenarios were analyzed:

- Baseline scenario: conventional plant operation without scheduling optimization
- Optimized scenario: plant operation adjusted according to the TOU electricity tariff periods

The comparison between these two scenarios allows the assessment of potential reductions in specific energy consumption and operational electricity costs.

3.1 Desalination plant description

The studied desalination plant is supplied with brackish groundwater extracted from ten boreholes located in ENNEBCH and TEHTAH, providing an average flow rate of approximately 250 $m^3 \cdot h^{-1}$. The raw water is collected in a 200 m^3 storage basin before entering the treatment process. Pretreatment includes pressurized sand filtration and pre-chlorination to remove suspended solids and control microbial growth. The water then passes through cartridge filters (5 µm) to protect the membranes as shown in **Fig.3.**

The desalination process is based on reverse osmosis (RO) technology, using high-pressure pumps to drive the saline water through semi-permeable membranes to remove dissolved salts. The system operates with two RO treatment lines, and the produced permeate undergoes post-treatment (remineralization and disinfection) before storage and distribution.

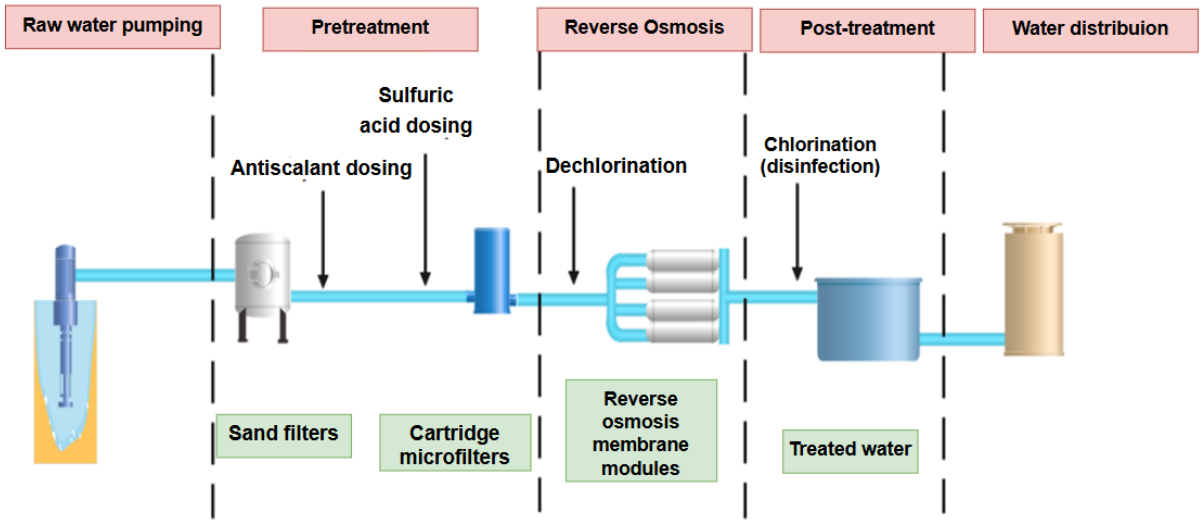

Fig.3. Desalination plant description Diagram

The main technical characteristics of the reverse osmosis desalination plant are summarized in **Table 2**. The system consists of two reverse osmosis trains operating in parallel and equipped with ESPA2-LD membranes designed for brackish water treatment. The plant operates with an average feed flow rate of approximately 125 $m^3 \cdot h^{-1}$ per train and a recovery rate of about 75%, resulting in a total production capacity of approximately 188 $m^3 \cdot h^{-1}$. Each train includes a multi-stage membrane configuration with several pressure vessels and spiral-wound membranes designed to ensure efficient salt rejection and stable hydraulic operation.

Table 2. Main characteristics of the reverse osmosis desalination plant

Parameter	Installed System
Membrane type	ESPA2-LD
Number of RO trains	2
Total production capacity	188 $m^3 \cdot h^{-1}$
Feed flow rate	125 $m^3 \cdot h^{-1}$
Permeate flow per train	94 $m^3 \cdot h^{-1}$
Recovery rate (%)	75 %
Number of pressure vessels per train	16
Number of membranes per pressure vessel	7
Total membranes per train	112
Number of vessels – stage 1	11
Number of vessels – stage 2	5
Operating pressure (RO)	~7.3 bar

3.2 Operational data collection

Operational data were collected from the plant's instrumentation sensors, including flow meters, pressure sensors, conductivity meters, and pH sensors installed throughout the desalination process. These measurements are continuously transmitted to the SCADA (Supervisory Control and Data Acquisition) system **Fig.4.**, where they are monitored and recorded in real time. The SCADA system stores the operational parameters in a central SQL database, from which the data were extracted and exported into CSV and XLSX formats for further processing, analysis, and evaluation of the plant's energy performance.

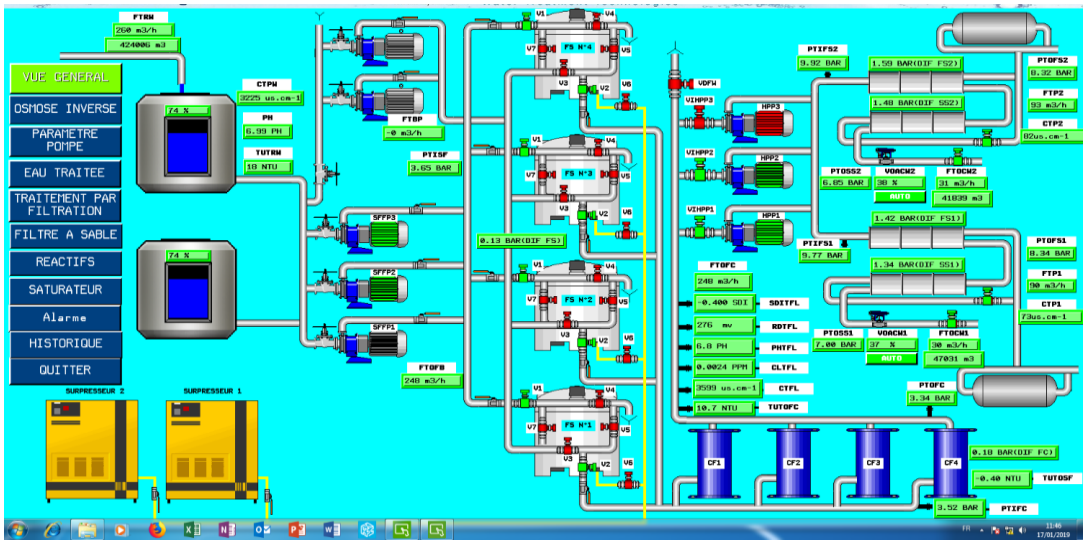

Fig.4. Desalination plant SCADA system.

3.3 Operational scheduling strategy

The operational optimization strategy was implemented based on the time-of-use (TOU) electricity tariff structure, which divides the daily electricity price into three periods: off-peak hours (low tariff), normal hours, and peak hours (high tariff), as illustrated in **Fig.5.** . The proposed approach prioritizes plant operation during off-peak periods (green) when electricity costs are lowest, followed by normal tariff hours (orange) when necessary, while peak tariff hours (red) are minimized to reduce energy costs.

The desalination plant is equipped with treated water storage reservoirs, which allow temporary storage of produced water during low-cost electricity periods. This stored water is then used to satisfy the municipal demand during peak consumption hours when electricity prices are highest. The scheduling strategy therefore shifts a larger fraction of water production toward low-tariff periods while maintaining sufficient storage capacity to ensure continuous water supply during high-demand periods.

This operational strategy represents a demand-side energy management approach requiring no additional infrastructure investment, as it relies only on adjusting the operating schedule of existing pumps and reverse osmosis units according to electricity tariff periods and storage capacity constraints.

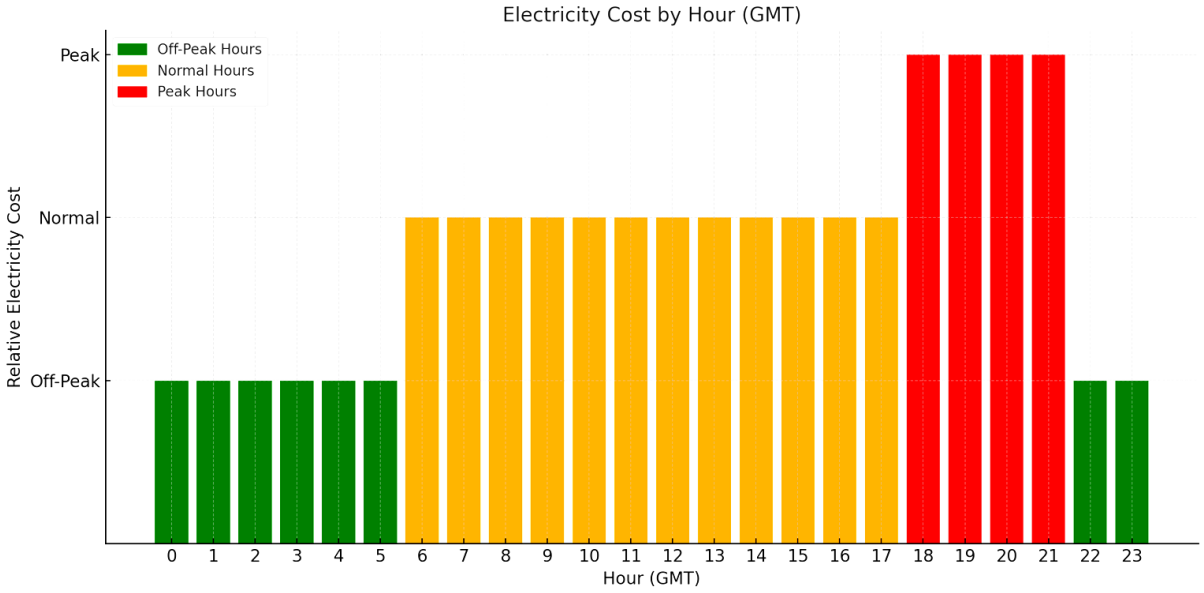

Fig.5. Daily electricity price: off-peak hours (low tariff), normal hours, and peak hours (high tariff)

The seasonal electricity tariff schedule used for the optimization analysis is summarized in **Table 3**, presenting the different time-of-use (TOU) periods and their corresponding electricity prices.

Table 3. Time-of-Use (TOU) electricity tariff structure used in the study **[15]**

Tariff Period	Winter Schedule	Summer Schedule	Cost (DH/kWh)	Cost ($/kWh)
Off-peak	5:00 pm – 11:00 pm	6:00 pm – 11:00 pm	1.4157	0.1416
Mid-period	7:00 am – 5:00 pm	7:00 am – 6:00 pm	1.0101	0.1010
Peak period	10:00 pm – 7:00 am	11:00 pm – 7:00 am	0.7398	0.0739

This figure (**fig.6**) illustrates an energy recovery device (ERD) used in reverse osmosis systems to improve energy efficiency.
High-pressure (HP) reject brine transfers its energy to the incoming low-pressure (LP) feed water, reducing pumping requirements.
As a result, the system significantly lowers energy consumption while maintaining effective desalination performance.

Fig.6. Energy recovery device

3.4 Energy–production relationship

The statistical analysis made use of real operational data collected from the desalination plant to determine water production effect on electric demand. A firm linear correlation was shown between daily electric energy consumption and water produced volume, thus confirming that reverse osmosis (RO) is the main process responsible for the electrical load in the plant. Specific energy consumption (SEC), which denotes the amount of electrical energy used to produce one cubic meter of desalinated water, was calculated using E**q. (1)**:

$$SEC = \frac{Econs}{Qprod} \quad \textbf{(1)}$$

where E_{cons} is the total electrical energy consumed (kWh), and Q_{prod} is the volume of produced water (m^3) corresponding to the total consumption.

This indicator is one of the most commonly used in electrical and energy engineering to evaluate the energy efficiency of desalination systems and to compare the pros and cons of different operating strategies.

3.5 TOU-based energy cost model :

A cost-oriented energy model was developed to analyze the effect of time-of-use (TOU) electricity tariffs on the price of desalinated water. The cost of unit water production connected to the power consumption was determined as follows **Eq. (2)**:

$$Cwater = \frac{\sum_t (Et\ x\ Tt)}{\sum Q} \quad \textbf{(2)}$$

where E_t is the electrical energy consumed during period t (kWh), T_t is the cost of electricity corresponding to period t (DH·kWh^{-1}), and $\sum Q$ is the total volume of produced water during the same time period (m^3).

This approach allows direct evaluation of how the shifting of loads around different tariff periods will impact the total energy cost of water production.

3.6 Operational scenarios

Three operational scenarios were evaluated to quantify the impact of time-of-use electricity tariffs on the energy and economic performance of the desalination plant.

- Baseline: Uninterrupted functioning without any tariff-based optimization.
- TOU-optimized: Higher output during periods with lower tariffs.
- Night-focused: Mainly production during night hours utilizing storage capacity.

4. Results and discussion

This section presents the analysis of the plant's operational performance and discusses the impact of the proposed optimization strategy on energy consumption and production cost.

4.1 Energy consumption analysis

The baseline operation exhibited an average specific energy consumption (SEC) of approximately 1.30 kWh•m^{-3}. Under the optimized operating scenario, the SEC decreased to about 0.95 kWh•m^{-3}. This improvement can be attributed primarily to the recovery and better utilization of the hydraulic energy contained in the reject stream, which contributes to improving the overall energy efficiency of the desalination system. Additionally, operating the plant under more stable conditions during low-demand periods improves pump performance and reduces hydraulic losses.

As shown in **Fig.7**, the reduction in SEC is particularly noticeable during off-peak and super off-peak periods, confirming the effectiveness of the proposed operational optimization strategy.

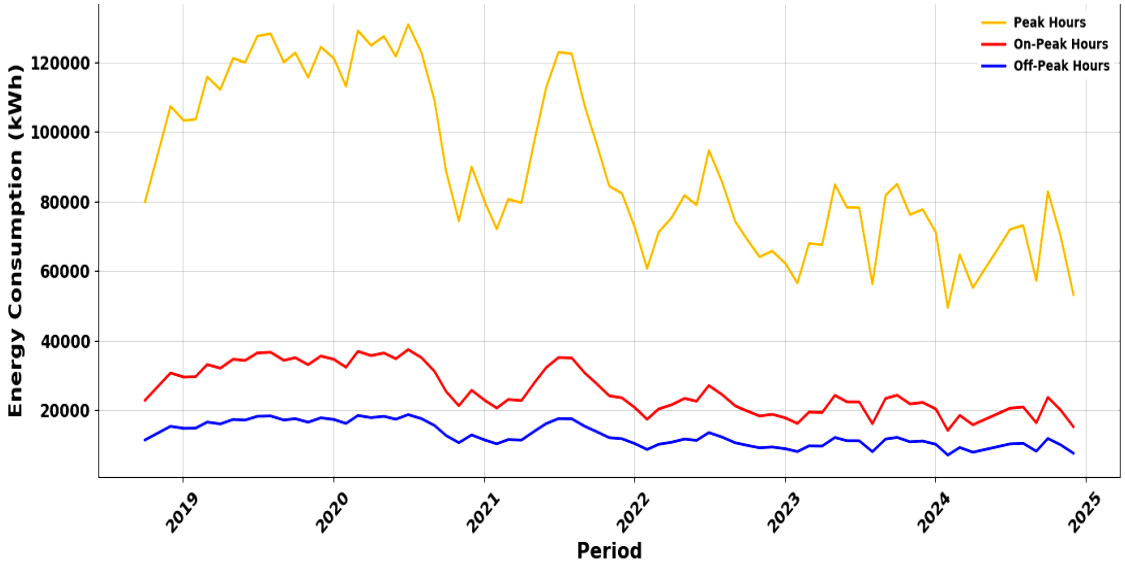

Fig. 7. Temporal variation of the specific energy consumption (SEC) of the reverse osmosis plant under baseline and time-of-use (TOU) optimized operating conditions.

4.2 Cost analysis

While the reduction in SEC (kWh•m^{-3}) is mainly related to improvements in hydraulic efficiency, the reduction in the production cost of water ($•m^{-3}) is primarily associated with the time-of-use (TOU) electricity tariff optimization. By shifting a larger fraction of water production toward off-peak electricity periods, the plant significantly reduces its electricity expenditure.

The electricity cost per cubic meter of produced water decreased from approximately 0.12 USD•m^{-3} under baseline operation to 0.076 USD•m^{-3} under the optimized TOU scenario, corresponding to a reduction of nearly 35%.

The influence of electricity tariff periods on water production cost is illustrated in **Fig. 8.** , where the TOU-optimized strategy consistently outperforms the baseline scenario.

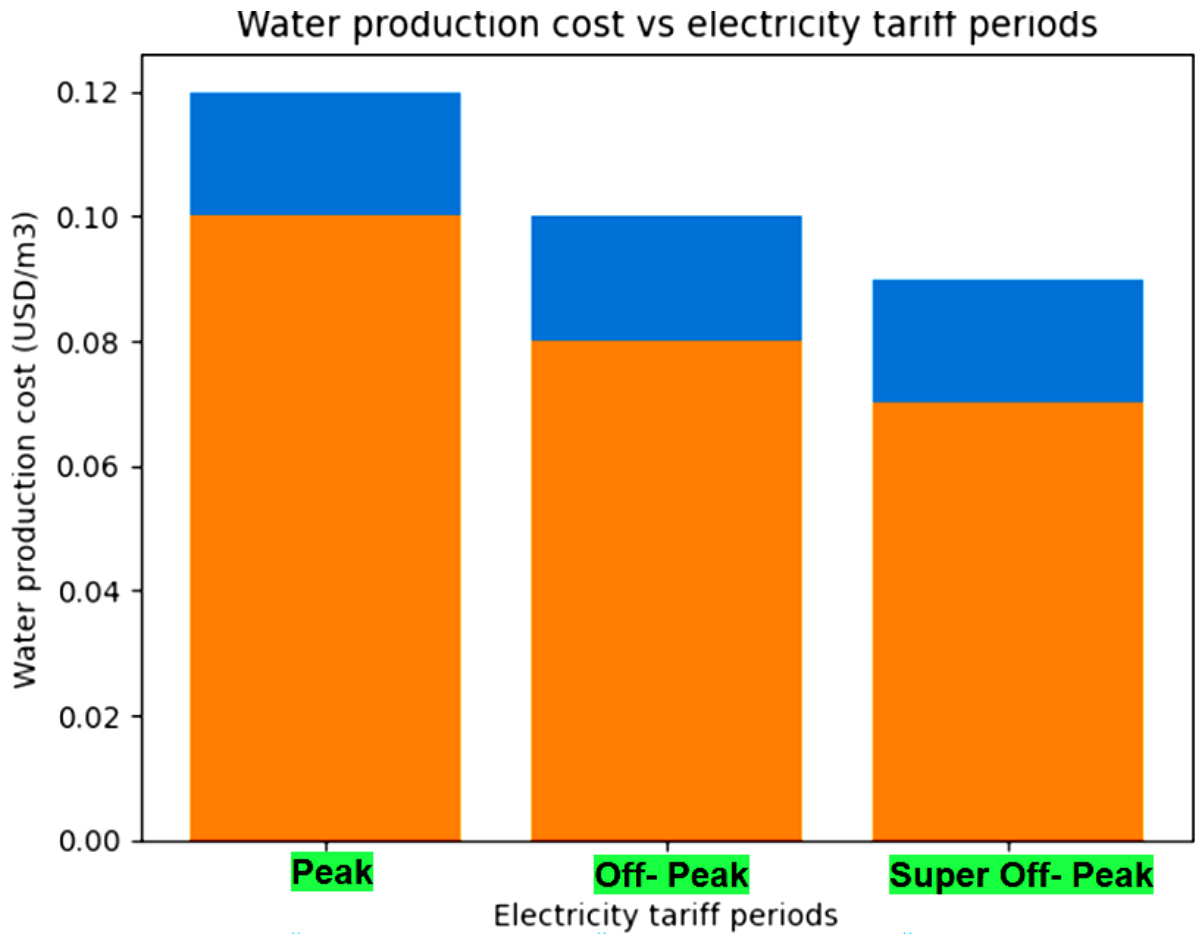

Fig. 8. Water production cost and TOU-optimized operating scenarios.

The graphic shows a progressive decline in the cost of water produced through the transition of operation from peak to off-peak and super off-peak tariff periods. The TOU-optimized strategy, when contrasted with baseline production, has a unit water cost that is considerably lower in all tariff windows, with maximum savings occurring in super off-peak hours. This proves the financial benefit of demand-side energy management in reverse osmosis desalination plants working with brackish water.

The findings support the idea that time-of-use (TOU)–based operational scheduling is an effective and economical way for reducing electrical energy costs in reverse osmosis desalination plants. In contrast to the integration of renewable energy that sometimes necessitates further capital outlay and higher system complexity, the proposed method relies exclusively on operational optimization. This method is particularly applicable to dry areas where different electricity rates have been established and where the current water storage capacity allows for enough operational flexibility. Additionally, the recommended technique can be easily applied in current RO plants without significant changes to the infrastructure or the addition of new equipment.

The obtained results are consistent with previous studies investigating energy optimization in reverse osmosis desalination systems. As summarized in **Table 1**, most studies report specific energy consumption values between 3–4.5 kWh•m^{-3} for seawater reverse osmosis systems when focusing on technological improvements such as energy recovery devices or process optimization. Other studies investigating demand-side

management or electricity tariff optimization strategies have reported lower SEC values, typically in the range of 1–2 kWh•m^{-3} for brackish water desalination systems. The results obtained in the present study, with SEC values ranging from 0.95 to 1.30 kWh•m^{-3}, are therefore consistent with the lower range reported in the literature for brackish water reverse osmosis plants. This confirms that operational optimization strategies, particularly those based on time-of-use electricity tariffs, can significantly improve the overall energy performance of desalination plants without requiring major infrastructure modifications.

5. Conclusion

This study shows that modifying reverse osmosis plant operation according to the time-of-use electricity tariffs will not only result in a significant increase in energy efficiency but also cut down the overall cost of water production. The TOU-based optimization strategy provides a simple, low-cost, and rapidly implementable solution for enhancing the economic performance of brackish water RO desalination plants, especially in dry areas where the electricity tariffs shift during the day. This proximity to the operational scheduling instead of the infrastructure upgrade gives the solution a strong scalability and transferability. The future investigation will be directed towards the extension of this framework by means of automated SCADA-based control, the projection of demand management, and the use of renewable energy thereby improving system flexibility and sustainability.

Authors Contribution

Yassine ELYAAKOUBY conducted the data analysis, developed the energy optimization model, and prepared the manuscript. Amine TILIOUA supervised the research, contributed to the conceptual framework, and reviewed the manuscript.

Funding

This research received no external funding.

Data Availability Statement

The operational data used in this study were obtained from the investigated reverse osmosis desalination plant. Data are available from the authors upon reasonable request.

Conflicts of Interest

The authors declare no conflict of interest.

Acknowledgements

The authors would like to thank the staff of the Department of Engineering Sciences, Faculty of Sciences and Techniques Errachidia, Moulay Ismaïl University of Meknès, and the staff of the investigated desalination plant for providing access to operational data and technical information used in this study.

References

[1] Intergovernmental Panel on Climate Change (IPCC), Climate Change 2023: Impacts, Adaptation and Vulnerability, Cambridge University Press (2023). https://doi.org/10.1017/9781009325844

[2] N. Ghaffour, T.M. Missimer, G.L. Amy, Desalination and water reuse to address global water scarcity, Water Research 190, 116646 (2021). https://doi.org/10.1016/j.watres.2020.116646

[3] Y. Kim, G. Lee, J. Byun, S. Lim, S. Lee, Y.G. Park, Optimizing energy efficiency in desalination: Performance evaluation of seawater reverse osmosis and pressure retarded osmosis hybrid systems, Desalination 601, 118557 (2025). https://doi.org/10.1016/j.desal.2025.118557

[4] H. Nassrullah, S.F. Anis, R. Hashaikeh, N. Hilal, Energy for desalination: A state-of-the-art review, Desalination 491, 114569 (2020). https://doi.org/10.1016/j.desal.2020.114569

[5] A. Toopshekan, H. Yousefi, F.R. Astaraei, Technical, economic, and performance analysis of a hybrid energy system using a novel dispatch strategy, Energy 214, 118850 (2020). https://doi.org/10.1016/j.energy.2020.118850

[6] Z. Wu, X. Zhao, Y. Mao, R. Liu, Flexibility quantification of desalination plants for demand response: An adaptive robust optimization methodology, Applied Energy 355, 123835 (2024). https://doi.org/10.1016/j.apenergy.2024.123835

[7] J. Schallenberg-Rodríguez, B. Del Rio-Gamero, N. Melian-Martel, T.L. Alecio, J. González Herrera, Energy supply of a large size desalination plant using wave energy. Practical case: North of Gran Canaria, Applied Energy 278, 115681 (2020). https://doi.org/10.1016/j.apenergy.2020.115681

[8] B. Tashtoush, W. Alyahya, M. Al Ghadi, J. Al-Omari, T. Morosuk, Renewable energy integration in water desalination: State-of-the-art review and comparative analysis, Applied Energy 340, 121950 (2023). https://doi.org/10.1016/j.apenergy.2023.121950

[9] D. Janowitz, A. Margane, S. Yüce, T. Wintgens, Photovoltaics powered seawater desalination by reverse osmosis and water conveyance benefits the green energy transition in the Middle East, Desalination 602, 118646 (2025). https://doi.org/10.1016/j.desal.2025.118646

[10] N. Ghaffour, T.M. Missimer, G.L. Amy, Technical review and evaluation of the economics of water desalination: Current and future challenges for better water supply sustainability, Desalination 522, 115434 (2022). https://doi.org/10.1016/j.desal.2021.115434

[11] Y. Elyaakouby, A. Tilioua, Energy optimization of reverse osmosis desalination systems in arid regions: A case study in Morocco, Desalination and Water Treatment 325, 101637 (2026). https://doi.org/10.1016/j.dwt.2026.101637

[12] A. Alhaj, S. Al-Ghamdi, M. Ali, Energy efficiency improvements in seawater reverse osmosis desalination systems, Desalination 509, 115065 (2021). https://doi.org/10.1016/j.desal.2021.115065

[13] Y. Zhang, H. Wang, J. Liu, Optimization of industrial energy consumption using time-of-use electricity tariffs, Energy 239, 122101 (2022). https://doi.org/10.1016/j.energy.2021.122101

[14] X. Li, J. Zhao, P. Wang, Demand-side energy management strategies for industrial water treatment plants, Applied Energy 335, 120745 (2023). https://doi.org/10.1016/j.apenergy.2023.120745

[15] M. Al-Nasser, A. Al-Sarkhi, Energy optimization approaches in desalination plants: A review, Desalination 568, 116012 (2024). https://doi.org/10.1016/j.desal.2023.116012

Assessment of the impact of drought on water resources in the Gharb plain: approach using the Support Vector Regression (SVR)

Driss El Karfa[1]*, Adnane Al Karkouri[2], Jamal Al Karkouri[1] , Mouhcine Batchi[1], Hommane Boudine[2], and Hind Fattah[3]

[1]Ibn Tofail University, Faculty of Human and Social Sciences, Laboratory of Territories, Environment and Development, Kénitra, Morocco
[2]Ibn Tofail University, Faculty of Sciences, Kénitra, Morocco
[3]Mohamed V University, Faculty of Letters and Human Sciences, Society, History and Heritage Laboratories, Rabat, Morocco

Abstract: The Gharb plain is one of Morocco's most fertile agricultural regions, as it is located in the lower part of the Sebou basin at a low altitude. This study combines the Standardized Precipitation–Evapotranspiration Index (SPEI) for identifying drought events, correlation analysis to assess their relationship with flow, and the support vector regression (SVR) model for hydrological modeling and prediction. The results reveal a strong relationship between drought and river flow. The SPEI-12 index shows the best performance, with a coefficient of determination ($R^2 = 0.91$) and a root mean square error (RMSE = 62.39), while SPEI-6 also exhibits a significant relationship ($R^2 \approx 0.79$). All models demonstrate very high statistical significance ($P < 10^{-18}$), confirming the ability of the SPEI index to explain flow variability in the study area.

1 Introduction

Global warming, primarily driven by increased greenhouse gas emissions (carbon dioxide, nitrous oxide, and methane) from human activities [1], has direct and indirect effects on agri-food systems. Changing and unpredictable temperatures and precipitation, as well as an increase in extreme weather events (droughts, floods, pest and disease outbreaks), threaten our ability to ensure global food security, eliminate poverty, and achieve sustainable development [2].

In addition, climate change will undermine food security in 11 West African countries, namely Benin, Burkina Faso, Côte d'Ivoire, Ghana, Guinea, Liberia, Niger, Nigeria, Senegal, Sierra Leone, and Togo. It also examines how climate change will necessitate intensified efforts to achieve sustainable food security throughout the region [3].

* Corresponding Author: driss.elkarfa@uit.ac.ma

In all Mediterranean countries located in semi-arid subtropical zones, rainfall is the dominant climatic parameter, being generally insufficient on the one hand, and much more variable than temperature on the other. Generally speaking, climate change will lead to shifts in climate zones and changes in rainfall patterns [4]. Furthermore, in recent decades, prolonged dry spells have become a reality in these countries, particularly in Morocco [5].

Morocco has experienced a significant increase in drought over the past few decades, accompanied by a general trend toward aridification, indicating that resource capacity is declining due to a succession of dry years, as most available water resources for agriculture are already being utilized: 75% in Morocco (2007) [6].

The Gharb plain is renowned for its agricultural significance, owing to its location in the Sabou basin, which receives most of the basin's surface water, covering an area of approximately 40,000 km² (Oued Sebou Basin Agency).

In addition, runoff at the mouth of the Sebou River is substantial due to the plain's low elevation and its predominantly agricultural use. This situation makes irrigation essential, particularly given the increasing frequency and severity of drought years [7]. This raises the issue of using hydrological runoff-based drought prediction models in the Gharb plain.

The objective of this study is to apply the most effective model to predict monthly streamflow using the Standardized Precipitation–Evapotranspiration Index (SPEI) in the Gharb Plain, thereby improving water resources management.

2 Study area

As shown in Figure 1, (Oued Sebou Basin Agency) the Gharb Plain is characterized by low elevations, as it has functioned as a subsidence basin since the Miocene, filled with alluvial deposits from the Sebou River and its tributaries, such as the Ouargha. This filling process was so rapid that the current topography of almost the entire plain was shaped in recent times (Middle and Recent Quaternary) before the Sebou River finally found its way to the Atlantic Ocean at the extreme southwestern end of the plain. Therefore, the Gharb refers to the plain of the lower Sebou River and the surrounding highlands. This plain offers a wide variety of landscapes. For example, the north of upper Gharb consists of Miocene marl hills; the east is clearly dominated by the pre-Rif folds of Jbel Outita; the boundary of the south is less marked, with the plain sinking beneath the sandy Villafranchian plateau of Mamora; finally, the west is isolated from the Atlantic Ocean by a string of consolidated Quaternary dunes.

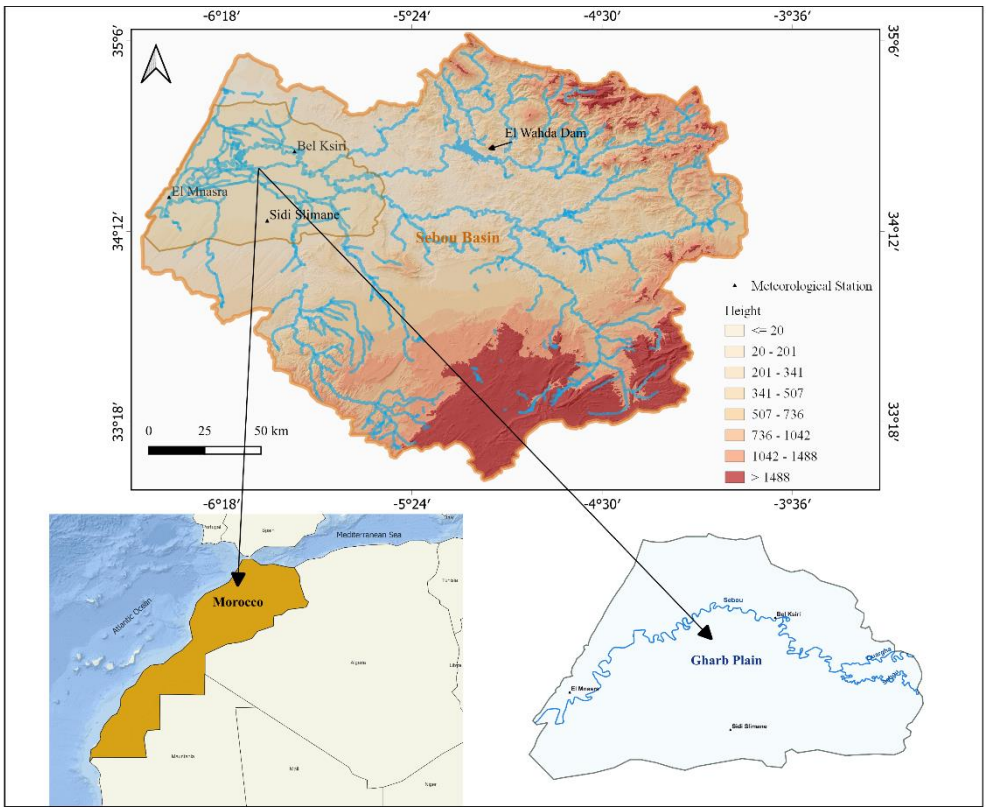

Fig 1. Localisation study area with GIS based in digital elevation model.

3 Data and Methods

3.1 *Data*

Two national institutions provided the data that were used in this study. The Regional Office for Agricultural Development of the Gharb (ORMVAG) provided precipitation and temperature data, while the Sebou River Basin Agency (ABHS) provided monthly flow data.

3.2 *Methods*

The Standardized Precipitation–Evapotranspiration Index (SPEI) was calculated for the periods 1987–2020 in Sidi Slimane and Bel Ksiri stations, and 1987–2019 in El Mnasra station. These three stations were well chosen because they represent the entire plain. The formula proposed by Thornthwaite in 1948 is simple because it depends only on the temperature that is chosen to calculate the SPEI.

Support Vector Regression (SVR) models are based on the principle of minimizing structural risk, whereas classical neural networks minimize empirical risk [8]. As a result, SVR models focus on reducing generalization errors rather than learning errors. Details on the development of SVR models are available in [9]. All SVR models in this study were

developed using the Online SVR software [10], which is designed to build support vector machines for regression tasks.

The data was divided into two sets: 80% for model training and 20% for validation. Before training, the variables were normalized using the StandardScaler method to avoid biases that are related to scale differences. The SVR model was trained with a basic radial basis function (RBF) kernel and the main parameters (C = 10, gamma = "scale," epsilon = 0.1). The model's performance was evaluated using several statistical indicators, including the coefficient of determination (R^2), root mean square error (RMSE), and Nash–Sutcliffe efficiency (NSE). In addition, Pearson's correlation coefficient and the associated p-value were calculated to assess the statistical significance of the predictions.

$$R^2 = 1 - \frac{\sum_{i=1}^{n}[y_i(i) - x_i(i)]^2}{\sum_{i=1}^{n}[x_i(i) - \bar{X}_i]^2} \qquad (1)$$

The RMSE (Root Mean Square Error) is calculated from the observed values and then averaged for all simulations that are made with the different models. It measures the difference between the simulation and the observations.

$$RMSE = \sqrt{\frac{1}{n} \sum_{i=1}^{n} (y_i - x_i)^2} \qquad (2)$$

R-squared (or coefficient of determination) is a statistical metric used to evaluate the quality of a model's fit to observed data.

$$R^2 = 1 - \left(\frac{SSres}{SStot}\right) \qquad (3)$$

Nash-Sutcliffe efficiency (NSE) is a statistical indicator used to evaluate the ability of a hydrological model to reproduce observed data by comparing the accuracy of the model to that of the average of the observations [11].

4 Results

4.1 *The Standardized Precipitation–Evapotranspiration Index (SPEI) in the study area*

As shown in Figure 2 (Ministry of Agriculture, Marine Fisheries, Rural Development, and Water and Forests; Gharb Regional Office for Agricultural Development, Kenitra 2021), the SPEI changes over time, often shifting from a wet period to a dry period in the short and medium term (SPEI-3 and SPEI-6), while the SPEI-12 indicates longer periods of drought.

Figure 3 (Ministry of Agriculture, Marine Fisheries, Rural Development, and Water and Forests; Gharb Regional Office for Agricultural Development, Kenitra 2021) shows greater variability in drought conditions, with episodes of severe and extreme drought, particularly at the SPEI-12 scale. This confirms an intensification of drought over the long term.

Figure 4 (Ministry of Agriculture, Marine Fisheries, Rural Development, and Water and Forests; Gharb Regional Office for Agricultural Development, Kenitra 2021) illustrates this trend: short-term droughts (SPEI-3) are common but short-lived, while long-term drought (SPEI-12) are less frequent but more persistent.

Figures 2, 3, and 4 show an overall consistency in the temporal variability of drought. Interannual variability is strongly indicated by the SPEI-3 and SPEI-6 indicators, while prolonged drought episodes are highlighted by the SPEI-12, particularly during certain recent periods.

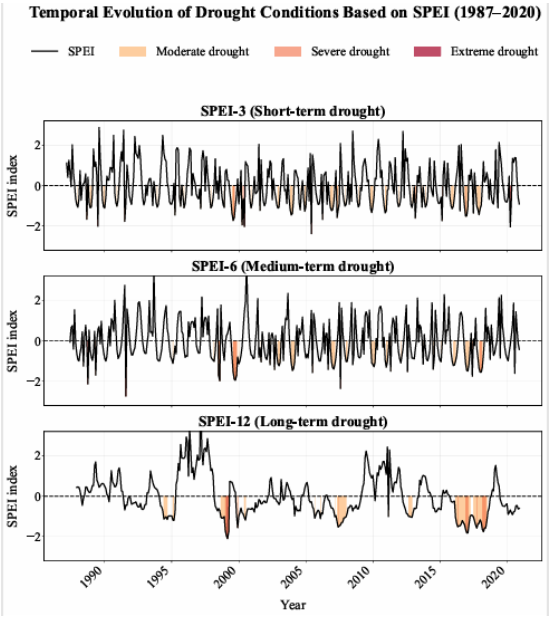

Fig 2. Monthly SPEI values in Bel Ksiri.

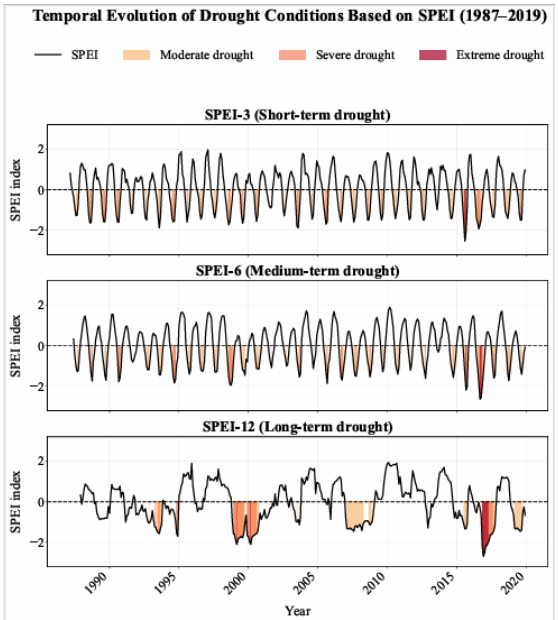

Fig 3. Monthly SPEI values in El Mnesra.

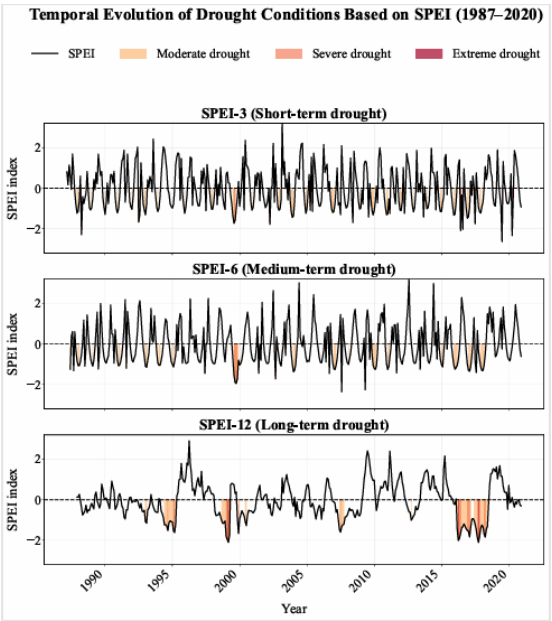

Fig 4. Monthly SPEI values in Sidi Sliman.

4.2 *Forecasting and prediction*

Figure 5 illustrates the effectiveness of the SVR model using the SPEI-3, SPEI-6, and SPEI-12 indicators. The model generally reproduces the observed flows, with accuracy improving as the time scale increases. Discrepancies are visible during peaks for SPEI-3, while SPEI-6 shows improvement and SPEI-12 provides the best measurement. To improve predictions, it is essential to take long-term climate signals into account.

Figure 6 shows that the accuracy of the SVR model improves significantly as the temporal scale of the SPEI index increases. While SPEI-3 struggles to capture the magnitude of flood peaks, SPEI-6 stabilizes the forecasts by reducing seasonal variations. The SPEI-12 allows observed flows to be fitted with the highest accuracy, demonstrating the robustness of long-term climate signals for modeling. This scaling highlights the importance of the basin's hydrological memory in its response to precipitation variations.

Figure 7 shows that the performance of the SVR model is closely linked to the temporal scale of the SPEI index, with optimal accuracy for SPEI-12. SPEI-3 exhibits instability during sudden changes, while SPEI-6 improves overall consistency, although it struggles to capture extreme peaks. The SPEI-12 stands out for its near-perfect synchronization with observed discharge data, enabling it to effectively capture high- and low-water dynamics. Hydrological predictions can be made more reliable by accounting for cumulative climate anomalies over one year.

The support vector regression (SVR) model, used for forecasting, is based on lagged flow data and other drought indicators, enabling accurate simulation of future flows, as clearly illustrated by the results presented in Tables 1, 2, and 3.

Statistical indicators confirm this reliability: the high coefficient of determination (R^2) reflects the model's ability to capture the variability in the data, while the low values of the root mean square error (RMSE) indicate a small margin of error. Furthermore, the Nash-Sutcliffe efficiency (NSE) values validate the quality of the predictions relative to the average of the observations, thereby confirming the model's robustness for water resource management in the Gharb Plain.

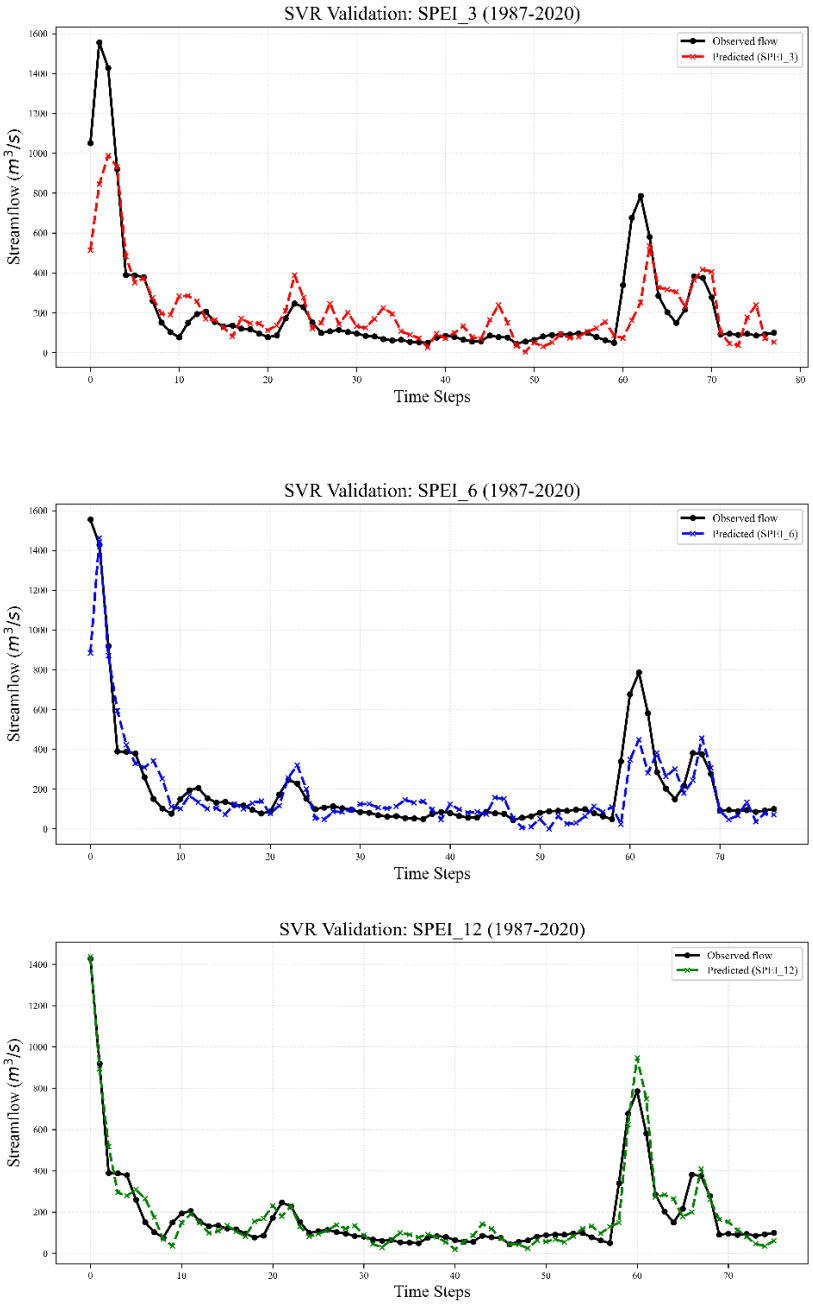

Fig 5. Comparison between observed and predicted flow using the SVR model based on the SPEI-3, 6, and 12 indices at Bel Ksiri.

Table 1. Evaluation of the performance of the SVR model for forecasting flows in the Gharb plain based on SPEI indices at different time scales in Bel Ksiri

indicator	R2	P-Value	RMSE	NSE
SPEI_3	0,68079675	$1{,}58812\ 10^{-22}$	159,4377688	0,68079675
SPEI_6	0,78764953	$1{,}69027\ 10^{-27}$	123,1273859	0,78764953
SPEI_12	0,918658202	$1{,}9703243\ 10^{-43}$	62,38689694	0,918658202

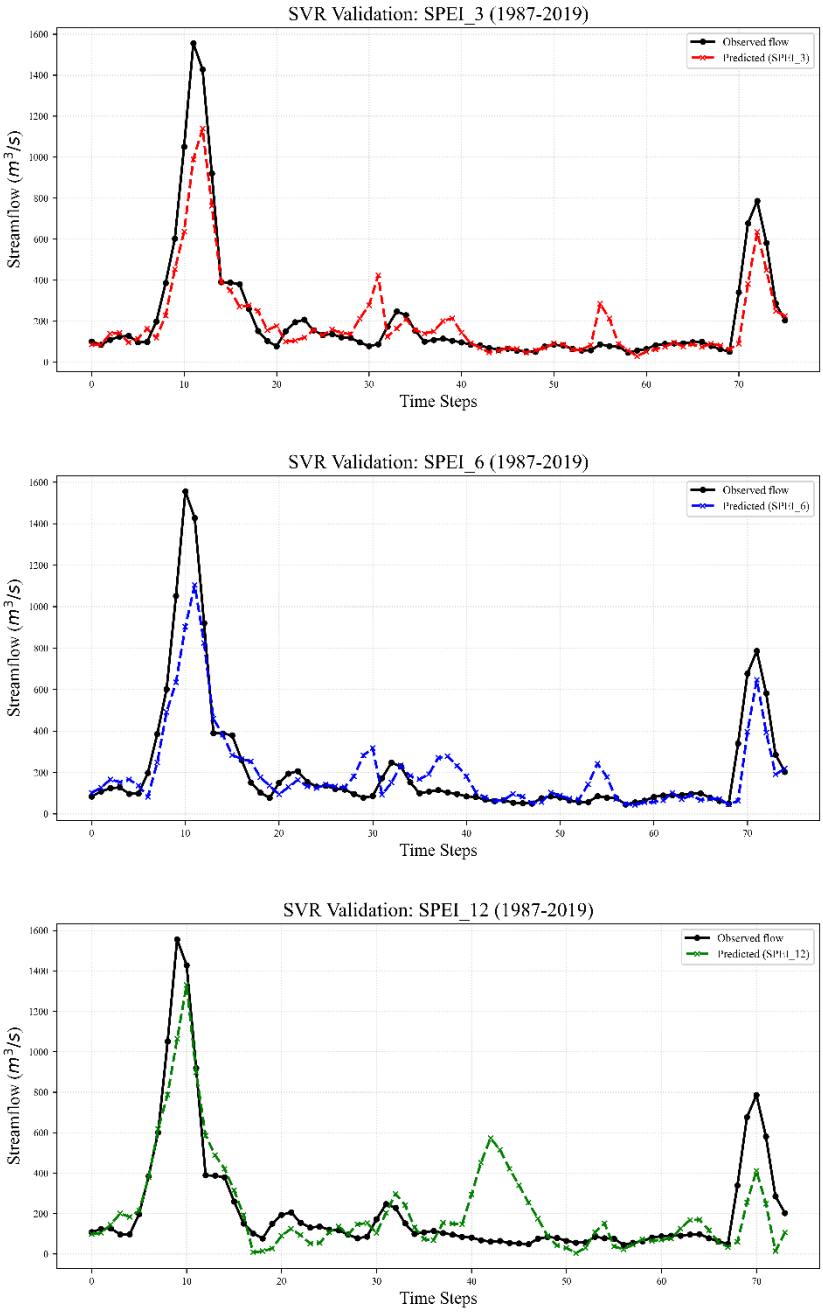

Fig 6. Comparison between observed and predicted flow using the SVR model based on the SPEI-3, 6, and 12 indices at El Mnesra.

Table 2. Evaluation of the performance of the SVR model for forecasting flows in the Gharb plain based on SPEI indices at different time scales in El Mnesra

Indicator	R2	P-Value	RMSE	NSE
SPEI_3	0,813934084	$6{,}64488\ 10^{-35}$	124,3008197	0,813934084
SPEI_6	0,794595762	$2{,}20527\ 10^{-32}$	131,3266682	0,794595762
SPEI_12	0,674415335	$3{,}04648\ 10^{-19}$	166,2170066	0,674415335

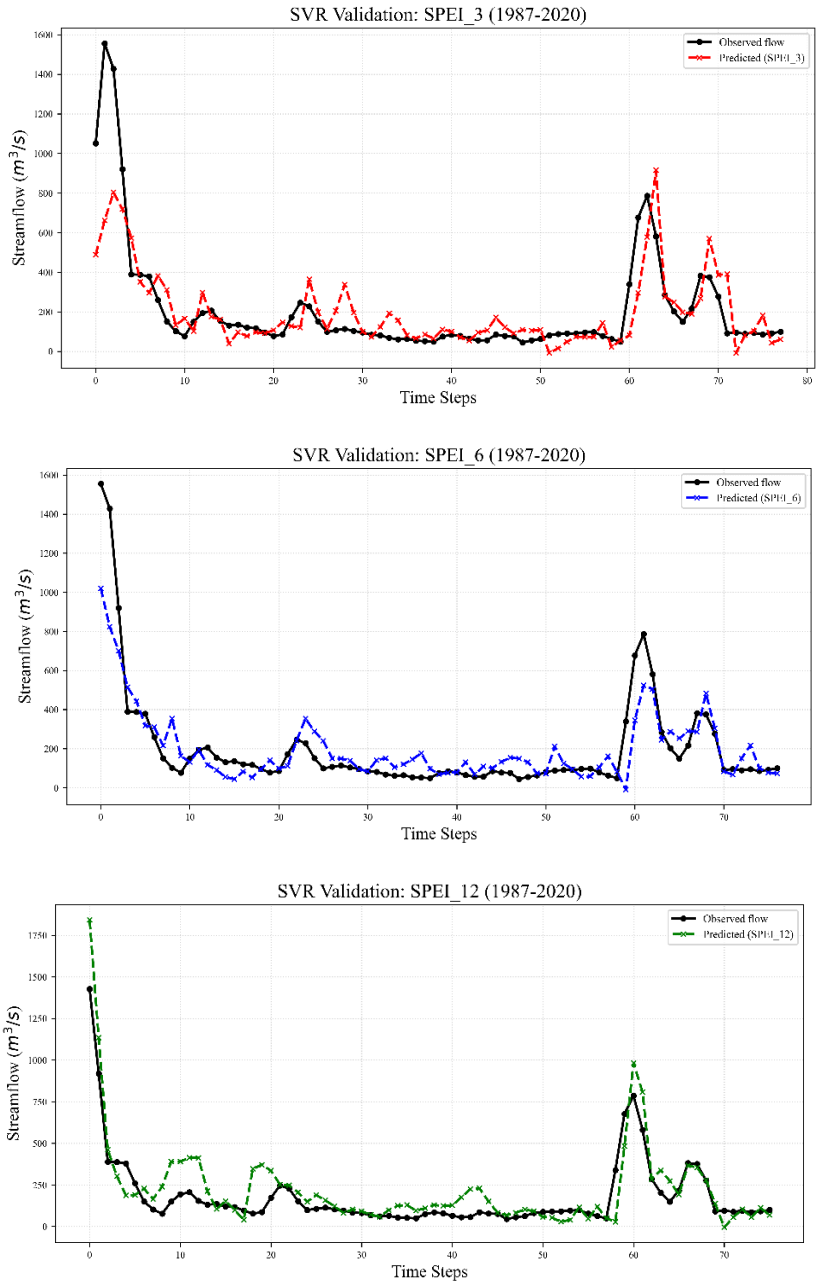

Fig 7. Comparison between observed and predicted flow using the SVR model based on the SPEI-3, 6, and 12 indices at Sidi Slimane.

Table 3. Evaluation of the performance of the SVR model for forecasting flows in the Gharb plain based on SPEI indices at different time scales in Sidi Slimane

Indicator	R2	P-Value	RMSE	NSE
SPEI_3	0,613969805	$3{,}32\ 10^{-18}$	175,334829	0,613969805
SPEI_6	0,74917273	$4{,}04\ 10^{-28}$	133,8182733	0,74917273
SPEI_12	0,695961572	$3{,}32\ 10^{-31}$	120,6148388	0,695961572

5 . Discussion

The precipitation index directly influences the availability of water resources, which in turn determines the condition of vegetation cover. Extreme droughts severely disrupt the water balance due to the combined effects of increased evapotranspiration and persistent moisture deficits [12]. Figures 2, 3, and 4 display that droughts are recurring in the study area, which will have a significant impact on the hydrological regime of the Gharb plain. Figures 5, 6, and 7 show that the model used (SVR) has a high capacity for predicting flow. In this context, the integration of these dynamics into the SVR model has demonstrated a strong predictive capacity for flows. The obtained results are very satisfactory, as the model used in this study has clearly demonstrated its ability to predict flow rates during periods of drought, particularly using the SPEI-12 index. This index depicts the best performance, with a coefficient of determination ($R^2 = 0.91$) and a root mean square error (RMSE = 62.39). Furthermore, the model exhibits very high statistical significance ($P < 10^{-18}$) for all the indices considered. However, the short duration of the time series limited the model's ability to make predictions outside the calibration conditions. Despite this, the SVR model's predictive capability demonstrated remarkable accuracy in hydrological studies. A similar study was conducted in the Rheraya basin, one of the sub-basins of the Tensift basin, where this model also demonstrated superior predictive capability compared to the Random Forest model [13].

Consequently, the reliability of this model (SVR) enables various stakeholders in water management to address this issue using rigorous scientific criteria, thereby facilitating the forecasting of water resource conditions and ensuring their proper management and sustainability in semi-arid environments, where droughts are frequent.

6 . Conclusion

The use of the SVR model in predicting monthly flow via SPEI-3, SPEI-6, and SPEI-12 demonstrates its performance across various validation measures. This work is an important resource for decision-makers who are responsible for water resource management in the Sebou basin in general and in the Gharb plain in particular.

The methodology adopted in this study makes it possible to propose effective solutions for water resource management in the Sebou basin in the context of climate change, and encourages all stakeholders to use cutting-edge technologies aimed at preserving these resources.Therefore, it is recommended to favor crops that consume little water and are resistant to drought, a recurring phenomenon in the area studied.

The scientific rigor of the results obtained allows them to be quantified and generalized. Indeed, the processing of data from official sources, combined with the use of a machine learning model, guarantees the reliability of the conclusions and their applicability to similar contexts.

References

1. M. Filonchyk, M. P. Peterson, L. Zhang, V. Hurynovich, Y. He, Greenhouse gases emissions and global climate change: Examining the influence of CO2, CH4, and N2O. Sci. Total Environ. 935, 173359 (2024).
https://doi.org/10.1016/j.scitotenv.2024.173359.
2. T. Begna, R. B. Wakweya, Mitigating climate change impacts on food security via climate-smart agriculture. Plant Stress 101152 (2025). https://doi.org/10.1016/j.stress.2025.101152
3. M. Thomson, C. R. Pattison, A. Agrawal, J. T. Erbaugh, H. K. Friedrich, S. R. Heinz, L. S. Gutierrez Hernandez, The climate change and conflict nexus in West Africa: A new approach for operationally relevant vulnerability assessments (2023).
4. P. Tarín-Carrasco, D. Petrova, L. Chica-Castells, J. Lukovic, X. Rodó, I. Cvijanovic, Assessment of future precipitation changes in Mediterranean climate regions from CMIP6 ensemble. EGUsphere, 2024, 1-34 (2024).
https://doi.org/10.5194/egusphere-2023-3057
5. A. Chaqdid, A. Tuel, A. El Fatimy, N. El Moçayd, Extreme Rainfall Events in Morocco: Spatial Dependence and Climate Drivers. Weather Clim. Extrem. 40, 100556 (2023). https://doi.org/10.1016/j.wace.2023.100556
6. V. Gumus, N. El Moçayd, M. Seker, M. Seaid, Future projection of droughts in Morocco and potential impact on agriculture. J. Environ. Manage. 367, 122019 (2024). https://doi.org/10.1016/j.jenvman.2024.122019
7. D. El Karfa, J. Al Karkouri, M. Batchi, H. Boudine, Assessing the influence of the Al Wahda dam commissioning on flood flows and low water levels in the Gharb plain, Morocco. J. Geogr. Inst. Jovan Cvijic SASA 74, 273–280 (2024). https://doi.org/10.2298/ijgi240122010e
8. S. Bour, Z. Kayhomayoon, F. Hassani, S. Ghordoyee Milan, O. Bazrafshan, R. Berndtsson, Enhancement of standardized precipitation evapotranspiration index predictions by machine learning based on regression and soft computing for Iran's arid and hyper–arid region. *PLoS One* **20**(3), e0319678 (2025). https://doi.org/10.1371/journal.pone.0319678
9. G. Moges, K. McDonnell, M. A. Delele, A. N. Ali, S. W. Fanta, Development and comparative analysis of ANN and SVR-based models with conventional regression models for predicting spray drift. Environ. Sci. Pollut. Res. 30, 21927–21944 (2023). https://doi.org/10.1007/s11356-022-23571-y
10. F. Rezaie, M. Panahi, S. M. Bateni, C. Jun, C. M. Neale, S. Lee, Novel hybrid models by coupling support vector regression (SVR) with meta-heuristic algorithms (WOA and GWO) for flood susceptibility mapping. Nat. Hazards 114, 1247–1283 (2022). https://doi.org/10.1007/s11069-022-05424-6
11. S. Sadkou, Level Finder–Prévision des crues par intelligence artificielle (réseaux de neurones) pour la mise en œuvre de plans d'intervention graduée et la gestion de crise à l'échelle (inter) communale. Ph.D. thesis, IMT Mines Alès (2024).
12. D. El Karfa, J. A. Karkouri, M. Batchi, H. Boudine, Assessing the influence of flow variability on irrigated agriculture in the Central Gharb Plain, Morocco. J. Glob. Innov. Agric. Sci. 11, 507–513 (2023).
https://doi.org/10.22194/JGIAS/23.1210
13. B. Bargam, A. Boudhar, C. Kinnard, H. Bouamri, K. Nifa, A. Chehbouni, Evaluation of the support vector regression (SVR) and the random forest (RF) models accuracy for streamflow prediction under a data-scarce basin in Morocco. Discover Appl. Sci. 6, 306 (2024).
https://doi.org/10.1007/s42452-024-05994-z

Flow in a Channel with a Second-Order Fluid Under Transverse Flow Conditions

Mustapha Lamine[1], *Jamila Bouchgl*[2,3] and *Ahmed Hifdi*[1]

[1] Laboratory of Mechanics and High Energy Physics, Faculty of Sciences Aïn-Chock, Hassan II University of Casablanca, P.O. Box 5366 Maarif Casablanca 20100, Morocco.
[2] Higher Institute of Marine Fisheries-Agadir
[3] Laboratory of energy Engineering, Materials and Systems, ENSA, Ibn Zoher University, Agadir Morocco

Abstract. We examine the linear stability of a second-order fluid flow between two parallel, porous plates, with uniform transverse flow. An analytical approach was developed to obtain the base solution for stationary flows of a slightly viscoelastic fluid, which was then perturbed around the equilibrium state. The governing problem is formulated as a modified Orr–Sommerfeld equation and solved numerically using the Chebyshev collocation technique. Our numerical code was validated by reproducing classical results for a Newtonian fluid, with a critical Reynolds number Rec = 5772.22 and critical wave number α_c = 1.021 when transverse flow is absent. We then studied the influence of transverse injection, expressed by the injection Reynolds number R_c. For R_c = 0.2, 0.4, and 0.6, the flow shows increasing stabilization, with critical Reynolds numbers rising accordingly. When fluid elasticity is included, with K = -10^{-4}, the growth rate of the most unstable mode decreases by roughly 15%, delaying the onset of instability. At high R_c, elasticity and transverse flow combine to shift the flow to more stable regimes, highlighting how even slight viscoelasticity can significantly modify the transition to instability. These results provide a clearer understanding of how transverse flow and fluid elasticity interact to influence channel flow stability, with potential applications in polymer processing, filtration, and porous media flows.

1 Introduction

The stability of fluid flow in channel configurations has long been a subject of interest in fluid mechanics because of its importance in many practical applications, including heat transfer, filtration processes, polymer transport, and flows in porous structures. Predicting the transition from stable to unstable flow is essential for understanding transport mechanisms and improving the performance of engineering systems. For this reason, the effects of cross-flow, porous media [1,2], slip boundary conditions, and fluid properties on flow stability have been widely investigated.

Viscoelastic fluids, which exhibit both viscous and elastic behavior, can significantly alter flow characteristics compared to Newtonian fluids, particularly by influencing the onset of

instabilities. Although previous studies have examined the flow of Newtonian and some viscoelastic fluids, the understanding of the combined effects of transverse injection and fluid elasticity in porous channels remains limited.
The influence of uniform cross-flow and thermal effects on channel flow stability has been examined in several studies. Khan and Sani in [3] investigated the Poiseuille–Rayleigh–Bénard instability in a channel flow with uniform cross-flow and thermal slip, and showed that thermal boundary conditions play an important role in determining the stability limits. Shankar and Shivakumara [4] studied the hydrodynamic stability of plane porous-Couette flow with vertical throughflow and found that wall permeability significantly modifies the critical conditions for instability. The combined effects of porous media and slip boundary conditions were later analyzed by Badday and Harfash [5], who reported that both permeability and slip at the boundaries influence the behavior of Poiseuille flow.
More recent work has extended these investigations to complex fluid models. The authors in [6] showed that, viscoelastic effects can alter the onset of instability. Shivaraj Kumar and Basavaraj [7,8] examined the stability with uniform vertical cross-flow using different analytical approaches, providing further understanding of the mechanisms governing flow transition. The effect of more complex porous structures was considered by Hajool and Harfash [9], who studied instability in Poiseuille flow through a porous medium and highlighted the influence of the porous matrix on stability behavior.

The role of non-Newtonian fluid properties has also attracted considerable attention. A.S.Varghese and S. Panda [10] investigated the instability of a second-grade fluid and demonstrated the importance of fluid elasticity in modifying flow characteristics. In the context of viscoelastic fluids, Lamine et *al*. [11] carried out, in a plane channel, a linear stability analysis of flow and later examined the influence of uniform wall suction and blowing on the stability of a viscoelastic liquid [12]. Their results showed that elastic effects and wall mass transfer have a significant impact on the critical stability parameters.
Despite the progress achieved in these studies, the interaction between cross-flow, porous effects, slip conditions, and fluid elasticity is still not fully understood. A detailed analysis of these combined effects is necessary to improve the theoretical description of channel flow stability and to better understand transition mechanisms in complex fluids.

In this study, we take a different approach from that of previous studies to perform a linear stability analysis of flow with second-order fluid, between two porous and parallel plates. We highlight the effects of the transverse jet (at high flow rates) and the elastic properties of the fluid on the critical marginal stability threshold. This allows us to offer a new perspective on the stability of this flow.

2 Problem Formulation

We consider the Poiseuille flow, in the cartesian coordinate system (**x**, **y**), of a viscoelastic fluid between two parallel and porous plates. The plates are separated by $2d$ and extending infinitely in the **x** direction. A uniform transverse injection with velocity $v_0 = C^{te}$ is applied at **y**= +d corresponding to the upper wall, while suction *occurs* at the same velocity v_0 at $\boldsymbol{y} = -d$ corresponding to the lower wall.
The equations modelling the problem are:

$$\rho\left(\frac{\partial \boldsymbol{V}^*}{\partial t} + \boldsymbol{V}^*.\boldsymbol{\nabla}\boldsymbol{V}^*\right) = -\boldsymbol{\nabla}P^* + \boldsymbol{\nabla}\boldsymbol{\tau}^* \quad (1)$$

$$div\,\mathbf{V}^* = 0 \quad (2)$$

$\boldsymbol{V}^*$ represent the velocity field and P^* is the pressure. $\boldsymbol{\tau}^*$ is the stress tensor, defined for a second-order fluid:

$$\boldsymbol{\tau}^* = \mu\mathbf{A}_1 + \alpha_1\mathbf{A}_2 + \alpha_2\mathbf{A}_1^2 \;;\quad \alpha_1 < 0 \; et \; \alpha_2 \leq 0 \tag{3}$$

with

$$\mathbf{A}_1 = \nabla\mathbf{V}^* + (\nabla\mathbf{V}^*)^T \tag{4}$$

$$\mathbf{A}_2 = \frac{\partial\mathbf{A}_1}{\partial t^*} + (\mathbf{V}^*.\nabla\mathbf{A}_1) + \mathbf{A}_1.\nabla\mathbf{V}^* + (\nabla\mathbf{V}^*)^T.\mathbf{A}_1 \tag{5}$$

the strain rate tensors are $\boldsymbol{A}_1$ and $\boldsymbol{A}_2$, μ represent the dynamic viscosity, α_1 represents the viscosity jump and α_2 indicates the elasticity of the fluid.

2.1 Base flow solutions

Taking into account the translational invariance of the velocity in the longitudinal direction, the velocity field in the continuity equation simplifies in the equilibrium state to:

$$V^* = \left(U^*(y^*), v_o, 0\right) \tag{6}$$

with:

$$U^*(y^* = \pm d) = 0 \tag{7}$$

Substituting equations (3)–(6) into (1), corresponding to the Navier-Stokes equations, leads to the equation that governs the fluid's motion in the equilibrium state:

$$KR_c d\frac{\partial^3 U^*}{\partial y^{*3}} - \frac{\partial^2 U^*}{\partial y^{*2}} - \frac{R_c}{d}\frac{\partial^2 U^*}{\partial y^*} = \frac{\partial P^*}{\partial x^*} \tag{8}$$

Where $K = \frac{\alpha_2}{\rho d^2}$ and $R_c = \frac{\rho\, v_0 d}{\mu}$ represent the elasticity number and the Reynolds number of injection, respectively. For solving the problem in this case, given by equation (8), requires three boundary conditions. To close the problem, in addition to the two boundary conditions (7), an approximation is made regarding the nature of the fluid by assuming it is slightly viscoelastic [4], i.e., the elasticity number is small compared to unity. Using this approach, equation (8) becomes:

$$-\frac{\partial^2 U^*}{\partial y^{*2}} - \frac{R_c}{d}\frac{\partial U^*}{\partial y^*} = \frac{\partial P^*}{\partial x^*} \tag{9}$$

Using the reference quantities: d for length, $\frac{d}{U^*_{\max}}$ for time, $U^*_{\max}$ for velocity and $\rho U^{*2}_{\max}$ for pressure as follows:

$$y = \frac{y^*}{d}, x = \frac{x^*}{d}, t = \frac{U^*_{max}\, t^*}{d}, V = \frac{V^*}{U^*_{max}} = \left(\frac{U^*}{U^*_{max}}, \frac{v_0}{U^*_{max}}\right), P = \frac{P^*}{\rho(U^*_{max})^2}$$

The solution of the problem (9) in dimensionless variables is:

$$U(y) = R_c \frac{y + sinh^{-1}(R_c) - e^{-R_c y} - \coth(R_c)}{1 - \log\left(R_c^{-1} sinh(R_c)\right) - R_c \coth(R_c)} \tag{10}$$

In the case of $R_c \to 0$, corresponding to a transverse flow, we recover the classic form of the Poiseuille profile corresponding to (1-y^2).

2.2 Linear Stability Analysis

Two-dimensional infinitesimal disturbances (v, p) are superimposed on the equilibrium flow. Then, the solutions are sought in normal modes as follows using the theorem of Squire:

$$(v,p) = [\varphi(y), P']e^{i(\alpha x - \alpha ct)}\ ;\quad i^2 = -1 \qquad (11)$$

Where c is the propagation velocity, α is the wave number in the x-direction, φ and p' are the complex amplitudes of the stream function $\psi(x, y, t)$ and the disturbance p', respectively. This leads us to establish a differential equation that determines the stability of this flow, expressed as:

$$i\alpha\,\mathrm{Re}\left[(U-c)(D^2-\alpha)^2 - D^2U\right]\varphi - (D^2-\alpha^2)^2\varphi =$$
$$Rc(D^3 - \alpha^2 D^1)\varphi + i\alpha\,\mathrm{Re}\,K\left[(U-c)(D^2-\alpha)^2 - D^4U\right]\varphi \qquad (12)$$

In the case where R_c = 0, the second term of equation (12) accounts for the effect of elasticity, K. The boundary conditions associated with this equation are as follows:

$$\varphi(\pm 1) = D^1\varphi(\pm 1) = 0,\ avec\quad D^j = \frac{\partial^j}{\partial y^j}\quad j = 1,2,3,4 \qquad (13)$$

2.2.1 Numerical Method

Using the Chebyshev spectral collocation method [11], the equations (12) and (13) are solved numerically. In this approach, discretizing our system (12) and (13) at the Gauss-Lobatto collocation points (N) reduces the problem to a system below with eigenvalues c:

$$\mathbf{E}\varphi = c\mathbf{F}\varphi \qquad (14)$$

Note that **E** and **F** denote the matrices dependent on α, K, R_c and Re. Furthermore, to validate our computational code, we first verify the results obtained for a Newtonian fluid in the literature. In the second step, we check the results for a non-Newtonian fluid in the previous studies. For K=0 (Newtonian fluid), and without transverse flow, R_c=0: we compute the 32 least stable even and odd eigenvalues for the fundamental mode ($\alpha = 1$, *Re*=10000). We found a good agreement between our results and those obtained previously. Additionally, we accurately determined the stability thresholds for the flow of a Newtonian fluid (R_c=0 et *K*=0): Re_c= 5772.221 et α_c=1.02056. In the presence of transverse flow ($R_c \neq 0$), we compared our results with those of Fransson and Alfredsson [3]. Table1 summarizes this validation.

Table 1: Critical stability thresholds when K=0.

	Our results		Results in [9]	
R_c	Re_c	α_c	Re_c	α_c
0	5772.221	1.0205	5772.22	1.0205
0,2	5966.799	1.0132	5967,01	1,0118
0,4	6607.263	0.9913	6607,4	0,9902
0,6	7902.204	0.9551	7902,5	0,9536

As shown in this table, the critical stability thresholds obtained in our computations are in excellent agreement with those reported in [9]. The absolute differences in the critical Reynolds numbers (Rec) and wave numbers (αc) are very small on the order of 0.001–0.3 for Re_c and 0.001–0.0015 for α_c highlighting the accuracy of our numerical method and the reliability of the results.

For $K\neq0$, corresponding to a non-Newtonian fluid, and without a transverse flow (R_c=0), our results are in a good agreement with those of the previous studies. This comparison is shown in Table 2.

Table 2: Critical stability thresholds when R_c=0.

	Our results		Previous studies	
K	Re_c	α_c	Re_c	α_c
0	5772.221	1.02056	5772	1.0195
-0.00001	5638.376	1.0267	5639	1.0240
-0.00005	5167.848	1.0501	5168	1.0475
-0.0001	4698.682	1.0770	4698	1.0750
-0.0002	4014.524	1.1250	4014	1.1215

In this study, we assume a slightly viscoelastic fluid (K << 1) to simplify the analysis and obtain a tractable analytical solution. This assumption is physically justified because, in many industrial applications such as polymer transport or flow through porous media, elastic effects are small but not negligible. The primary influence of elasticity on flow stability can thus be captured without introducing the full complexity of strongly viscoelastic behavior. Additionally, the boundary conditions chosen uniform injection at the upper wall and uniform suction at the lower wall reflect practical situations where transverse flow can be controlled, such as in filtration or channelized flow systems. These conditions also facilitate the analytical and numerical treatment of the problem while preserving the main physical mechanisms governing the flow.

3 Results and Discussion

In the (Re_c, α_c) plane, the marginal stability curves for R_c = 0.2, 0.4 and 0.6, with the elasticity number fixed at K= - 10^{-5} and K= - 10^{-4}, are plotted in Figures 1 and 2, respectively. These curves indicate that increasing values of R_c are associated with a gradual stabilization of the flow. Therefore, the pair (Re_c, α_c) takes intermediate values between those observed when one of the control parameters (R_c et K) is present and the other is absent.
At specific values of Re_c = 6000 and α_c = 1, we qualitatively illustrate in Figure (3) the impact of increasing R_c on the amplitude of the imaginary part c_i of the most unstable eigenvalue, while fixing the elasticity number at K = 0, -10^{-5},-5.10^{-5},-10^{-4} et -2.10^{-4}.

From figure 3, we observe that when K=0, an increase in R_c causes the initially least stable mode to stabilize and then regain stability at higher values of R_c. The amplitude of the unstable mode increases with K for a given value of R_c *t*aking into account the elastic behavior of the fluid.

At large values of this parameter, elasticity reduces the amplitude of this unstable mode. Furthermore, the variation of R_c maintains the same shape of c_i as observed in the case of a

Newtonian fluid. However, the stabilization observed at high values of R_c is more prominent in the elastic fluid than in the Newtonian fluid.

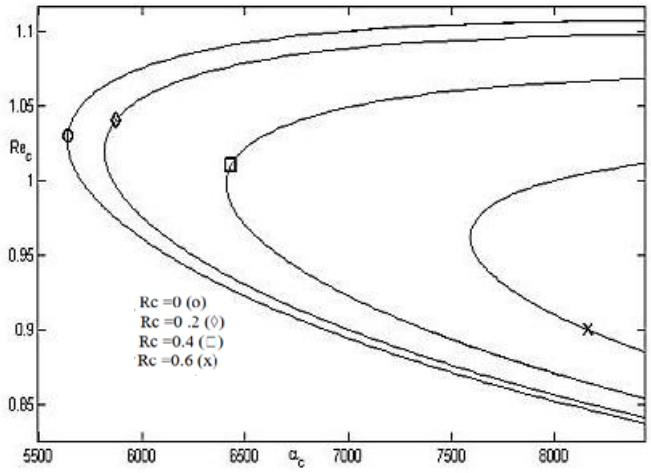

Fig. 1. Marginal stability curves at K=-10^{-5} [6] for different injection Reynolds number.

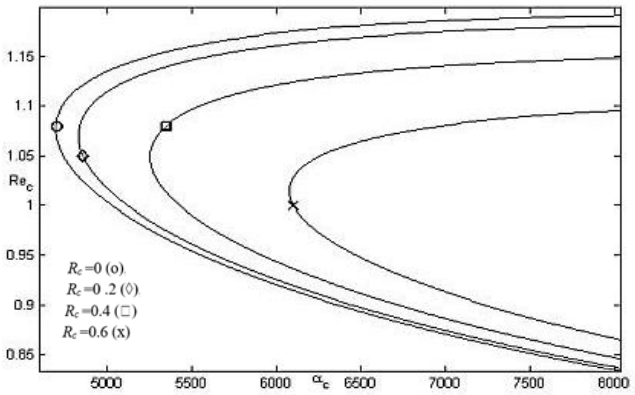

Fig. 2. Marginal stability curves at K=-10^{-4} [6] for different injection Reynolds number.

The table 3 bellow shows how the elasticity of the fluid (K) and the transverse flow (Rc) influence the stability of the channel flow. When the fluid becomes more elastic (K more negative), the critical Reynolds number decreases, meaning the flow becomes unstable more easily. When a transverse flow is applied (Rc > 0), the critical Reynolds number increases, indicating that the flow is more stable. This gives a clear, quantitative view of the effects of these two parameters on flow stability.

The observed trends show that increasing the transverse injection Rc stabilizes the flow by suppressing the growth of the least stable modes, while increasing fluid elasticity K tends to either stabilize or destabilize the flow depending on its magnitude. Specifically, for small negative values of K, the amplitude of the most unstable mode decreases, delaying the onset of instability, whereas at higher elasticity, the interaction with Rc produces more complex behavior. This analysis links the numerical results directly to the physical

processes governing the flow, providing a more robust qualitative and quantitative understanding of the system.

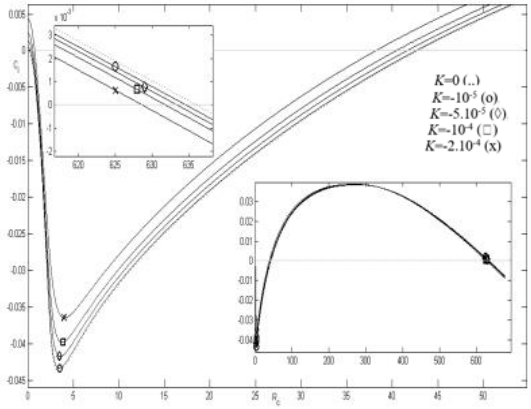

Fig. 3. Effect of R on the imaginary part of the largest eigenvalue of the fundamental mode (Re_c =6000; α_c=1), for different values of K.

Table 3: Combined effect of K and Rc on the critical stability threshold (Re_c = 5772.22; α_c = 1.02056)

R_c \ K	0	-10^{-5}	-5.10^{-5}	-10^{-4}	-2.10^{-4}	
0	5772.221	5638.37	5167.85	4698.68	4014.52	R_{ec}
	1.02056	1.0267	1.0501	1.0770	1.1250	α_c
0.2	5966.799	5824.32	5331.28	4839.89	4126.96	R_{ec}
	1.01320	1.0194	1.0428	1.0697	1.1174	α_c
0.4	6607.263	6438.22	5854.85	5282.52	4465.76	Rec
	0.99130	0.9976	1.0214	1.0485	1.0961	α_c
0.6	7902.204	7671.76	6890.68	6144.42	5110.64	R_{ec}
	0.95510	0.9617	0.9864	1.0141	1.0623	α_c

Our results are consistent with recent literature on viscoelastic and second-order fluid flows in channels. For instance, Shankar & Shivakumara [13] studied the linear stability of plane channel flow of a Navier–Stokes–Voigt fluid with vertical through flow and identified complex neutral stability curves and coupled effects of throughflow and viscoelasticity on the onset of instability [6]. Their findings highlight that the interaction of through flow and viscoelasticity can lead to non-trivial stability characteristics, which complements our observation that transverse flow (Rc) and fluid elasticity (K) interact to delay or promote instability depending on the parameter range. Similarly, Lamine et *al.* [11] demonstrated the influence of fluid elasticity on channel flow stability, further confirming the relevance of elastic effects in stabilizing or destabilizing flows.

4 Conclusion

This study analyzed the linear stability of a second-order fluid flowing between two parallel, porous plates with a uniform transverse flow. For a Newtonian fluid without transverse flow, the critical Reynolds number was found to be 5772.22 with a critical wave number of 1.021. Introducing transverse flow increased the critical Reynolds number, reaching 5966.8, 6607.3, and 7902.2 for Rc = 0.2, 0.4, and 0.6, showing that cross-flow stabilizes the system. When fluid elasticity was included ($K = -10^{-4}$), the growth rate of the most unstable mode decreased by about 15%, delaying the onset of instability. At high transverse flow rates, elasticity and cross-flow combined to further stabilize the flow, demonstrating that even slight viscoelasticity can significantly influence flow behavior.

Although this study is primarily numerical, the results provide useful quantitative insights for practical applications such as polymer transport, filtration, and heat transfer. In particular, the stabilizing effects of transverse flow and fluid elasticity on the critical stability thresholds could inform the design and optimization of systems involving slightly viscoelastic fluids. Future work could focus on translating these numerical findings into concrete engineering guidelines.

Overall, these results quantify how transverse injection and fluid elasticity interact, offering valuable perspectives for fluid handling, industrial processes, and flows in porous media.

References

[1] M. Assoul, A. El jaouahiry, J. Bouchgl, M. Echchadli, S. Aniss, Effect of Horizontal Quasi-Periodic Oscillation on the Interfacial Instability of Two Superimposed Viscous Fluid Layers in a Vertical Hele-Shaw Cell, Fluids, 8, 6 (2023). https://doi.org/10.3390/fluids8060164.

[2] J. Bouchgl, S. Aniss, S., Effect of periodic oscillation on the interfacial instability of two superposed fluid layers in a fully saturated porous media, Int. J. Appl. Mech.**,** **13**, 2150088 (2021). https://doi.org/10.1142/S1758825121500885

[3] MBM. Khan, M. Sani, S. Ghosh, H. Behera, Poiseuille-Rayleigh-Benard instability of a channel flow with uniform cross-flow and thermal slip, Phys. Fluids, **33**, 053612 (2021). https://doi.org/10.1063/5.0050006.

[4] B.M. Shankar, I.S. Shivakumara, Changes in the hydrodynamic stability of plane porous-Couette flow due to vertical through flow, Phys. Fluids, **33**, 074103 (2021). https://doi.org/10.1063/5.0054179.

[5] A.J. Badday , A.J. Harfash, Instability in Poiseuille flow in a porous medium with slip boundary conditions and uniform vertical throughflow effects, J. Eng. Math., **135**, 6, (2022). https://doi.org/10.1007/s10665-022-10231-w

[6] B.M. Shankar, I.S. Shivakumara, Stability of plane Poiseuille and Couette flows of Navier-Stokes-Voigt fluid, Acta. Mech., **234**, 4589 (2023). https://doi.org/10.21203/rs.3.rs-2497965/v1

[7] D.L. Shivaraj Kumar , M.S. Basavaraj , Dual analysis of stability in plane Poiseuille channel flow with uniform vertical cross flow, Phys. Fluids, **36**, 034106 (2024). https://doi.org/10.1063/5.0191925

[8] D.L. Shivaraj Kumar , M.S. Basavaraj, Stability patterns in plane porous Poiseuille flow with uniform vertical cross-flow: a dual approach, Int. J. Non-Linear Mech., **165**, 104797 (2024).

https://doi.org/10.1016/j.ijnonlinmec.2024.104797

[9] S.S. Hajool, A.J. Harfash, Instability of Poiseuille flow in a bidisperse porous medium subject to a uniform vertical through flow effect, ASME J. Fluids Eng., **146**, 051301 (2024). https://doi.org/10.1115/1.4064102.

[10] A.S. Varghese , S. Panda, Flow instabilities of second-grade fluid over a stretching sheet, Eur. J. Mech. B/Fluids, **102**, 135 (2023). https://doi.org/10.1016/j.euromechflu.2023.07.009

[11] M. Lamine, S. Aniss, A. Hifdi, Linear Stability Analysis of Viscoelastic Fluids in a Plane Channel Flow, Advances in Mechanics. CMM 2022. Lecture Notes in Mechanical Engineering. Springer, Cham, (2024). https://doi.org/10.1007/978-3-031-46973-2_12

[12] M. Lamine, A. Hifdi, Stability analysis of a viscoelastic liquid in a channel flow with uniform wall suction/blowing, J. Eng. Math., **152**,1 (2025). https://doi.org/10.1007/s10665-025-10463-6.

[13] B.M.Shankar, Shivakumara I.S, On the hydrodynamic stability of channel flow of a Navier–Stokes–Voigt fluid with vertical throughflow, Int. J. of Non-Linear Mech., **178**, (2025). https://doi.org/10.1016/j.ijnonlinmec.2025.105224.

Ecological strategies for reusing aquaculture water in agriculture

Khadija Ouaissa[1,2,*], *Jamila* Bouchgl[3], *M'Hamed* Hmamou[1], *Abdel Ali* Fadlali[1], and *Mustapha* Hasnaoui [2]

[1] Aquaculture laboratory; Higher institute of maritime Fisheries. Agadir. Morocco.
[2] Environmental, Ecological and Agro-Industrial Engineering Laboratory. Department of Biology, Faculty of Sciences and Techniques. University Sultan Moulay Slimane. Beni-Mellal, Morocco.
[3] Laboratory of energy Engineering, Materials and Systems, ENSA, Ibn Zohr University, Agadir, Morocco.
[*]Corresponding author : khadijaouaissa89@gmail.com

Abstract:

This study evaluates the feasibility of using fish farm effluent as a substitute for chemical fertilizers in maize cultivation. Four treatments were applied: T0 – freshwater (control), T1 – fish farm effluent, T2 – water + mineral fertilizer, T3 – fish effluent + nitrogen supplementation. Key growth parameters (width, vigor, number of leaves) were measured at early and late developmental stages. ANOVA results indicated no statistically significant differences among treatments for all measured parameters ($p > 0.05$). Maize irrigated with fish farm effluent (T1) showed slightly higher early growth (width = 47.2 mm, vigor = 8.77, leaves = 5) compared to T0 (width = 52.8 mm, vigor = 10.33, leaves = 6), while T2 and T3 treatments had similar trends. Effluent treatments provide essential nutrients (N, P, K), supporting initial growth and promoting circular agriculture. This approach may reduce synthetic fertilizer use, lower production costs, and decrease environmental pollution. The study highlights fish farm effluent as a sustainable irrigation source for maize.

1. Introduction

Increased use of chemical fertilizers in agriculture and more intensive agricultural operations have resulted in a number of negative impacts on the environment, including pollution of soils and depletion of T_0 resources. There is also an increase in eutrophication of aquatic ecosystems as a result of exposure to mineral fertilizer [1 , 2]. The application of mineral fertilizers does improve crop productivity; however, the overuse of these products has resulted in the depletion of many natural resources and increased costs to the agricultural industry, especially in the case of arid and semi-arid areas with limited access to fresh water [2].

As a result, rising water scarcity and the increasing global interest in sustainable agriculture has resulted in an increase in interest in integrated farming systems that reuse aquaculture by-products to reduce waste and promote sustainability [3]. Aquaculture waste (also referred to as aquaponics) can be defined as the discharge of water from fish farms and the waste produced by fish farms in the form of sewage. Aquaculture waste has been found to be an optimal source for supplying essential nutrients like nitrogen (N), phosphorus (P), and potassium (K) from fish feces and uneaten feed remains [4].

Research indicates that by using the effluents produced through aquaculture treatments as a method of irrigation, it is possible to create enhanced yield, increase water-use efficiencies, and lessen the reliance on synthetic fertilizers. An example of this type of practice is irrigation of maize with tilapia effluent, which have both provided increased production over traditional forms of irrigation [5]. Furthermore, these systems help create circular economy type systems since the water that is utilized for fish farming can then be reused to irrigate crops, which minimizes wastage, pollution, and degradation of the natural environment [6,7] . The goals of this research project are to assess whether or not tilapia pond water used as an irrigation source for maize will provide sustainable yields; determine the effects of tilapia pond water based irrigation on agro-economic factors; and provide viable alternatives to synthetic fertilizer uses, while promoting sustainable management of nutrient and water resources.

2. Materials and Methods

2.1 Experimental Site and Soil

The experiment occurred between April and June 2025. Maize was grown in soil characterized as sandy loam, pH 7.2, organic matter 2.1%, initial N = 0.15%, P = 15 mg/kg, K = 110 mg/kg, each treatment had 3 replicates.

Table 1. Initial physicochemical characteristics of the experimental soil.

Soil parameters	Value
Soil texture	Sandy Loam
pH	7.2
Organic matter	2.1 %
Initial nitrogen (N)	0.15mg/kg
Initial phosphorus (P)	15mg/kg
Initial potassium (K)	110mg/kg
Replicates per treatment	3

2.2 Experimental Site

The experiment occurred between April and June of 2025. Fish were reared in 400-L tanks , where their average weight was approximately 100 g. Throughout the experiment, the fish were fed a nutrient-dense diet formulated to provide essential nutrients (protein, lipid, and mineral) and the fish were fed twice daily.“Fig. 1” shows The tilapia feed includes a high protein level, high energy level, a moderate fat level, and moderate-fiber level and adequate minerals.

Figure 1: Feed fish of tilapia

"Table 2". The inclusion of these high-quality ingredients provides a feed type that supports the growth of tilapia and the production of nutrient-rich effluent that can be used as irrigation water in integrated aquaculture–agriculture farming systems.

Table 2: Biochemical Composition of Tilapia Feed

Biochemical Composition	**%**
Crude Protein	38
Crude fat	10
Crude Fibre	9
Ash	10
Phosphore	1
Calcium	1
Supplements (Vitamins , Minerals)	31
Energy	363 kcal

2.3 Monitored Parameters

To investigate the impact of a variety of irrigation and fertilization applications on maize production, the research article evaluated a number of significant factors: Growth Rate of the Plant; Leaf coloration; The presence of signs that indicate the existence of nutritional deficiencies in the crop; and The general condition of all crops during their growth cycle. These parameters were used to evaluate plant health and development. to evaluate the health status and level of development of plants, as well as to determine whether irrigation and fertilization methods used are effective. The article includes information from four separate experiments that used daily irrigation and included four different irrigation and fertilization applications to test the effects on maize.

2.4 Experimental treatments:

First Test of this Study: the corn crop was watered with freshwater all the way through. Second Test of this Study: the corn crop was watered with water obtained from a soilless dry-farming technique. Third Test of this Study: the corn crop was watered with fish-farming-derived water. Fourth Test of this Study: the corn crop was watered with fertilizer.

3. Results and discussion

Table 3 : Results of the measured parameters

Date	PLANT	Symbol	Width (mm)	Vigor (mm)	Irrigation (ml)	Color degrees	Number of leaves	Temperatur (C)
21-04-2025	Freshwater (control)	T0	27	8.8	100	4.5	4	24
	Fish farm effluent	T1	32.5	8	100	4.5	5	24
	Water + mineral fertilizer	T2	32.5	8	100	4.5	5	24
	Fish effluent + nitrogen supplementation	T3	39	8.7	_	4.5	4	24
23-04-2025	Freshwater (control)	T0	29.5	8.87	200	4.5	4	26
	Fish farm effluent	T1	34	9	200	4.5	5	26
	Water + mineral fertilizer	T2	34.5	9	200	4.5	5	26
	Fish effluent + nitrogen supplementation	T3	39	8.7	_	4.5	4	26
24-04-2025	Freshwater (control)	T0	31	8.87	250	4	4	25
	Fish farm effluent	T1	34.9	9	250	4	5	25
	Water + mineral fertilizer	T2	37	9	250	4	5	25
	Fish effluent + nitrogen supplementation	T3	39	8.7	_	4	4	25
25-04-2025	Freshwater (control)	T0	32	8.87	300	4.5	4	27
	Fish farm effluent	T1	36	9	300	4.5	5	27
	Water + mineral fertilizer	T2	37	9	300	4.5	5	27
	Fish effluent + nitrogen supplementation	T3	39	8.7	_	4,5	4	27
27-04-2025	Freshwater (control)	T0	35	9.11	300	4.5	5	23
	Fish farm effluent	T1	39	7.61	300	4	4	23
	Water + mineral fertilizer	T2	37.5	7.49	300	4	4	23
	Fish effluent + nitrogen supplementation	T3	42	8.71	_	3.5	4	23
28-04-2025	Freshwater (control)	T0	38.5	9.12	300	4,5	5	24

	Fish farm effluent	**T1**	41.4	7.88	300	4	4	24
	Water + mineral fertilizer	**T2**	39	7.5	300	4	4	24
	Fish effluent + nitrogen supplementation	**T3**	43	8.88	_	3.5	4	24
29-04-2025	**Freshwater (control)**	**T0**	40	9.60	100	4.5	5	24
	Fish farm effluent	**T1**	43	8.23	150	3,5	4	24
	Water + mineral fertilizer	**T2**	38	7.15	150	4	4	24
	Fish effluent + nitrogen supplementation	**T3**	41		_	3	4	24
30-04-2025	**Freshwater (control)**	**T0**	42,5	9.37	100	4.5	5	22
	Fish farm effluent	**T1**	45.3	8.25		3.5	4	22
	Water + mineral fertilizer	**T2**	39.5	7.53		4	4	22
	Fish effluent + nitrogen supplementation	**T3**	44.8	8.95	_	3	4	22
31-04-2025	**Freshwater (control)**	**T0**	45.4	9.74	100	4.5	5	21
	Fish farm effluent	**T1**	47.2	8.14	100	4	4	21
	Water + mineral fertilizer	**T2**	46.5	9.14	_	4	4	21
	Fish effluent + nitrogen supplementation	**T3**	45	_	_	3.5	4	21
01-05-2025	**Freshwater (control)**	**T0**	48	9.8	_	4.5	5	22
	Fish farm effluent	**T1**	49	8.19	100	4	5	22
	Water + mineral fertilizer	**T2**	47.5	9.21	100	4	4	22
	Fish effluent + nitrogen supplementation	**T3**	45.6	8.96	_	3.5	5	22
03-05-2025	**Freshwater (control)**	**T0**	52.8	10.33	100	4.5	6	22
	Fish farm effluent	**T1**	46.2	8.77	100	4	5	22
	Water + mineral fertilizer	**T2**	48.2	9.39	100	3.5	4	22
	Fish effluent + nitrogen supplementation	**T3**	45.9	9.11	_	3	5	22

Table 4 : Analysis of Variance (ANOVA) Results for the Effects of Treatment on Plant Width, Vigor, and Number of Leaves.

Parameters	Source	df	F-value	P-Value
Width	Treatment	3	=1,1	⟩0,05
Vigor	Treatment	3	n.s	⟩0,05
Number of leaves	Treatment	3	n.s	⟩0,05

The results of the analysis of variance (ANOVA) for the three measured factors width, vigor, and number of leaves affected by the different treatments are summarized in the table. The statistical analysis was performed to determine whether the applied treatments had significant effects on these plant growth parameters.

Width: The F statistic for width was 1.1, with a p-value greater than 0.05. This indicates that there were no statistically significant differences in plant width among the treatments. In other words, the application of different treatments did not lead to measurable changes in plant width at the alpha level of 0.05.

Vigor: For plant vigor, the F statistic was reported as not significant (n.s.) with a p-value exceeding 0.05. This suggests that the treatments did not produce significant variations in the overall vigor or growth robustness of the plants. The lack of statistical significance implies that any observed differences in vigor could be attributed to natural variability rather than the experimental treatments.

Number of leaves: Similarly, the analysis for the number of leaves yielded an F statistic marked as not significant (n.s.) with a p-value greater than 0.05. This result shows that the treatments did not significantly affect the leaf count of the plants compared to the control. The absence of a significant effect indicates that all treatment groups maintained similar foliar development.

Figure 2 : Visual appearance of maize crops under different irrigation treatments

Table 3 summarizes the effects of irrigation treatments on maize growth at early and late developmental stages. early growth (April 21, 2025) and later growth

(May 3, 2025). During these two periods, we measured plant width, vigor, leaf color, number of leaves, irrigation application, and ambient temperature. Plants irrigated with freshwater showed the greatest increase in width; however, this difference was not statistically significant. giving them the advantage of faster growth compared to the other treatments. On the other hand, plants watered with T_1 and dry fertilizer started with a larger diameter, but their growth slowed down later on. This suggests that while their growth rate initially increased, it eventually plateaued.

T_0 irrigation produced the largest percentage increase in plant vigor, likely due to compensatory growth following the slow initial growth of the plants [8] . In contrast, the nutrient-enriched treatments maintained relatively constant high levels of vigor throughout the entire experiment, indicating continuous vigor and the presence of a good physiological state [8] . A slight decrease in leaf color intensity was observed in the nutrient-enriched treatments during the later stages of the experiment. This trend could indicate the onset of a mild nutrient deficiency, or it could reflect physiological adaptations due to rapid growth or increased nutrient uptake by the plants.

The largest percentage increase in leaf count occurred in plants irrigated with T0, further suggesting compensatory growth [8] .There was no significant difference in the number of leaves produced between the nutrient-enriched treatments and the number of leaves produced by the plants. For the nutrient-enriched treatments, there was a relatively more moderate or stable increase in the number of leaves produced compared to initial leaf production, followed by a decrease in the rate of leaf emergence during the later stages of the experiment .

The findings of this research indicate that the use of nutrient-enriched irrigation water from an aquaculture pond for tilapia farming and growth, according to the study by [8] had a more positive effect on the initial growth of maize plants than the use of T_0 alone for irrigation. Specifically, the increase in maize plant early growth response can be attributed to the higher concentrations of macronutriments such as nitrogen, phosphorus, and potassium present in aquaculture waste [9] . It has been shown that irrigation with aquaculture effluent leads to an increase in the amounts of N, P, and K in the soil and an accelerated growth rate of crops compared to irrigating crops with T_0 [8]. Enriched treatments, like those involving nutrient-rich aquaculture effluents, have been highlighted by researchers as a valuable source of nutrients. According to studies, these effluents, derived from aquaculture systems, offer a promising alternative for boosting plant health and growth [9] . It was also pointed out that aquaculture effluents serve as a valuable alternative source of essential nutrients for a range of agricultural uses, including livestock, garden vegetables, and other crops. This helps reduce reliance on traditional mineral fertilizers while boosting the overall vitality of the crops. [10, 11] further supported this, demonstrating that the rapid growth rates observed during the early stages of crop treatment with nutrient-enriched aquaculture effluents will not be sustained in the long term unless nutrient inputs are properly managed. This idea is confirmed by [12, 13], who found that the rapid depletion of nutrients in aquaculture effluents requires additional supplementation to ensure continued growth. Other studies have shown that aquaculture effluents can, at least temporarily, increase soil fertility; however, this benefit diminishes if nutrient sources are not replenished and maintained at appropriate levels over time [9] . Additionally, [14- 15] emphasized that water containing high nutrient levels used for irrigation must maintain a proper balance of macronutriments to avoid nutrient deficiencies or imbalances, especially during the later stages of plant development.

4. Conclusion

This study suggests that fish pond water may serve as an alternative to chemical fertilizers in maize irrigation. Early growth was slightly enhanced by effluent treatments due to N-P-K supply, but no significant differences were found among treatments. Using fish pond effluents can reduce reliance on synthetic fertilizers, decrease production costs, and support circular agriculture. Proper nutrient management is essential to maintain crop development and avoid deficiencies.

References

1. M. Jenzri, C. Gharred, Z. Bouraoui, ,H. Guerbej, J. Jebali, & T. Gharred, . Evisceration of Holothuria poli by mechanical, chemical and hypoxia stress methods and its bioremediation potentials for the pisciculture wastewater. Aquaculture Research, 53(9), 3309–3317. (2022) DOI: https://doi.org/10.1111/are.15838
2. Food and Agriculture Organization of the United Nations (FAO). The State of World Fisheries and Aquaculture 2024: Blue Transformation in Action. Rome : FAO. ISBN 978-92-5-138763-4. https://openknowledge.fao.org/handle/20.500.14283/cd0683
3. R.C. Puspa & Janak Singh Rawal. Integrating Aquaculture and Hydroponics: A Review of Aquaponics Systems and Their Sustainability. Engineering Heritage Journal, 5(2): 53–61. (2024). doi : 10.26480/gwk.02.2024.53.61
4. I. Kolozsvári. Optimizing crop water use with saline aquaculture effluent: biomass yield and nutrient uptake in forage sorghum under effluent irrigation. Agronomy, 15(10), 2396. (2025). https://doi.org/10.3390/agronomy15102396
5. N. Ahmed, J. D.Ward, & C. P. Saint. Can integrated aquaculture- agriculture (IAA) produce “more crop per drop”? Food Security, 6(6), 767–779.(2014). DOI : https://doi.org/10.1007/s12571-014-0394-9.
6. D. N. Farrant, , K. L. Frank & , A. E. Larsen. Reuse and recycle: Integrating aquaculture and agricultural systems to increase production and reduce nutrient pollution. Science of the Total Environment, 785, 146859. (2021). https://doi.org/10.1016/j.scitotenv.2021.146859
7. K. Ouaissa, M. Hmamou , Y Ennaciri , M.Hasnaoui. Effect of Dactylogyrus Parasite on External Organs of the Nile Tilapia (Oreochromis niloticus).Egyptian Journal of Aquatic Biology & Fisheries. Article 49, Volume 28, Issue 4, July and August 2024, Pages 799-806 . DOI: 10.21608/ejabf.2024.369527
8. J. Smith, A. Brown, & M.Lee. Effects of irrigation and nutrient enrichment on plant vigor and leaf dynamics in controlled growth experiments. Journal of Plant Science and Nutrition, 15(4), 325–337. (2020) . https://doi.org/10.1016/j.scitotenv.2021.146859
9. A. A. Diatta, , A. G. B Manga, C. Bassène, C. Mbow, M. Battaglia , M. Sambou , E. Babur, & Ö. S. Uslu . Sustainable production of tomato using fish effluents improves plant growth and yield parameters under greenhouse conditions. Agronomy, 13(11), 2696. (2023).https://doi.org/10.3390/agronomy13112696
10. T. Tang, H.-J. Kim Effects of Hydraulic Loading Rate on Spatial and Temporal Water Quality Characteristics and Crop Growth and Yield in

Aquaponic Systems. Horticulturae, 6(1), 9. (2020). DOI : https://doi.org/10.3390/horticulturae6010009

11. K. Ouaissa , A. kritihi, A. Maychal , M. Hasnaoui. Evolution of Fish Farm Feeding Strategies in Aquaculture. Egyptian Journal of Aquatic Biology & Fisheries. Vol. 28(5): 321 – 329 (2024). https://doi.org10.21608/ejabf.2024.378876
12. H. Guo, L. Liao, Z. Zheng, J. Xu Q. Wei, P. Chen, & K. Wang. Evaluating the effects of aquaculture wastewater irrigation with fertilizer reduction on greenhouse tomato production, economic benefits and soil nitrogen characteristics. Phyton – International Journal of Experimental Botany, 92(12), 1–10.(2023). https://doi.org/10.32604/phyton.2023.044051
13. B. S.Cerozi de Oliveira, R. L, J. J.Wang, & L. H. M da Silva. Fish effluent as a source of water and nutrients for sustainable urban agriculture. Agriculture, 12(12), 1975. (2022) https://doi.org/10.3390/agriculture12121975
14. M. Al- Wabel, M. I., Almutari, M. M., Ahmad, M., Al- Swadi, H. A., Ahmad, J., & Al- Farraj, A. S. F. . Impacts of aquaculture wastewater irrigation on soil health, nutrient availability, and date palm fruit quality. Scientific Reports, 14, 18634. (2024) https://doi.org/10.1038/s41598- 024- 68774- 0.
15. A. Mielcarek, A. Kłobukowska, K.Rodziewicz, J. Janczukowicz, W. & Bryszewski, K. Ł. Water nutrient management in soilless plant cultivation versus sustainability. Sustainability, 16(1), 152. (2024). https://doi.org/10.3390/su16010152

Artificial Intelligence and Big Data for Dynamic Pricing in Renewable Energy Markets: A Review of Forecasting and Optimization Approaches

Ikram Lefhal Lalaoui [1*], *Essaid* El Haji [1], and *Mohamed* Kounaidi[1]

[1]Intelligent Automation and BioMed Genomics Laboratory, FST of Tangier, Abdelmalek Essaadi University, Tetouan, Morocco

Abstract. The use of artificial intelligence (AI) and big data technologies has increased the usage of dynamic pricing mechanisms in renewable energy markets. The increasing amount of renewable energy being installed into the electric grid i.e. solar and wind is causing variable amounts of electricity to be produced, which is causing price volatility in the wholesale electricity market. AI-based forecasting and optimization techniques can effectively utilize large energy datasets to improve pricing methodologies.

This paper provides an overview of current research on the applications of artificial intelligence and big data for dynamic pricing in renewable energy markets. The review will discuss machine learning (ML), deep learning (DL), and reinforcement learning (RL) techniques, as well as big data platforms that are being used to process information obtained from smart meters, weather stations, and wholesale electricity market prices. Research demonstrates that AI models outperform traditional methods for forecasting; specifically, hybrid deep learning frameworks have provided very good results with mean absolute errors (MAEs) of as low as 0.138, root mean square error (RMSEs) of as low as 0.166 for various electricity markets. A comparison of CNN-BiLSTM models using hyperparameter optimization to traditional approaches resulted in an average reduction in RMSE of 16.7%, and an average reduction in MAE of 23.46%. In addition to achieving high levels of accuracy, deep learning-based forecasting tools also provide significant computational advantages. Specifically, deep learning-based forecasting tools run at least five times faster than traditional benchmarks for multiple markets. These results clearly indicate that AI-based forecasting models produce superior results relative to traditional forecasting methods as measured by metrics such as mean absolute percentage error (MAPE) and root mean square error (RMSE). Finally, this review identifies several critical challenges facing the use of AI-driven dynamic pricing in smart grid systems. These challenges include, but are not limited to, data availability, model interpretability, and regulatory constraints.

1 Introduction

The widespread transition to renewable-based electricity systems will radically alter the structure and function of today's electricity markets. The inherently volatile and weather-sensitive characteristics of renewable sources of energy (such as solar and wind) are producing unprecedented levels of volatility and uncertainty in the supply and price of electricity [1–5]. Previous studies have highlighted that accurate electricity price

* Corresponding author: ikram.lefhallalaoui@etu.uae.ac.ma

forecasting is essential for efficient market operation and demand response management in renewable-dominated power systems [2–5]. As a result of this increased volatility, existing static pricing methodologies are no longer sufficient; there is an immediate need for advanced, dynamic pricing methodologies that can provide incentives for efficiency in consumption while maintaining the stability of the grid [6–11].

At the same time, the increasing digitization of the electric system through the installation of smart meters, sensors and digital marketplaces has created enormous amounts of "Big Data." When combined with the exponential growth of artificial intelligence (AI) capabilities and machine learning (ML), deep learning (DL), and reinforcement learning (RL) techniques, the potential for developing advanced methods of analyzing this data for price forecasting and real-time decision making is tremendous [1, 8, 9]. As a result, researchers are actively investigating the development of the next-generation of intelligent, data-driven pricing systems that utilize the converging technologies of big data analytics and AI to advance dynamic pricing models for renewable dominated electricity markets [10, 12].

There is currently a large body of literature that explores the application of various forms of AI to pricing and forecasting tasks [2–5, 7], however, prior reviews of this literature have generally been limited to a narrow focus on forecasting methodologies [1, 2] or to more general uses of AI in the energy sector [9]. A critical gap therefore remains in terms of a comprehensive review of the literature that addresses how the combined use of AI and big data is advancing dynamic pricing models in the unique context of renewable based electricity markets. To synthesize the current state of the art and to create a common framework for evaluating the architectures and performances of proposed systems as well as identifying consistent issues and problems (e.g., scalability, interpretability, regulatory requirements) that remain to be addressed by future research efforts is essential.

To address the existing knowledge gap identified above, this study will carry out a review of the literature related to applications of AI and Big Data to support the implementation of dynamic pricing in renewable energy markets. The ultimate objectives of this review are to: (1) categorize and compare the most prominent AI-based systems and architectures for use with the relevant data; (2) synthesize the results reported from each study in terms of how well they performed and what their design was; (3) assess and criticize the major technical and non-technical hurdles to using these techniques in practice; and (4) to identify and outline needed areas of research to assist in developing and implementing new technologies to support the sustainable development and operation of intelligent energy markets. In the remainder of this paper, we will detail the subsequent steps based on our defined framework. In Section 2, we will provide a general overview of the background information needed. In Section 3, we will explain the approach to conducting our literature review. In Section 4, we will report on the summary of our analysis of the methodologies and findings. In Section 5, we will outline the technical and non-technical obstacles and limitations to employing these methods in practice. In Section 6, we will outline potential areas of future research. In Section 7, we will provide a comprehensive summary of our efforts.

2 Background and Key Concepts

2.1 Renewable Energy Markets

Modern electric power markets have a growing proportion of variable renewable generation as an outcome of an increase in the use of intermittent energy producers such as wind and solar power. The amount of electricity generated from these renewable resources is very

dependent upon the weather, therefore introducing substantial amounts of uncertainty (unpredictability) and variability (intermittence) into the electric power supply [1, 5] This basic nature of renewable resources has a direct impact on how markets operate, prices form and ultimately grid reliability. Markets with a large share of renewable energy will experience greater price fluctuations and more often than not negative price events and higher demands for flexibility on both the supply and demand side of the electric system [5]. Although the emerging designs of markets (i.e. day ahead, intra-day and balancing markets) offer potential solutions, most of the current pricing mechanisms do not account for real time operating conditions of the electric system nor do they effectively encourage consumers and producers to optimize their respective consumption and production patterns [11]. Therefore, there is a critical need for advanced, data-driven pricing models to facilitate managing the natural variability and uncertainty associated with renewable energy markets [6, 11].

2.2 Dynamic Pricing Mechanisms

The tariffs of Dynamic Pricing are influenced by real-time variations of the price of electricity, due to the dynamics of supply, demand and restrictions on the grid. These tariffs can be implemented using different models such as TOU (Time Of Use), RTP (Real-Time Pricing) and CPP (Critical Peak Pricing). Their main purpose is to influence consumer's behavior (to move their use from peak hours to off-peak hours, or to reduce their global consumption in case of peak hours or when there is lack of supply/demand) [6]. The large-scale installation of Smart Meters and advanced telecommunications infrastructures have allowed the technical implementation of Dynamic Pricing tariffs; however, developing the best dynamic pricing strategy is still a complex problem because it includes forecasting and reacting to many nonlinear and probabilistic variables present in the energy markets [3, 4]. For this reason, Dynamic pricing mechanisms require accurate forecasting models and real-time decision-making capabilities, if we have the ability to make decisions based on real-time information and if we can optimize continuously the price of electricity, all of which represent great opportunities for the application of AI [6, 12].

2.3 *Artificial Intelligence and Big Data in Energy Systems*

The modern electricity grid produces an ever-growing amount of data from many different types of data sources, for example, weather monitoring stations, energy market platforms, wind farms and other forms of renewable energy generators and smart energy meters. This presents a considerable problem in terms of managing it and realizing value from it in that it contains so much information, and the rate at which it can be generated and processed is very high, and it takes on a multitude of formats [10, 13]. Cloud computing, edge computing, distributed databases are just a few examples of technology which enables the building of scalable systems to manage the large volumes of data. At the same time, artificial intelligence (AI) which includes machine learning (ML), deep learning (DL), and reinforcement learning (RL) have shown impressive capabilities to model complex system behavior, to identify non-linear relationships between variables and to learn how to behave under changing conditions [8, 9]. With regards to dynamic pricing, AI is being used to build predictive models to forecast prices [1–5, 7] to determine optimal pricing strategies [6, 11] and to provide the capability for real-time, automatic decision making [13]. The integration of AI with big data analytics provides the potential for creating smart, adaptive and cost-effective pricing systems for renewable energy markets of the future [10, 12].

3 Review Methodology

The review process provided an opportunity for a consistent, reproducible, and transparent examination of all available literature. Literature searches were completed in various academic databases, including ScienceDirect, SpringerLink and Scopus. All of these databases provide access to many of the top journals in the field of interest; thus, they were searched to ensure that high impact journals were included. The focus of the search was on the latest and most influential studies about the topics of artificial intelligence, big data analytics, dynamic pricing, and renewable energy markets, with a primary emphasis on studies which have been published since 2020. Therefore, the purpose of the search was to identify the most recent methodologies and technologies currently being employed in the area of interest. A combination of keywords ("dynamic pricing," "electricity price forecasting," "renewable energy markets," "machine learning," "deep learning," and "big data analytics") and Boolean operators were used to isolate relevant studies. Additionally, only peer-reviewed articles from academic journals were included in this study so as to ensure their scientific validity and relevance.
In order to organize the studies selected for inclusion based upon the AI and big data techniques they employed, the data sources utilized by those studies, the architectures of systems described in the studies, the goals of applications described in the studies, and the performance evaluation metrics used in the studies, a classification framework was developed. In addition to identifying the predominant trends and concerns within the field, and areas where additional research may be warranted, an organized and systematic review of each study enabled the identification of the most significant findings from the structured review.

4 AI and Big Data Techniques for Dynamic Pricing

The systematic evaluation of research on renewable energy markets and how they relate to dynamic pricing challenges has resulted in a clear categorization of types of solutions being used to address the challenges in renewable energy markets. There are three main categories of AI based methodologies that support the architecture necessary for large-scale big data systems; Machine Learning (ML), Deep Learning (DL) and Reinforcement Learning (RL). Fig. 1 illustrates the overall architecture of an AI-based dynamic pricing system, and Table 1 presents an integrated view of the types of methodologies, their uses and the references included in this study.

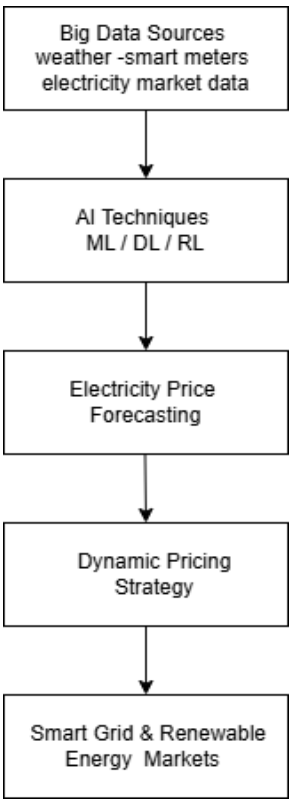

Fig. 1. AI-Based Dynamic Pricing Framework

Table 1. AI and Big Data Techniques Applied to Dynamic Pricing in Renewable Energy Markets.

Technique	Main Purpose	Example Models	Example References
Machine Learning	Electricity price forecasting and pattern recognition	SVM, Random Forest, Gradient Boosting	[2], [8]
Deep Learning	Modeling temporal and nonlinear price patterns	LSTM, CNN, CNN-BiLSTM	[3], [4], [5]
Reinforcement Learning	Adaptive pricing and demand response optimization	Q-learning, DQN	[6], [13]
Big Data Platforms	Large-scale data processing and analytics	Apache Spark, Cloud computing	[10], [12]
Hybrid AI Systems	Integrated forecasting and optimization frameworks	DL + RL hybrid models	[3], [11]

The primary application of machine learning algorithms is for price forecasting and pattern recognition. Deep learning algorithms can be used to identify complex nonlinear

patterns within large time series data sets. There is an increasing use of reinforcement learning to optimize adaptive pricing and demand response systems.

4.1 Machine Learning for Forecasting and Pattern Recognition

Traditional and advanced machine learning (ML) techniques continue to be at the core of the process of forecasting electricity prices, which is an essential input to all pricing models. Support Vector Machines (SVM) and Random Forest algorithms, among other ensemble methods, are well regarded for their capacity to model nonlinear relationships in the marketplace that involve the output of renewable generators and trends in customer demand [2, 8], and these models can serve as a baseline for comparison to other approaches or can be used within more complex modeling processes. Broader reviews support the use of ml as a flexible and effective technology across many different types of applications within the energy systems area [9].

4.2 The Rise of Deep Learning Models

Deep learning (DL) models have shown greater performance capabilities than others especially when it comes to identifying complex patterns of temporal dependency and processing large dimensional datasets that characterize contemporary energy market data. LSTM networks as well as CNNs are being utilized for time series forecasts [1]. These forecasting models learn a complex mapping function from input features to predicted electricity prices, which can be mathematically represented as:

$$\hat{P}_t = f(X_t, \theta) \quad (1)$$

Where $\hat{P}_t$ is the predicted electricity price at time t, X_t is the vector of input features (including historical prices, weather data, demand patterns, and renewable generation forecasts), and θ represents the model parameters learned during training.

Hybrid or ensemble DL models that use a combination of different architectures are currently trending to provide increased accuracy and robustness. Studies have been successful in implementing CNN-BiLSTM models with hyperparameters optimized [4], as well as other hybrid frameworks using multiple data sources and/or additional algorithmic steps to forecast day ahead prices [3, 5, 7]. In addition to showing measurable improvement in error metrics (RMSE, MAE) etc, these models also demonstrate a higher level of performance compared to their respective traditional machine learning (ML) benchmarks.

4.3 Reinforcement Learning for Adaptive Strategy Optimization

Although ML & DL are used for forecasting, RL can be used for direct strategy optimization in the context of optimizing price and/or DR policy. By using a simulated or live marketplace environment as its learning environment, an agent learns what the optimal pricing and/or DR policy should be through continuous interaction with the environment; this makes it well-suited for use in real-time and adaptive pricing applications. Some examples of how this could be applied include: developing incentive-based demand response strategies for smart-grids [6], and developing real-time bid and price management strategies for load aggregators [13]. In both examples, RL has demonstrated significant promise for enabling dynamic, closed loop pricing/DR strategies that adapt based on changing conditions in the grid.

4.4 *The Enabling Role of Big Data Architectures*

The ability to effectively apply these described AI models will depend on the availability of scalable big data architectures to process the data coming from smart meters, weather sensors, and markets at a rate of volume, velocity, and variety. Research has shown how big data processing systems such as Apache Spark have been used in large scale load forecasting and demand response studies; they also provide examples of successful project implementations (e.g., Low Carbon London) [10]. Additionally, the emergence of platforms that integrate both big data management and AI analytics is providing the necessary support to the new generation of electric utilities and their associated technologies to create an end-to-end pipeline from collecting data to deploying models [12].

4.5 *Convergence: Hybrid and Market-Aware Systems*

The main trend is toward a complete system combining forecast, optimization, and learning parts using integrated solutions. This trend can be seen both from a technical standpoint as hybrid AI models that use DL forecasting with RL optimization [6, 13] and structural standpoint through AI based on market frameworks that introduce new mechanisms for peer-to-peer energy trading and dynamic pricing within regulatory boundaries [11]. Both are at the front of the research, and they aim to create an entire (holistic), large scale, and market aware smart pricing systems.

Table 2. Comparison of Recent AI-Based Electricity Price Forecasting Studies.

Study	Method	Dataset	Main Contribution
Lago et al. (2021)	Machine learning ensemble	European markets	Benchmark framework for forecasting
Huang et al. (2024)	Hybrid deep learning	Chinese electricity market	Improved day-ahead price prediction
Mubarak et al. (2024)	CNN-BiLSTM	Smart grid datasets	Hybrid DL forecasting
Aliyon & Ritvanen (2024)	Deep learning	European electricity markets	Analysis of price predictability
Salazar et al. (2023)	Reinforcement learning	Smart grid demand response	Adaptive pricing strategy

Table 2 presents a comparison of representative studies that apply artificial intelligence techniques to electricity price forecasting and dynamic pricing. The table highlights the diversity of datasets, modeling approaches, and research objectives addressed in recent literature.

5 Challenges and Limitations

Although both AI and Big Data have shown promise in making dynamic pricing in renewable energy more efficient, there are a number of key barriers that prevent them from being implemented in practice. The first barrier to implementing these technologies has been related to data - namely how to collect, store, process and analyze high-quality data in real time in a way that aggregates large amounts of disparate data types (e.g., market price, weather conditions, customer behaviors) to provide reliable output from models [10]. This data-related challenge is compounded by a second major challenge associated with the interpretability/explainability of the models. While advanced AI models, especially those using deep learning and/or reinforcement learning, can be highly accurate in their predictions and actions, they typically operate as "black boxes" (i.e., the inputs/outputs, internal workings and decision-making processes are unknown), thereby generating skepticism/trust issues among regulators, market participants and customers and hindering acceptance of new models/systems [1, 4, 6, 11]. In addition to technical challenges, there are also regulatory and market design barriers to implementation. Current frameworks for setting prices, participating in markets and handling data privacy are generally incompatible with the rapid development and data-intensive nature of AI-based pricing systems, a mismatch that is not typically examined in detail in technical analyses [11]. Last, the question of whether scalable, broadly applicable models exist remains an open one. Many models have been validated in case studies/simulations but lack evidence that they will perform well in other grid environments/market regimes [10, 12]. Therefore, overcoming these interconnected technical, regulatory and practical challenges is necessary for advancing from research into trusted, commercially viable intelligent pricing systems.

6 Research Gaps and Future Directions

This study has identified several key research areas where further work is needed to progress the area of using artificial intelligence to create dynamically priced renewable energy systems. One of the primary research areas needing focus is the creation of Explainable Artificial Intelligence (XAI) frameworks for energy economics, which will be able to provide accurate forecasts and optimize prices, while also allowing users to understand how the AI made its pricing decisions in an auditable manner, so as to build

trust with all stakeholders [6, 11]. At the same time, the research community needs to develop highly scalable, adaptive system architectures to process massive amounts of rapidly changing data to produce real-time price signals; this is in addition to the current use of offline analytics to develop price signals [10, 12]. In addition, a major gap currently exists in the area of integrating regulatory and market design constraints into AI models. Future research should move from developing algorithms that exist in a regulatory vacuum, to designing the pricing mechanisms that are developed through the use of AI models to be both economically efficient, and legal by default [11]. Lastly, to confirm the applicability of theoretical advances, the field of AI-DRP for RENs requires extensive testing and real world implementation of proposed models in pilot projects or experimental market environments. The testing of these models in real world environments will allow researchers to determine whether their proposed models perform well, are robust, and have the potential to positively impact society on a large scale, ultimately closing the gap between theory and practice, and enabling the establishment of sustainable and intelligent energy markets [3, 13].

7 Conclusion

This review of the literature examined recent advances in artificial intelligence and big data techniques for enabling dynamic pricing in renewable energy markets. The review clearly demonstrates that hybrid and adaptable AI-based models which utilize both deep learning techniques for forecasting as well as reinforcement learning techniques for optimizing prices, and scalable big data infrastructure to execute those optimized prices, outperform traditional price-setting methodologies. Nevertheless, there exist significant barriers to achieving transformative impact with AI-based dynamic pricing models beyond mere technological sophistication. Most notably, the complexity associated with explaining how black box AI models arrive at their conclusions, the regulatory misalignment between traditional regulatory structures and modern AI-based models, and the ability to scale solutions developed within academic or research environments into real world operational environments, are all significant impediments to wide-scale adoption of such technology. Consequently, the development of truly transformative pricing models will require a comprehensive research approach which focuses upon developing both transparent and explainable algorithms as well as regulatory aware design of those models; and finally rigorous testing and validation of those models within realistic operational environments. By addressing each of these interdependent challenges, researchers and practitioners can facilitate the widespread adoption of reliable, effective and resilient pricing systems necessary for facilitating a global transition to renewable energy-based power systems.

References

1. T. Jasiński, A Review of Recent Trends in Electricity Price Forecasting Using Deep Learning Techniques, Energies 18, 6422 (2025). https://doi.org/10.3390/en18246422
2. J. Lago, G. Marcjasz, B. De Schutter, R. Weron, Forecasting day-ahead electricity prices: A review of state-of-the-art algorithms, best practices and an open-access benchmark, Appl. Energy 293, 116983 (2021). https://doi.org/10.1016/j.apenergy.2021.116983
3. S. Huang, J. Shi, B. Wang, N. An, L. Li, X. Hou, C. Wang, X. Zhang, K. Wang, H. Li, S. Zhang, M. Zhong, A hybrid framework for day-ahead electricity spot-price

forecasting: A case study in China, Appl. Energy 373, 123863 (2024). https://doi.org/10.1016/j.apenergy.2024.123863

4. H. Mubarak, A. Abdellatif, S. Ahmad, M.Z. Islam, S.M. Muyeen, M.A. Mannan, I. Kamwa, Day-Ahead electricity price forecasting using a CNN-BiLSTM model in conjunction with autoregressive modeling and hyperparameter optimization, Int. J. Electr. Power Energy Syst. 161, 110206 (2024). https://doi.org/10.1016/j.ijepes.2024.110206
5. K. Aliyon, J. Ritvanen, Deep learning-based electricity price forecasting: Findings on price predictability and European electricity markets, Energy 308, 132877 (2024). https://doi.org/10.1016/j.energy.2024.132877
6. E.J. Salazar, M. Jurado, M.E. Samper, Reinforcement Learning-Based Pricing and Incentive Strategy for Demand Response in Smart Grids, Energies 16, 1466 (2024). https://doi.org/10.3390/en16031466
7. R. Iqbal, H. Mokhlis, A.S. Mohd Khairuddin, M.A. Muhammad, An Improved Deep Learning Model for Electricity Price Forecasting, Int. J. Interact. Multimed. Artif. Intell. 9, 1-10 (2024). https://doi.org/10.9781/ijimai.2023.06.001
8. M. Castelli, A. Groznik, A. Popovič, Forecasting electricity prices: A machine learning approach, Algorithms 13, 119 (2020). https://doi.org/10.3390/a13050119
9. M.M. Forootan, I. Larki, R. Zahedi, A. Ahmadi, Machine Learning and Deep Learning in Energy Systems: A Review, Sustainability 14, 4832 (2022). https://doi.org/10.3390/su14084832
10. H.A. El-Sayed Ali, M.H. Alham, D.K. Ibrahim, Big data resolving using Apache Spark for load forecasting and demand response in smart grid: A case study of the Low Carbon London Project, J. Big Data 11, 59 (2024). https://doi.org/10.1186/s40537-024-00909-6
11. J. Holzinger, A. Nagl, K. Bozem, C. Lecon, A. Ensinger, J. Roessler, C. Neufeld, Business Case for a Regional AI-Based Marketplace for Renewable Energies, Sustainability 17, 1739 (2025). https://doi.org/10.3390/su17041739
12. M. Santos-Dominguez, N. Hernandez Flores, I.A. Parra-Ramirez, G. Arroyo-Figueroa, AI--Big Data Analytics Platform for Energy Forecasting in Modern Power Systems, Big Data Cogn. Comput. 9, 272 (2025). https://doi.org/10.3390/bdcc9110272
13. G. Xu, S. Song, Y. Li, Y. Lu, Y. Zhao, L. Zhang, F. Wang, Z. Song, Application of deep reinforcement learning in electricity demand response market: Demand response decision-making of load aggregator, MethodsX 12, 102735 (2024). https://doi.org/10.1016/j.mex.2024.102735